UNIVERSITAT POLITÈCNICA DE VALÈNCIA

DEPARTAMENT DE COMUNICACIONS

Design of photonic sensors based on cavities and new interrogation techniques

Ph.D THESIS

Javier Hervás Peralta

Supervisor:

Salvador Sales Maicas

Universitat Politècnica de València February, 2019

"If we knew what it was we were doing,

it would not be called research, would it?"

Albert Einstein (1879-1955)

Agradecimientos

Quisiera agradecer en primer lugar a mi director de tesis por la confianza que me mostró desde el primer momento. Esta relación comenzó con aquel trabajo final de carrera, seguido por el trabajo final de máster hasta la consecución de esta tesis doctoral. Sé que no podría haber escogido un director mejor. Gracias por buscar siempre huecos para atender las infinitas dudas y problemas que surgían cada vez que intentaba algo nuevo.

Quiero dar gracias también a todos los integrantes del PRL, en especial a los *barriers.* No solo habéis sido compañeros de trabajo sino que os habéis convertido en amigos y personas que siempre llevaré en el corazón (eso que decís que no tengo). Estos casi cinco años de trabajo de investigación hubieran sido algo muy diferente sin vosotros.

Quiero agradecer también a Miguel Llera y a Walter Margulis por su acogida y dedicación durante mis estancias en la Haute Ecole Arc Ingenierie y en el instituto de investigación ACREO respectivamente.

Agradezco también el apoyo del Ministerio de Educación y Formación Profesional a través de la beca FPU FPU13/04675 sin la que este proyecto de investigación no habría podido ser llevado a cabo.

Finalmente agradecer a mi familia, y en especial a Lorena, ya que sin vuestro apoyo, cariño y confianza en mí esto no hubiera sido posible.

Gracias a todos.

Resumen

Los sensores ópticos son dispositivos fotónicos sensibles a determinadas magnitudes que se usan precisamente para medir, ya sea de forma absoluta o relativa, esas magnitudes. Medir la temperatura, la presión, la tensión, la humedad o la presencia de un determinado gas son algunas de las funcionalidades que llevan a cabo estos sensores. A lo largo de las últimas décadas multitud de sensores y técnicas de interrogación han sido desarrolladas, lo que ha tenido un increíble impacto en multitud de áreas. Uno de los ejemplos más claro es la arquitectura civil, donde los sensores fotónicos juegan un papel fundamental en la monitorización del estado de las estructuras.

A pesar de los buenos resultados conseguidos por los sensores ópticos hasta la fecha, las técnicas de interrogación desarrolladas hasta ahora muestran algunas desventajas. Tiempos de medida altos, baja resolución o una gran complejidad son algunas de ellas. En esta tesis doctoral se presenta el diseño y caracterización de diversos sensores fotónicos basados en las ya conocidas redes de difracción de Bragg así como la implementación de nuevas técnicas de interrogación de dichos sensores para intentar eliminar o reducir esas desventajas. Las técnicas de interrogación desarrolladas en este trabajo se basan en la fotónica de microondas, donde la interacción entre las señales ópticas y eléctricas se usa para detectar en este caso los cambios en una determinada magnitud.

Las técnicas desarrolladas en este trabajo buscan ser lo más versátiles y escalables posibles para así poder adaptarse a los requerimientos de diferentes escenarios. Encontramos así técnicas que permiten interrogar a miles de sensores con una gran resolución y sensibilidad así como también técnicas de interrogación de sensores puntuales con una enorme sensibilidad y simplicidad tanto en la interrogación como en el sistema usado para ello. También están presentes los resultados obtenidos mediante la colaboración con el instituto de investigación sueco ACREO para el desarrollo de un sensor de campo eléctrico basado en fibras polarizadas donde se han fabricado varias redes de difracción de Bragg.

Abstract

Optical sensors are photonic devices sensitive to different magnitudes that are used precisely to measure, in an absolute or a relative way, these magnitudes. These optical sensors are nowadays used to measure temperature, pressure, strain, humidity or the presence of a particular gas. In the past few decades a multitude of photonic sensors and different interrogation techniques have been developed, which had a great impact in dozens of different fields. One of the best examples is civil architecture, in which photonic sensors play a fundamental role in order to monitor the condition of the structures.

Despite of the good results showed by photonic sensors, the interrogation techniques used show different drawbacks. A large measurement time, low resolution or great complexity are some of them. In this doctoral thesis the design and characterization of a set of different photonic sensors based on the already known fiber Bragg gratings, along with the implementation of new interrogation techniques, are used in order to eliminate or at least reduce these problems. The interrogation techniques developed in this work are based on Microwave Photonics techniques, in which the interaction between optical and electrical signals is used to detect in this case the changes in a particular magnitude.

The techniques showed in this work have been designed in order to be as versatile and scalable as possible to have the opportunity to adapt to any requirement in different scenarios. In this work techniques that are able to interrogate hundreds or even thousands of sensors with great sensitivity and resolution can be found in addition to techniques that are developed to interrogate individual sensors with an enormous sensitivity. The work carried out in collaboration with the Swedish research institute ACREO, based on the development of an electric field sensor based on poled fibers together with FBGs is also present.

Resum

Els sensors òptics son dispositius fotònics sensibles a determinades magnituds que s'usen precisament per a mesurar, ja siga de forma absoluta o relativa, aquestes magnituds. Mesurar la temperatura, la pressió, la tensió, la humitat o la presència d'un determinat gas són algunes de les funcionalitats que realitzen aquestos sensors. Al llarg de les últimes dècades multitud de sensors i tècniques d'interrogació han sigut desenvolupades, i això ha tingut un impacte increïble a multitud d'àrees. Un dels exemples més clar es l'arquitectura civil, on aquestos sensors juguen un paper fonamental en la monitoratge de l'estat de les estructures.

Encara que els resultats aconseguits han sigut bons, les tècniques d'interrogació desenvolupades fins ara mostren alguns desavantatges. Temps de mesurament alt, baixa resolució o una gran complexitat són algun d'ells. A aquesta tesi doctoral es presenta el disseny i caracterització de diversos sensors fotònics basats en les ja conegudes xarxes de difracció de Bragg així com l'implementació de noves tècniques d'interrogació per a intentar eliminar o reduir aquestos inconvenients. Les tècniques d'interrogació desenvolupades en aquest treball es basen en la fotònica de microones, on l'interacció entre les senyals òptiques i elèctriques s'usa per a detectar en aquest cas els canvis en una determinada magnitud.

Les tècniques desenvolupades en aquest treball busquen ser el més versàtils i escalables possibles per a poder adaptar-se als requeriments dels diferents escenaris. Trobem així tècniques que permeten interrogar milers de sensors amb una gran resolució i sensitivitat però també tècniques que permeten interrogar sensors puntuals amb una increïble sensitivitat mostrant una gran simplicitat en el seu disseny. També estan presents els resultats obtinguts mitjançant la col·laboració amb l'institut d'investigació suec ACREO per al desenvolupament d'un sensor de camp eléctric basat en FBGs i en fibres polaritzades.

Index

APPENDIX 1

List of figures

List of tables

Chapter 1

Introduction to optical fibre sensors and Microwave Photonics

1.1 Context

Optical fiber sensors [1] are photonic devices in which the optical fiber is used as sensing element or as a medium to deliver and retrieve light from an external sensor. Photonic sensors have been developed in the past decades in order to change properties of light (intensity [2], phase [3], polarization [4] or wavelength [5]) with regards to an external stimulus. Currently, optical fiber sensors are used to monitor temperature [6], pressure [7], strain [8], humidity [9] and some other parameters [10-11].

Some techniques use the raw optical fiber, usually called single mode fiber (SMF), as a sensing element. In these techniques the whole fiber acts as a sensor. This kind of sensors are called distributed sensors [12]. The most used techniques to interrogate such sensors are based in some scattering phenomena that takes place in the optical fiber. The most commonly used are the Rayleigh [13], Brillouin [14] and Raman [15] scattering.

Some other techniques are based in the inscription of reflectors inside the fiber [16] in order to get some advantages, although this process restricts the ability to use the whole fiber as a sensor. In this case only the sections of the fiber in which these reflectors are fabricated are normally used as sensing points. Therefore, distributed sensing is no longer a reality and in this particular case these devices are known as multiplexed sensors [12] (if the distance between reflectors is small they can be called quasi-distributed sensors as well). The fabrication of reflectors inside the fiber can produce some benefits compared to distributed sensing such as power efficiency, higher signal to noise ratio, increased interrogation speed or lower complexity. All kind of reflectors have been fabricated in optical fibers but the most commonly used by far are known as fiber Bragg gratings (FBGs) [17]. These components reflect a particular set of wavelengths based on their physical properties, properties that are affected by the environmental conditions.

But not only the devices used to sense are important. The technique that is used to extract the sensing information, usually known as interrogation technique, is also important. Different techniques show different advantages and drawbacks and new techniques are being studied in order to overcome the disadvantages brought about by more traditional interrogation techniques. One of the most important trends is the usage of Microwave Photonics techniques [18-19] to

interrogate such sensors. The goal is to improve the resolution, accuracy, sensitivity, speed of interrogation or simplicity of the interrogation techniques.

1.2 Distributed sensors

Distributed sensing [12] allows continuous measurement along the entire length of an optical fiber cable. Traditionally, sensing systems consist of discrete sensors that measure a particular parameter at a given point. In distributed sensing, the entire fiber becomes the sensor. Normally, the interrogation of such device is carried out by an interrogator that works using a radar-style process: pulses are sent into the fiber, they are back-scattered (partially) and the system records the returned signal in relation with time. This way every point along the fiber becomes a sensor.

1.2.1 Rayleigh scattering

The term Rayleigh scattering describes light scattering coming from refractive index inhomogeneities whose size is smaller than the particular wavelength of the light travelling through the fiber [20]. This scattering phenomena is an isotropic process, which means that most of the scattered light escapes from the core to the cladding or even abandons the optical fiber. However, some of the scattered light is back reflected and transmitted through the core of the optical fiber reaching at the end the transmitter.

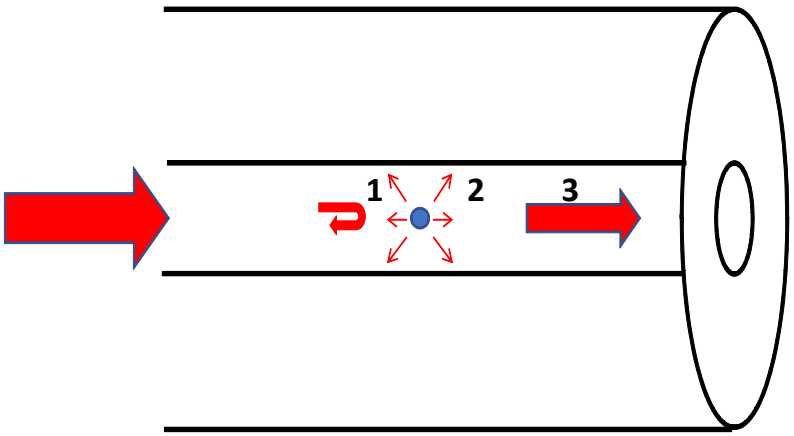

Fig. 1.1. Rayleigh scattering. 1) A small percentage of the incoming light is back reflected; 2) A small percentage of the incoming light is coupled to the cladding; 3) Most of the incoming light keeps travelling through the core

This is one of the main factors contributing to optical losses in the optical fiber. The coefficient for the losses can be expressed as [21]:

$$\alpha_S(T) = \frac{8\pi^3}{3\lambda^4}(n_1^8 p^2) kT\beta_T \quad (1.1)$$

where *n* is the refractive index, *p* is the photoelastic coefficient, *k* is Boltzmann's constant, *T* is the absolute temperature and β_T is the isothermal compressibility. These losses, as well as the amount of light that is backscattered, depend on the environmental conditions experienced by the fiber. This way the environmental conditions experienced by the fiber can be monitored and the fiber can be used as a distributed sensor. A typical Rayleigh scattering measurement could be the one shown in Fig. 1.2.

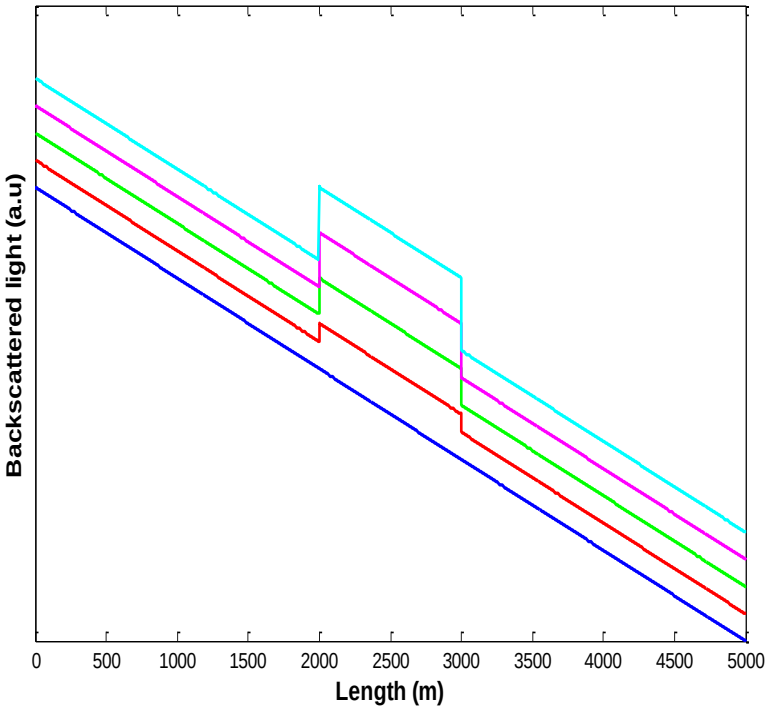

Fig. 1.2. Backscattered light received at the transmitter due to Rayleigh scattering

In Fig. 1.2 different traces are shown. The blue one represents an ideal backscattered profile of a fiber link with no connections/splices. If temperature is increased in a certain area (2,000-3,000 m), the backscattered light in that particular area will be increased (red trace). As temperature is increased, the backscattered light is increased as well (green to cyan traces). This way, the environmental conditions experienced by the fiber can be extracted from the backscattered light profile in relation to time/length.

1.2.2 Raman scattering

Raman scattering is a phenomena caused by non-linear interactions inside the core of an optical fiber. Once the injected power into the fiber has reached a certain level, called threshold power, these interactions start to happen [22].

If a powerful enough beam is travelling through an optical fiber, Raman scattering will take place. When photons are scattered from an atom or a molecule, most of them are elastically scattered (Rayleigh scattering) so the scattered photons have the same energy (frequency) as the incident photons. But a small fraction of these scattered photons will be inelastically scattered, what causes a change in their energy (frequency or wavelength). For example, in a gas, Raman scattering normally occurs due to a change in the vibrational, rotational or electronic state of a molecule [23]. So three different things can happen when photons and matter interact:

- There is no energy exchange between the incident photon and the molecule (Rayleigh scattering).
- The molecule absorbs some energy, as a consequence, the resultant photon has a lower frequency (Stokes scattering).
- The molecule losses some energy, therefore the resultant photon is displaced to a higher frequency (anti-Stokes scattering).

The change of frequency experienced by the photon is around 13 THz. So, the spectrum of the backscattered light could be the one showed in the next figure (Brillouin back-scattered light is also shown).

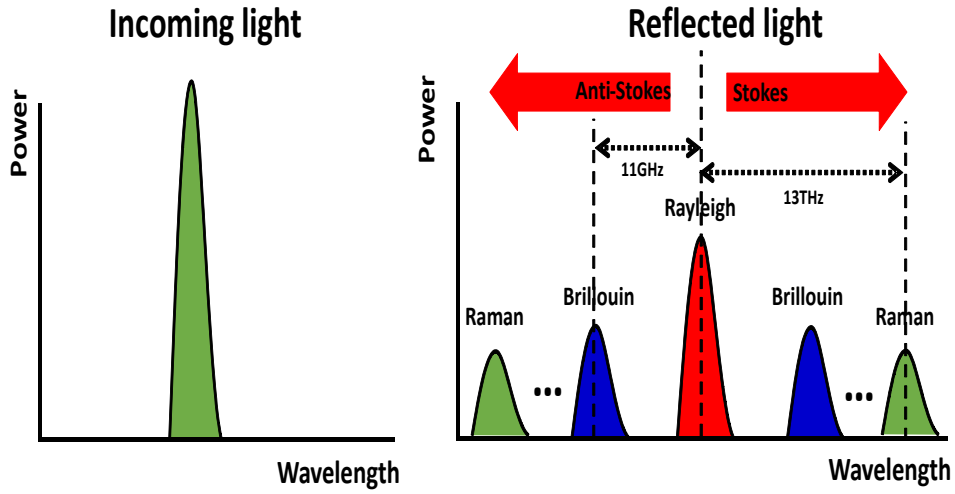

Fig. 1.3. Wavelength profile of the incoming and the backscattered light

The amplitude of the Stokes light is weakly dependent on temperature while the amplitude of the anti-Stokes light depends strongly on temperature. If the amplitudes at both bands are detected and related, the temperature profile of the fiber can be measured [24]. Therefore, if a temperature change occurs in a certain spot in the fiber, the spectrum of the Raman backscattered light changes as it is pictured in the next figure:

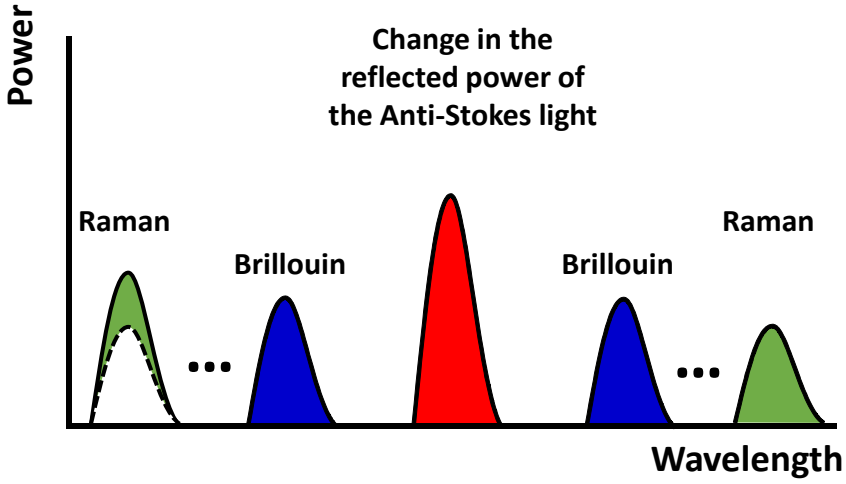

Fig. 1.4. Change in the spectrum of the Raman backscattered light produced by a temperature change

1.2.3 Brillouin scattering

Brillouin scattering is a phenomena similar to Raman scattering due to it also comes from the interaction between matter and light. Raman scattering is caused by the interaction of light with molecules. Nevertheless, Brillouin scattering comes from the interaction between photons and phonons [25].

Brillouin scattering is also an inelastic scattering process. That means that the photon can lose energy (creating a phonon this way) or absorb energy (absorbing a phonon in the process). This change in the energy level of the photon creates a change in its frequency called Brillouin shift in frequency (11 GHz for fused silica at a wavelength around 1.5 μm), and it equals the energy of the absorbed/released quasiparticle. The magnitude of this frequency change depends on the velocity of sound v_s and the wavelength of the light in the glass, and can be expressed this way [26]:

$$\Delta v_B = 2n\frac{v_s}{\lambda} \tag{1.2}$$

where n is the refractive index. The sound velocity, however, depends on the Young's modulus E_0 and density of the glass (ρ):

$$v_s = \left(\frac{E_0}{\rho}\right)^{1/2} \tag{1.3}$$

In consequence, the Brillouin frequency shift can provide information about the material composition of the fiber or the environmental conditions the fiber is experiencing. The spectrum of the Brillouin backscattered light in comparison to other scattering processes is showed in Fig. 1.3.

So, when a temperature/strain change occurs on a certain spot of the fiber, the spectrum of the Brillouin backscattered light changes in frequency as it is shown in Fig. 1.5. This behaviour is superior to an intensity change (Raman scattering) due to the fact that intensity based techniques are more affected by low SNR (central frequency discrimination is easier than amplitude level discrimination in this kind of environment).

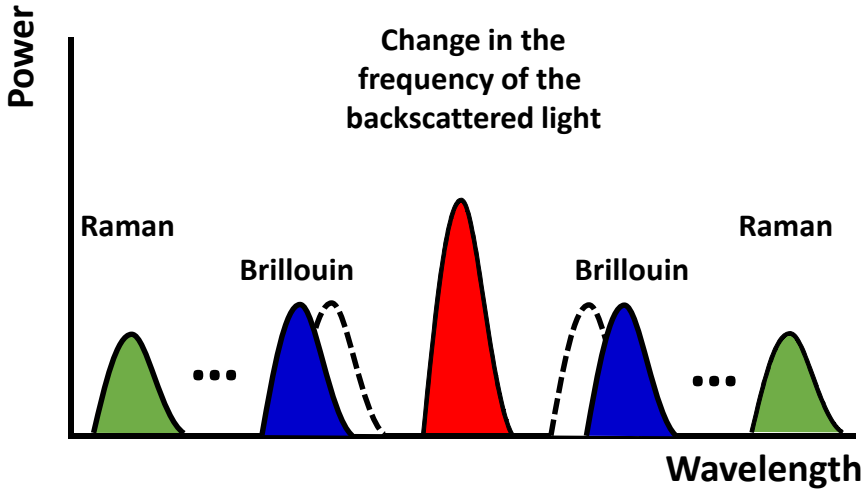

Fig. 1.5. Effect of temperature/strain in Brillouin backscattered light spectrum

Brillouin scattering can be optically stimulated leading to the greatest intensity of the scattering mechanism and consequently to an improved signal-to-noise ratio. This is what is called stimulated Brillouin scattering (SBS) [27]. This phenomena is created by a very strong beam inside the optical fiber. In this case, the variations of the strong beam are going to affect the material via electrostriction or radiation pressure and may induce acoustic vibration in the material. This electrostriction effect creates a grating in the fiber that increases the amount of light that is backscattered, increasing this way the SNR of the technique. So, SBS can be described as a 3-wave interaction involving the incident light (known as pump), the generated acoustic wave and the scattered light.

1.3 Multiplexed sensors

In contrast to distributed sensing in which the whole fiber becomes a sensor, in multiplexed sensing only a particular set of spots along the fiber behave like sensors [12]. FBGs and other kind of reflectors are normally the structures that carry out the sensing part in the multiplexed sensing field. The ability to sense at every position along the fiber is lost but some other characteristics like sensitivity, power efficiency, SNR, interrogation speed or simplicity can be enlarged this way.

1.3.1 FBGs sensors

A fiber Bragg grating is a periodical or quasi-periodical modulation of the refractive index of the core of an optical fiber along its longitudinal axis [17]. This modulation can be created thanks to a phenomena called photosensitivity [28]. Thanks to this phenomena, the refractive index of the core of an optical fiber can be altered by an intense optical radiation of an appropriate wavelength.

These periodical perturbations in the refractive index provoke that part of the incoming light is coupled to different modes causing this way the coherent addition of the multiple contributions, but only at particular wavelengths. In the FBGs, those wavelengths that fulfil the necessary phase condition given by the energy and momentum conservation law are added constructively and they propagate backwards. The wavelength on which the maximal coupling occurs is called the Bragg wavelength. This Bragg wavelength can be expressed as [17]:

$$\lambda_B = 2n_{eff}\Lambda \tag{1.4}$$

where n_{eff} is the effective refractive index of the optical fiber core and Λ is the period of the modulation of the refractive index. The working principle of an FBG is summarized in Fig. 1.6.

One of the principle characteristics of the FBGs is the great versatility to design their spectral features through variation of the spatial separation between consecutive perturbations of the refractive index, the amplitude of the modulation or the modulation profile (apodization). This way, the FBGs have had a very important role in optical communication applications such as filtering [29], dispersion compensation [30] or wavelength dependent optical routing [31]. In addition, FBGs have been used as well as optical sensors [32] thanks to the dependency of their spectral properties on the environmental conditions.

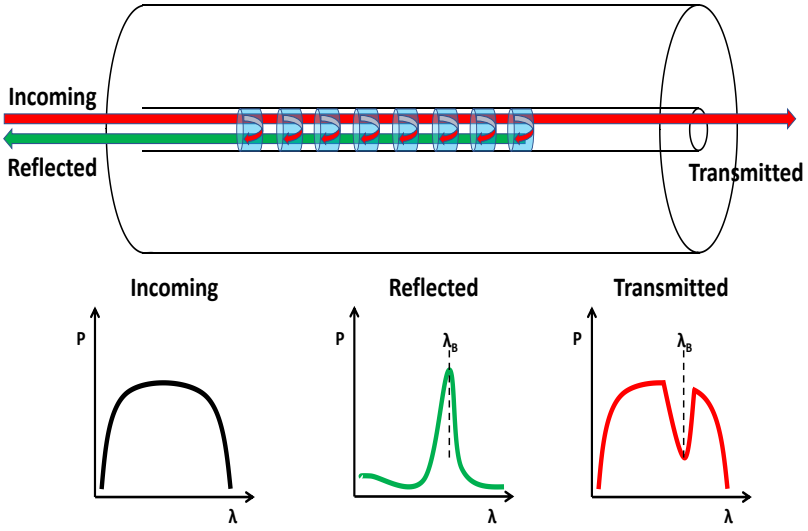

Fig. 1.6. Principle of operation of the FBG

The Bragg wavelength is affected by environmental conditions that change the refractive index or the modulation pitch. The Bragg wavelength variation can be related this way to the different contributions, mainly deformation and temperature:

$$\Delta\lambda_B = \frac{\partial\lambda_B}{\partial\varepsilon}\varepsilon + \frac{\partial\lambda_B}{\partial T}\Delta T \tag{1.5}$$

$$\varepsilon = \frac{\Delta L}{L} \tag{1.6}$$

where ΔT is the temperature variation and ε is the unitary deformation. By substituting (1.4) on (1.5), the following equation is obtained:

$$\Delta\lambda_B = \lambda_B\left[\frac{1}{\Lambda}\frac{\partial\Lambda}{\partial\varepsilon} + \frac{1}{n_{eff}}\frac{\partial n_{eff}}{\partial\varepsilon}\right]\varepsilon + \lambda_B\left[\frac{1}{\Lambda}\frac{\partial\Lambda}{\partial T} + \frac{1}{n_{eff}}\frac{\partial n_{eff}}{\partial T}\right]\Delta T \tag{1.7}$$

In the previous equation the effect on the Bragg wavelength can be divided into two different terms. The first one, represents the dependency of the Bragg wavelength on the deformation and can be expressed as [32]:

$$\Delta\lambda_B = \lambda_B\left[1 - \frac{n^2}{2}[p_{12} - v(p_{11} + p_{12})]\right]\varepsilon \tag{1.8}$$

where p_{11} and p_{12} are the elasto-optic tensor coefficients and v is the Poisson's coefficient.

The second term, which represents the dependency on temperature, can be expressed as [32]:

$$\Delta\lambda_B = \lambda_B \left[\alpha_\Lambda + \frac{1}{n_{eff}} \frac{\partial n_{eff}}{\partial T}\right] \Delta T \tag{1.9}$$

where α_Λ is the thermal expansion coefficient and $\partial n_{eff}/\partial T$ represents the variation of the refractive index in relation to temperature. As the FBG is sensitive to temperature and deformation, sometimes that forces to compensate or isolate the effect of one of the magnitudes in order to measure the other [33].

1.4 Microwave photonics

Microwave photonics (MWP) [18] is an interdisciplinary field in which the interaction between microwave and photonic signals is studied for applications like sensor networks [19], radar, satellite communications, warfare systems or signal processing [34]. MWP has been attracting a lot of attention from the research community in order to discover new techniques for such applications. The major functions of MWP are photonic generation, processing and control and distribution of microwave signals.

1.4.1 Microwave photonics for optical sensing

The basic layout of a MWP system [35] is depicted in Fig. 1.7. The starting point is an RF signal with two sidebands centred at ±Ω. This signal drives the modulator to up-convert this signal to the optical spectrum, being centred now at ω±Ω, being ω the central frequency of the optical source. This signal is processed by the optical system, characterized by a transfer function H(ω).

Finally an optical detector is employed to down-convert the signal to the MW domain again so the electrical transfer function H(Ω) can be studied.

Such a system can be used in the sensing field thanks to the dependency of the optical transfer function on the measurand ε, H(ω)→H(ω,ε). The recovered RF signal will change accordingly to the measurand ε, making this way possible to extract the measurand from the changes in the electrical transfer function, H(Ω).The resolution of the sensor would be related to the accurate acquisition of the electrical response. While optical spectrum analyzers (OSA) show low resolution (gigahertz or hundreds of megahertz step), vector network analyzers (VNA) or signal analyzers (SA) can work under extremely high resolutions (kilohertz scale or even less). This can bring some benefits to the sensor interrogation in terms of sensitivity and accuracy.

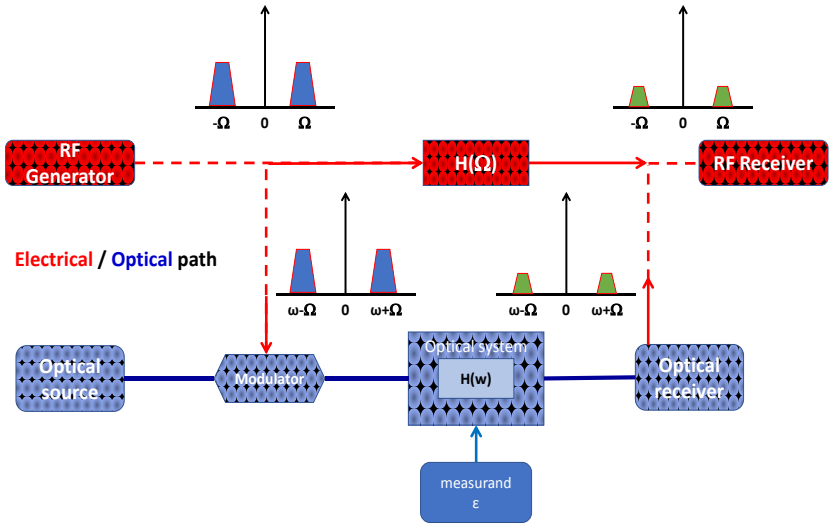

Fig. 1.7. Basic layout of a MWP system

One of the simpler sensors interrogated using MWP techniques is shown in Fig. 1.8 [36]. It is a hot spot detector based in a long standard FBG (10 cm). Initially, the majority of the incoming light is reflected at the beginning of the FBG. If there is a hot spot along the FBG, the Bragg wavelength of that particular section shifts, and light is reflected by that section as well. This way, a 2 tap MWP filter is created, and studying the electric response of the system, the location of the hot spot in relation to the input edge of the FBG can be calculated.

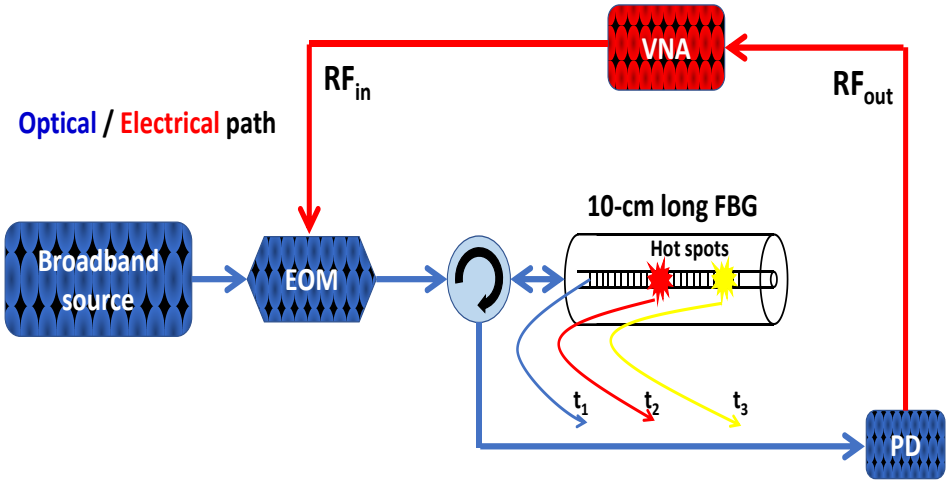

Fig. 1.8. Schematic view of the hot spot detection system (EOM: electro-optic modulator, PD: photodetector, VNA: vector network analyzer)

In Fig. 1.9 the ideal electrical response for different spatial separations between the beginning of the FBG and the hot spot are shown. As can be seen, the electrical response of the system changes as the hot spot position does, being possible this way to locate the hot spot along the FBG.

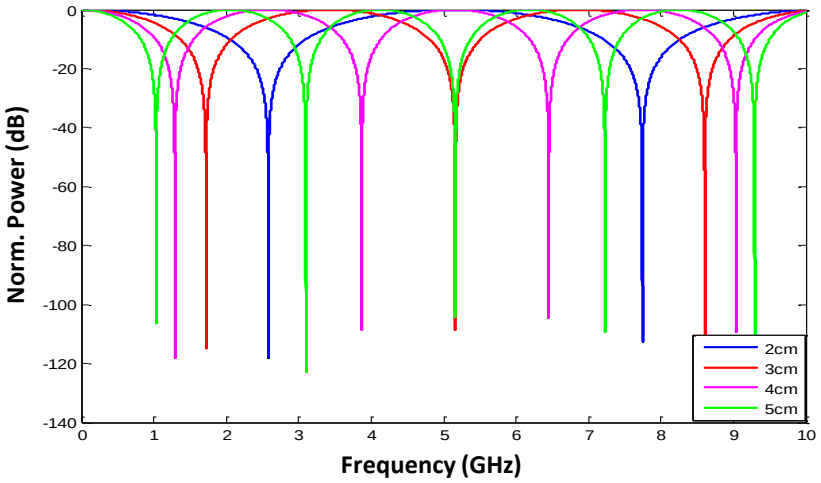

Fig. 1.9. Electrical response of the system showed in Fig. 9 for different separations between the beginning of the FBG and the hot spot

References

[1] K. Thyagarajan; Ajoy Ghatak, "Optical Fiber Sensors," in *Fiber Optic Essentials* , , IEEE, 2007, pp.

[2] W. Kam *et al.*, "Compact and Low-Cost Optical Fiber Respiratory Monitoring Sensor Based on Intensity Interrogation," in *Journal of Lightwave Technology*, vol. 35, no. 20, pp. 4567-4573, 15 Oct.15, 2017.

[3] X. Fan, G. Yang, S. Wang, Q. Liu and Z. He, "Distributed Fiber-Optic Vibration Sensing Based on Phase Extraction From Optical Reflectometry," in *Journal of Lightwave Technology*, vol. 35, no. 16, pp. 3281-3288, 15 Aug.15, 2017.

[4] G. Liu, J. Yu, L. Xie, Z. Dou, W. Zhang and Z. Yue, "Polarization-Dependent Optical Sensor Based on Reduced Graphene Oxide," in *IEEE Photonics Technology Letters*, vol. 29, no. 9, pp. 767-770, 1 May1, 2017.

[5] Z. Guan, A. P. Zhang, R. Liao and S. He, "Wavelength Detection of Coherence-Multiplexed Fiber-Optic Sensors Based on Long-Period Grating Pairs," in *IEEE Sensors Journal*, vol. 7, no. 1, pp. 36-37, Jan. 2007.

[6] J. Zhu, A. P. Zhang, T. Xia, S. He and W. Xue, "Fiber-Optic High-Temperature Sensor Based on Thin-Core Fiber Modal Interferometer," in *IEEE Sensors Journal*, vol. 10, no. 9, pp. 1415-1418, Sept. 2010.

[7] J. W. Arkwright, I. D. Underhill, S. A. Maunder, A. Jafari, N. Cartwright and C. Lemckert, "Fiber Optic Pressure Sensing Arrays for Monitoring Horizontal and Vertical Pressures Generated by Traveling Water Waves," in *IEEE Sensors Journal*, vol. 14, no. 8, pp. 2739-2742, Aug. 2014.

[8] L. Ma, Y. Qi, Z. Kang and S. Jian, "All-Fiber Strain and Curvature Sensor Based on No-Core Fiber," in *IEEE Sensors Journal*, vol. 14, no. 5, pp. 1514-1517, May 2014.

[9] C. Huang, W. Xie, M. Yang, J. Dai and B. Zhang, "Optical Fiber Fabry–Perot Humidity Sensor Based on Porous Al_2O_3Film," in *IEEE Photonics Technology Letters*, vol. 27, no. 20, pp. 2127-2130, 15 Oct.15, 2015.

[10] D. M. Klein, E. G. Yukihara, E. Bulur, J. S. Durham, M. S. Akselrod and S. W. S. McKeever, "An optical fiber radiation sensor for remote detection of radiological materials," in *IEEE Sensors Journal*, vol. 5, no. 4, pp. 581-588, Aug. 2005.

[11] G. Yan *et al*., "Fiber-Optic Acetylene Gas Sensor Based on Microstructured Optical Fiber Bragg Gratings," in *IEEE Photonics Technology Letters*, vol. 23, no. 21, pp. 1588-1590, Nov.1, 2011.

[12] Eric Udd; William B. Spillman, "Distributed and Multiplexed Fiber Optic Sensors," in *Fiber Optic Sensors: An Introduction for Engineers and Scientists* , , Wiley, 2011, pp.

[13] A. K. Sang, M. E. Froggatt, D. K. Gifford, S. T. Kreger and B. D. Dickerson, "One Centimeter Spatial Resolution Temperature Measurements in a Nuclear Reactor Using Rayleigh Scatter in Optical Fiber," in *IEEE Sensors Journal*, vol. 8, no. 7, pp. 1375-1380, July 2008.

[14] M. A. Soto, P. K. Sahu, G. Bolognini and F. Di Pasquale, "Brillouin-Based Distributed Temperature Sensor Employing Pulse Coding," in *IEEE Sensors Journal*, vol. 8, no. 3, pp. 225-226, March 2008.

[15] Jonghan Park *et al*., "Raman-based distributed temperature sensor with simplex coding and link optimization," in *IEEE Photonics Technology Letters*, vol. 18, no. 17, pp. 1879-1881, Sept. 2006.

[16] M. Wang, M. Yang, J. Cheng, G. Zhang, C. R. Liao and D. N. Wang, "Fabry–Pérot Interferometer Sensor Fabricated by Femtosecond Laser for

Hydrogen Sensing," in *IEEE Photonics Technology Letters*, vol. 25, no. 8, pp. 713-716, April15, 2013.

[17] K. Thyagarajan; Ajoy Ghatak, "Fiber Bragg Gratings," in *Fiber Optic Essentials* , , IEEE, 2007, pp.

[18] J. Yao, "Microwave Photonics," in *Journal of Lightwave Technology*, vol. 27, no. 3, pp. 314-335, Feb.1, 2009.

[19] X. Yi, S. X. Chew, L. Li, R. Minasian and L. Nguyen, "Microwave photonics for high performance sensing," *2017 16th International Conference on Optical Communications and Networks (ICOCN)*, Wuzhen, 2017, pp. 1-3.

[20] D. Marcuse, "Rayleigh scattering and the impulse response of optical fibers," in *The Bell System Technical Journal*, vol. 53, no. 4, pp. 705-715, April 1974.

[21] K. Tajima, "Low-loss optical fibers realized by reduction of Rayleigh scattering loss," *OFC '98. Optical Fiber Communication Conference and Exhibit. Technical Digest. Conference Edition. 1998 OSA Technical Digest Series Vol.2 (IEEE Cat. No.98CH36177)*, San Jose, CA, USA, 1998, pp. 305-306.

[22] R. H. Stolen, "Nonlinearity in fiber transmission," in *Proceedings of the IEEE*, vol. 68, no. 10, pp. 1232-1236, Oct. 1980.

[23] J. Duardo, F. Johnson and L. Nugent, "Some new aspects in stimulated Raman scattering from hydrogen gas," in *IEEE Journal of Quantum Electronics*, vol. 4, no. 6, pp. 397-403, June 1968.

[24] M. A. Farahani and T. Gogolla, "Spontaneous Raman scattering in optical fibers with modulated probe light for distributed temperature Raman remote sensing," in *Journal of Lightwave Technology*, vol. 17, no. 8, pp. 1379-1391, Aug. 1999.

[25] D. Sealer and H. Hsu, "Stimulated Brillouin scattering as a parametric interaction," in *IEEE Journal of Quantum Electronics*, vol. 1, no. 3, pp. 116-124, June 1965.

[26] Y. Aoki, K. Tajima and I. Mito, "Input power limits of single-mode optical fibers due to stimulated Brillouin scattering in optical communication systems," in *Journal of Lightwave Technology*, vol. 6, no. 5, pp. 710-719, May 1988.

[27] A. Djupsjobacka, C. Jacobsen and B. Tromborg, "Dynamic stimulated Brillouin scattering analysis," in *Journal of Lightwave Technology*, vol. 18, no. 3, pp. 416-424, March 2000.

[28] R. M. Atkins, P. J. Lemaire, T. Erdogan and V. Mizrahi, "Mechanisms of enhanced UV photosensitivity via hydrogen loading in germanosilicate glasses," in *Electronics Letters*, vol. 29, no. 14, pp. 1234-1235, 8 July 1993.

[29] M. Lv, D. Feng and D. Yang, "Synthesis of special fiber Bragg grating filters by layer peeling algorithm," *2009 Conference on Lasers & Electro Optics & The Pacific Rim Conference on Lasers and Electro-Optics*, Shanghai, 2009, pp. 1-2.

[30] Y. J. Lee, J. Bae, K. Lee, J. Jeong and S. B. Lee, "Tunable Dispersion and Dispersion Slope Compensator Using Strain-Chirped Fiber Bragg Grating," in *IEEE Photonics Technology Letters*, vol. 19, no. 10, pp. 762-764, May15, 2007.

[31] N. S. Moon, C. S. Goh, S. K. Khijwania and K. Kikuchi, "Experimental demonstration of fiber Bragg grating based optical cross-connect for WDM networks," *Proceedings 27th European Conference on Optical Communication (Cat. No.01TH8551)*, Amsterdam, Netherlands, 2001, pp. 538-539 vol.4.

[32] A. D. Kersey *et al*., "Fiber grating sensors," in *Journal of Lightwave Technology*, vol. 15, no. 8, pp. 1442-1463, Aug. 1997.

[33] Y. S. Hsu, Likarn Wang, Wen-Fung Liu and Y. J. Chiang, "Temperature compensation of optical fiber Bragg grating pressure sensor," in *IEEE Photonics Technology Letters*, vol. 18, no. 7, pp. 874-876, April 1, 2006.

[34] R. A. Minasian, "Photonic signal processing of microwave signals," in *IEEE Transactions on Microwave Theory and Techniques*, vol. 54, no. 2, pp. 832-846, Feb. 2006.

[35] J. Hervás *et al*., "Microwave Photonics for Optical Sensors," in *IEEE Journal of Selected Topics in Quantum Electronics*, vol. 23, no. 2, pp. 327-339, March-April 2017, Art no. 5602013.

[36] Amelia Lavinia Ricchiuti, David Barrera, Salvador Sales, Luc Thevenaz, and José Capmany, "Long fiber Bragg grating sensor interrogation using discrete-time microwave photonic filtering techniques," Opt. Express 21, 28175-28181 (2013)

Chapter 2

The wavelength to radio-frequency delay mapping technique

2.1 Introduction

FBGs have been used extensively in the sensing field for quite a long time [1-5]. The ability to record environmental parameters, such as strain [6-7] or temperature [8-9], in its physical attributes (Bragg wavelength) has granted FBGs a key role in the multiplexed sensing domain [10-12].

The multiplexed sensing field shows a trend towards having a large number of discrete sensors featuring a large sensitivity, small resolution and an increasing interrogation speed. In order to have a large number of discrete sensors in a single fiber, sensors may show the same spectral properties [13].

Traditional techniques are not very suitable to interrogate this kind of devices. The OTDR technique [14] is able to locate reflectors in time/space but it is not able to show the Bragg wavelength drift when one or several FBGs are under a temperature/pressure change. The OFDR technique [15] is able to locate the sensors in time/space and to measure the Bragg wavelength change, but it is a costly and bulky approach [16]. Besides, the interrogation time of such techniques ranges from few to tens of seconds or even more.

In order to satisfy these new requirements novel techniques have been studied in the past years to improve the performance of the traditional ones. Microwave Photonics [17-19] techniques are destined to have a key role in order to get the fulfilment of these new requirements [20].

In this chapter, a new interrogation technique based on the so called wavelength to radio-frequency delay mapping [21-22] is used to retrieve the sensing information of an array of 7 cascaded standard FBGs. This technique can be viewed as a modification of the incoherent OFDR technique [15-16]. The Bragg wavelength of the FBGs are mapped into radio-frequency delays by use of a dispersive media, implemented with a single-mode fiber link. These delays are determined in the impulse response of the system, calculated through inverse fast Fourier transformation (IFFT) of the electrical frequency response of the system. To illustrate the flexibility of the proposed concept further, neither the differences between the Bragg wavelengths of adjacent FBGs in the cascade, nor their shapes, widths, or reflected power, are uniform. As will be shown in this chapter, even in this general scenario the wavelength to radio-frequency delay mapping technique together with numerical post processing of the

retrieved frequency-domain traces allow for an effective interrogation of the multiplexed FBG sensor.

2.2 Array fabrication

The array was fabricated using the fabrication setup of the research group. It was set up fifteen years ago but in the recent period it has been updated to overcome the problem of inscribing FBGs arbitrarily in any of the cores of a multicore fiber.

The setup architecture can actually be divided into three subsystems: the laser beam conditioning subsystem, the optical fiber positioning subsystem and the core tracking subsystem.

The laser beam conditioning subsystem consists of a continuous-wave frequency-doubled Argon-ion laser emitting a maximum optical power of 100 mW at an optical wavelength of 244 nm; a mirror mounted in a piezo-electric transducer, which is able to induce a vertical deflection in the laser beam; two cylindrical lenses that tune the height and the width of the laser beam; and the phase mask that creates the diffraction pattern that inscribes the FBG in the fiber core. All these elements are placed on top of a high-precision translation stage that moves parallel to the optical fiber and the incoming laser beam.

The optical fiber positioning subsystem controls the 3D spatial position of the optical fiber. A pair of rotation stages that are placed on top of two three-axis translation stages hold the optical fiber. These rotation stages allow placing the cores into the proper spatial location for the grating inscription. The whole subsystem can also adjust the distance of the optical fiber to the phase mask. This distance is verified by a vision system that is placed over the inscription setup and aligned to the phase mask.

The core tracking subsystem is the responsible for optimizing the irradiation of the laser beam into a particular core of the MCF (or into the single core of a standard single mode fiber). It deflects the laser beam by moving the mirror mounted in the piezo-electric transducer. Actually, this subsystem turns to be critical when a very narrow laser beam is used. In addition, it provides information about the spatial position of the different cores within the cross-sectional area of the optical fiber. The core tracking is based on the 3.10-eV (400-nm) photoluminescence generated by the UV radiation produced from GeO defects in a germanium-doped silica glass [23]. The intensity of the guided photoluminescence is proportional to the UV power absorbed in the core. However, the detection of this guided photoluminescence is usually hampered by the noise. To alleviate this limitation, the core tracking subsystem generates a small sinusoidal signal that is applied to the piezo-electric transducer that vertically deflects the laser beam. This produces a modulation at the photodetected signal that is filtered and demodulated by a lock in amplifier.

When the laser beam aligns with the target core, the photodetected signal and the signal applied to the piezo-electric transducer have the same frequency. If the laser beam is not properly aligned, a signal with twice the frequency is generated instead. In that case, the output of the lock in amplifier is digitally processed to generate a DC signal that corrects the laser beam vertical position.

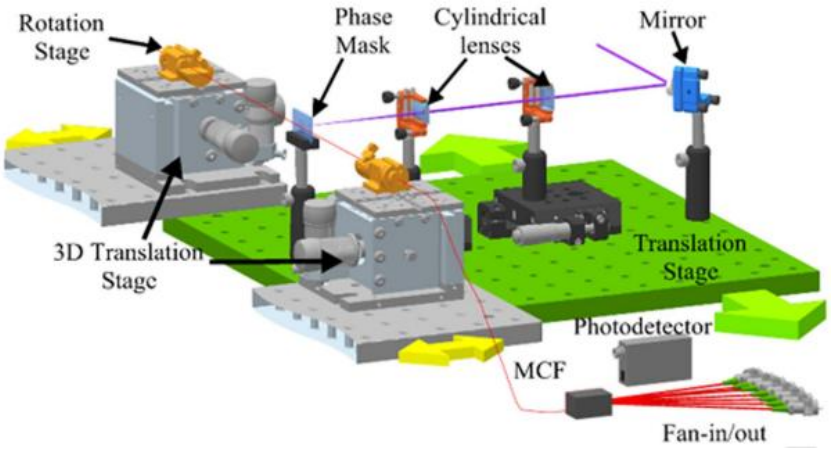

Fig. 2.1. Schematic view of the fabrication setup

2.3 Dispersion measurement

The key question in the wavelength to radio-frequency delay mapping is the dispersive media. It has the role to transform the Bragg wavelength change experienced by an FBG into a delay change of the sample reflected by that FBG. The dispersive media chosen to prove the performance of this technique was 6.83 km of standard single-mode fiber. It was selected mainly due to its simplicity.

The dispersion of this fiber had to be measured through the entire measurement window (in a discrete way) because on the contrary it would lead to an accuracy reduction and an increment on resolution.

The technique used for measuring the dispersion of the fiber was the carrier suppression effect [24]. This effect occurs when an analog modulation with two sidebands is photodetected after transmission through an optical fiber link. The different dispersion both sidebands experience creates a phase-shift between both sidebands, leading some frequencies to be cancelled due to the orthogonal addition. Depending either on the length of the fiber link or on the wavelength of the incoming light, the frequencies in which fading effects are present, are

different. Taking into account the fiber length, if the first frequency erased is measured, the dispersion of the fiber can be calculated using this formula:

$$\Omega = \sqrt{\frac{(2k+1)\pi}{\beta_2 z}} \tag{2.1}$$

where Ω is the angular frequency, β_2 is the first order dispersion, z is the fiber length and k would be 0 in this case. Therefore, if the frequency value of the notch is measured and the length of the fiber is known, the β_2 value of the working wavelength can be calculated trivially. The typical appearance of the electrical frequency spectrum, when the carrier suppression effect takes place, is this:

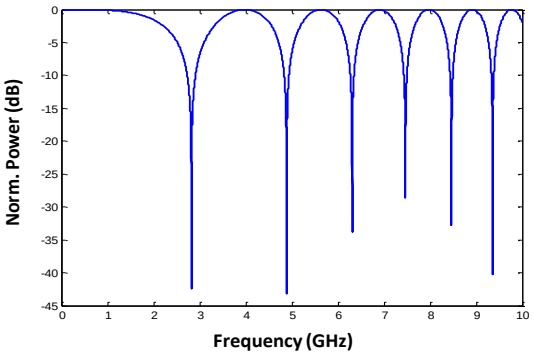

Fig. 2.2. Effect of the carrier suppression effect in the electrical response (simulation)

As can be seen different values for k (2.1) give the different notches of the response, but only the first notch was used in this measurement in order to calculate the dispersion value at a given wavelength. The working wavelengths in which the experimental measurements were going to be performed to prove the validity of the interrogation technique were from 1,530 to 1,580 nm. The carrier suppression effect was studied in four different wavelengths (1,530, 1,550, 1,565 and 1,580 nm). The setup used to calculate the electrical response at the different working wavelengths is shown in this figure:

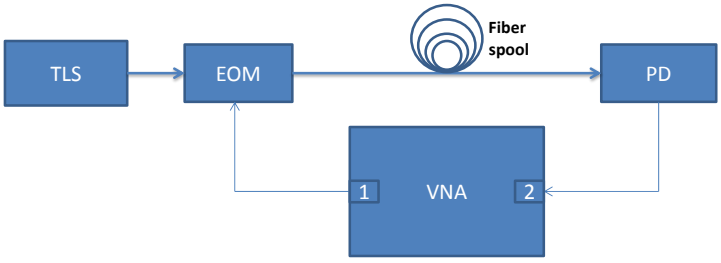

Fig. 2.3. Schematic diagram of the setup used to measure the dispersion of the fiber

The light coming from a tunable laser (TLS) is modulated in an electro-optic modulator (EOM), by the electric signal coming from port 1 of a Vector Network Analyzer (VNA), before being injected to the fiber spool acting as the dispersive media. After propagation through the dispersive media the light is photodetected in the photodetector (PD) and it is headed to the port 2 of the VNA, which calculates the electrical response. The dispersion values calculated are shown in table 2.1. As can be seen clearly, the dispersion value becomes larger with wavelength, in agreement with the expected behavior of a standard fiber.

Wavelength (nm)	D (ps/(km·nm))
1,530	16.467
1,550	17.261
1,565	18.012
1,580	18.907

Table 2.1. Dispersion calculated values for different working wavelengths

The second order dispersion was calculated through polynomial fitting. The value found was 0.05 ps/(nm^2·km) although this value was not taken into account in order not to enlarge the complexity and computational effort of the interrogation technique. Instead, a linear approximation was performed between the computed dispersion values calculated by the electrical responses measured. The dispersion values used for the experimental measurements of the interrogation technique are shown in this figure:

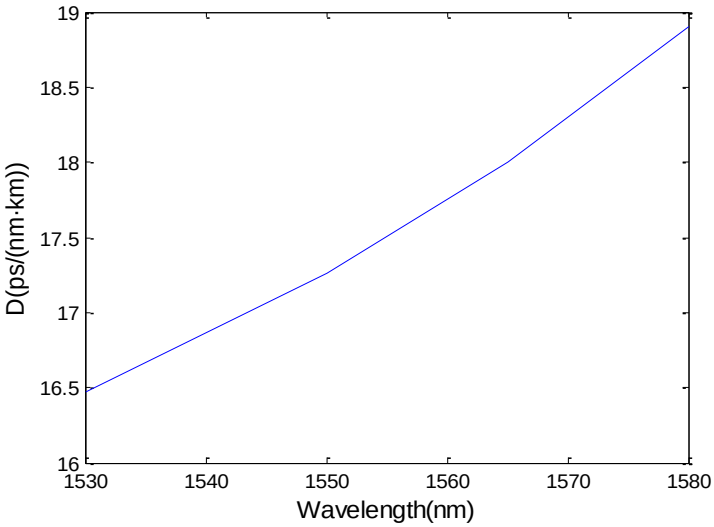

Fig. 2.4. Dispersion values calculated for the experimental implementation of the interrogation technique

It is clear that the decision to not use the second order dispersion is going to create some measurement errors. This error was computed for different Bragg wavelength changes (0.6, 1 and 5 nm) and are shown in Fig. 2.5. For the precision that was set as objective for the interrogation technique (around 10 pm), the removal of the second order dispersion effect has negative consequences only when the Bragg wavelength change is larger than 1 nm, which represents a 100 ^{o}C temperature change, far larger than the expected changes measured in the experiments.

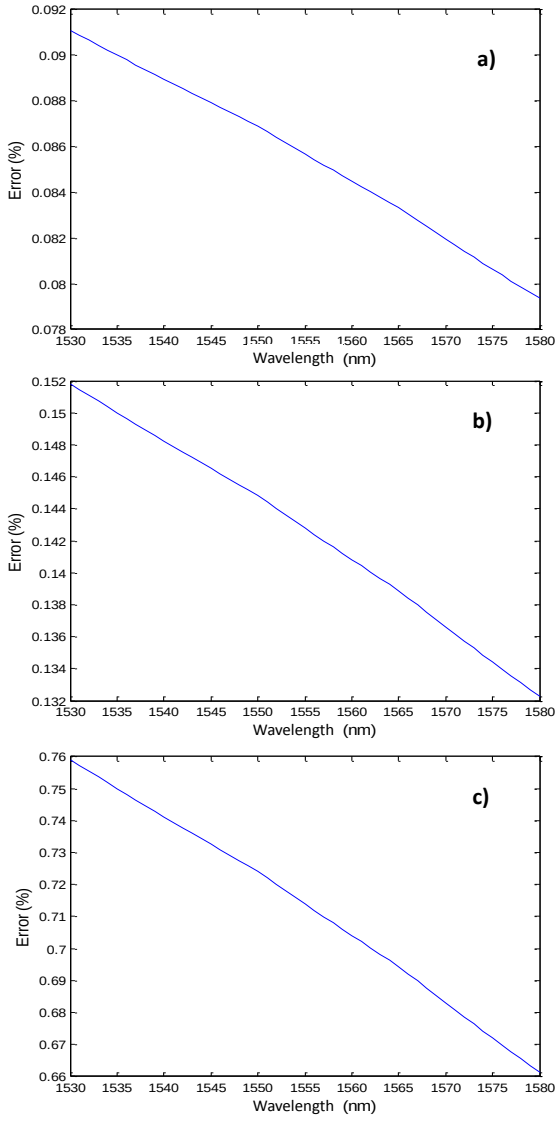

Fig. 2.5. Computed error of not taking into account the second order dispersion for different wavelength changes: a) 0.6 nm, b) 1 nm, c) 5nm)

2.4 Principle of operation

The setup used to retrieve the sensing information of the array of 7 FBGs, considered here as the device under test (DUT), is depicted in Fig. 2.6. It is based on the measurement of the electrical frequency response *H(Ω)* relating the output and input RF signals, as measured by a vector network analyzer (VNA), when the DUT is considered as an optical transmission system.

The output power of a C-band broadband optical source (BBS), implemented here by use of a SLED, is modulated by an electro-optic modulator (EOM) by the RF signal from the VNA output port. This optical signal is then launched into the DUT by means of a circulator. In the DUT, different spectral slices of the modulated BBS are reflected by the FBGs and routed to the dispersive element, composed of 6.83 km of single mode fiber (SMF). This dispersive element is used to map the Bragg wavelengths of the individual FBGs into electrical delays of the RF modulating waveforms, so that shifts in Bragg wavelength due to temperature or strain induce group delay shifts. After photodetection (PD) the RF signal is directed to the VNA input port and the electrical response of the system is measured as function of the input RF tone, Ω. The electrical response has the form [25]:

$$H(\Omega) = \sum_{k=0}^{N-1} a_k e^{-j\Omega\tau_k} \tag{2.2}$$

where N is the number of FBGs or samples, $a_k > 0$ is the sample weight, proportional to the FBG reflectivity and thus positive, and τ_k is the sample delay, which is given by the group delay $\tau(\lambda)$ experienced by the k-th Bragg wavelength, $\tau_k = \tau(\lambda_{Bk})$, in the SMF dispersive delay line. The frequency response (2.2) is thus the superposition of N oscillations in frequency, and the

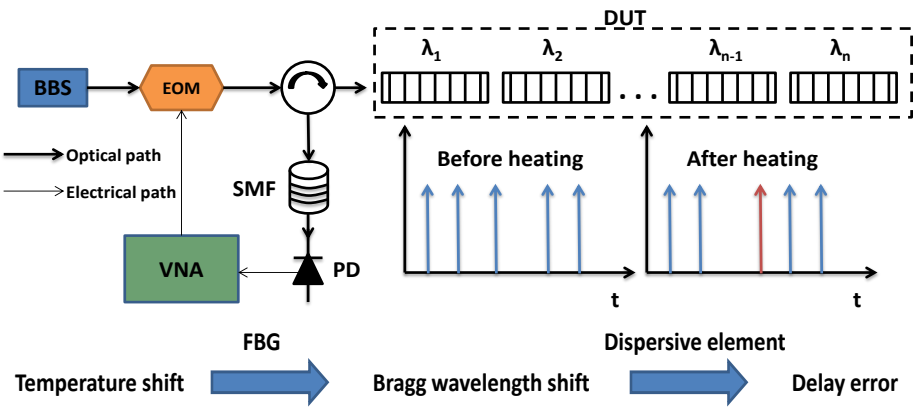

Fig. 2.6. Schematic view of the setup used for the experimental measurements and principle of operation

sample delays, which determine the corresponding Bragg wavelengths, can be extracted by an IFT.

VNA traces provide a discrete version of the amplitude and phase of function $H(\Omega)$ in a range of positive frequencies. Denoting the scanning frequency interval as $0 < \Omega < 2\pi B$, with B the measurement bandwidth in Hertz, the IFT of (2.2) is:

$$h_B(\mathrm{t}) = \sum_{k=0}^{N-1} a_k e^{j\pi B(t-\tau_k)} \,\mathrm{sinc}[\mathrm{B}(t-\tau_k)] \tag{2.3}$$

where $\mathrm{sinc}(x)=\sin(\pi x)/(\pi x)$ and the delays can be determined from the N peak positions of the *sinc* pulses in the amplitude of the impulse response. The peaks or pulses are assumed isolated from each other so that their overlap is negligible. This impulse response (2.3) is a complex response obtained by IFT from the raw VNA traces in the single-sided, positive-frequency range. As a response in the electrical domain that compares input and output voltage waveforms, the link's true electrical impulse response is a real quantity, which can be retrieved from VNA data through IFT after the extension to negative frequencies by use of the hermiticity condition $H(-\Omega) = H(\Omega)^*$. However, this extension would require doubling the initial data string with the subsequent numerical effort, and is not necessary in the present method since the delays can be determined directly from (2.3).

From $\tau_k = \tau(\lambda_{Bk})$, a temperature or strain measurement method can be built by comparing the delays $\tau_k^0 = \tau(\lambda_{Bk}^0)$ when the DUT is in a reference position, free of strain and at a given temperature, with the impulse response when one or several FBGs undergo a shift in Bragg wavelength due to a temperature or strain change, $\tau_k = \tau(\lambda_{Bk}^0 + \Delta\lambda_{Bk})$. Delay shifts $\Delta\tau_k = \tau_k - \tau_k^0$ are related to wavelength shifts according to:

$$\frac{\Delta\tau_k}{\Delta\lambda_{Bk}} = \left.\frac{d\tau}{d\lambda}\right|_{\lambda=\lambda_{Bk}} = D(\lambda_{Bk})\,\mathrm{L} \tag{2.4}$$

where $D(\lambda)$ is the fiber's dispersion at wavelength λ and L the fiber length. Then, only the FBG temperature/strain coefficient is needed to turn this Bragg wavelength shift into a temperature or strain shift.

In (2.4) it has been neglected second-order dispersion effects in the delay shifts induced by wavelength shifts. In the 6.83-km SMF coil, typical shifts of $\Delta\lambda_{Bk} \sim$ 1 nm induce variations $|D(\lambda_{Bk} + \Delta\lambda_{Bk}) - D(\lambda_{Bk})|L = S(\lambda_{Bk})L < 0.4$ ps/nm with respect to $D(\lambda_{Bk})L \sim 116$ ps/nm, which implies a relative accuracy of $\sim 0.4/116 \sim 4\times10^{-3}$ in the determination of $\Delta\lambda_{Bk}$. For $\Delta\lambda_{Bk} \sim 1$ nm, higher-order dispersion

corrections to (2.4) are to be taken into account for target resolutions ≤ 4 pm, otherwise they can be neglected as is the case in this experiments.

When the IFT is calculated from discrete data $H[\Omega_n]$, it is known [26] that the difference $\Delta t = t_{n+1}-t_n$ between sampling instants in the retrieved impulse response $h_B[t_n]$ is given by the inverse of the frequency span of the initial data, $H[\Omega_n]$. If the single-sided raw data from the VNA are used in the IFT, then $\Delta t=1/B$. However, this procedure cannot determine accurately the position of the delays in $h_B(t)$ since, as given by (2.3), they are embedded in a *sinc* peak of width between zeroes equal to $2/B$. So, the sinc pulse width depends on the bandwidth of the electrical measurement (2.3). The higher the bandwidth, the narrower the sinc sample, as can be seen in Fig. 2.7 where the samples of an FBG in a reference position and after being heated are shown for different bandwidth in the electrical measurement.

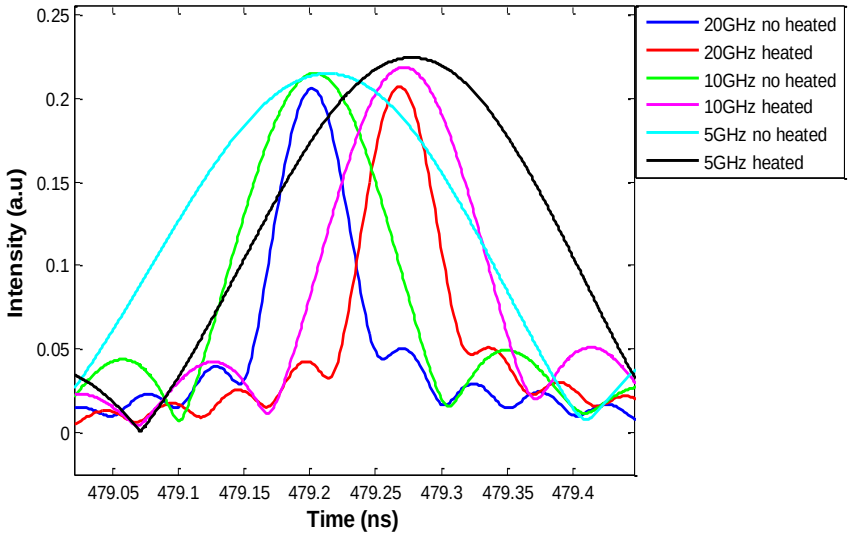

Fig. 2.7. Samples of an FBG in a reference position and when it has been heated for different bandwidths (20, 10 and 5 GHz)

The standard numerical method to interpolate the discrete $h_B[t_n]$ trace in order to clearly resolve the peaks, consists in numerically enlarging the bandwidth to $B'>B$ by adding zeroes to the initial data $H[\Omega_n]$, a procedure that is referred to as zero padding. The difference between sampling points in the trace $h_B[t'_n]$ so obtained is reduced by the ratio of bandwidths $F= B'/B$, i.e., $\Delta t' = 1/B' =\Delta t /F$.

As is well-known in digital signal processing [26], if zero padding is used to estimate the Fourier transform of a number of sinusoids such as (2.2), the resolution is ascribed to the width of the smallest spectral line, i.e., to the width

2/*B* of the *sinc* peak in (2.3). In this regard, it is clear that zero padding does not increase resolution, just interpolates the Fourier transform. In this case, however, the sensor resolution is ascribed to the ability to determine the peak positions in time and is given by $\Delta t' = 1/(B')$. Therefore, zero padding allows for an increase of resolution without an increase in measurement bandwidth. Conversely, zero padding can be used to reduce the measurement bandwidth *B* for a given resolution Δt, by compensating the decrease in bandwidth with a higher factor *F*. It can be used to reduce the dispersion device length needed to have the same Bragg wavelength resolution also by reducing the sampling ratio in the impulse response. It is shown in Fig. 2.8. To have a 10 GHz electrical bandwidth means that the temporal distance between consecutive points in the impulse response is 0.1 ns. To be able to detect a 10 pm change in the Bragg wavelength of a given FBG with no zero padding being used, the length of the fiber needed would be 588 km. However, if the number of points is increased a hundred-fold performing zero padding, the temporal sampling is now 1 ps and the dispersive media length needed would be just 5.88 km.

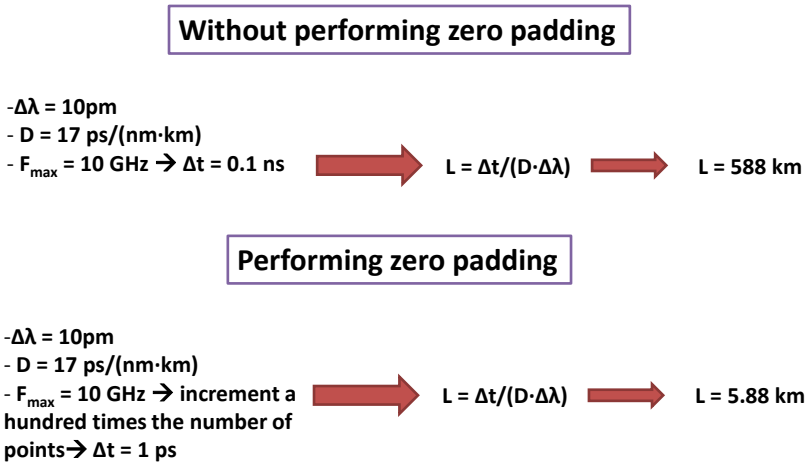

Fig. 2.8. Zero padding allows to reduce the length of the dispersive media for the same resolution

In Fig. 2.9 it is presented an example of the proposed procedure, where simulated data are used to determine the delay τ_k in the impulse response associated to a single FBG when the reflector is in a reference position (blue trace) or heated (red), resulting in a small variation of the peak's center. In the left hand side, simulated data (10,001 points) in a bandwidth B = 2 GHz result in temporal traces with sampling step $\Delta t = 1/B$ = 0.5 ns, unable to resolve the temperature change. By contrast, in the right side the data trace was zero-padded to one million points, thus increasing the effective bandwidth by a factor F=100 up to 200 GHz. After IFT, the impulse response trace is sampled at $\Delta t'$ = 5 ps, revealing the structure of the *sinc* pulse. In this situation, the temperature change can be clearly resolved.

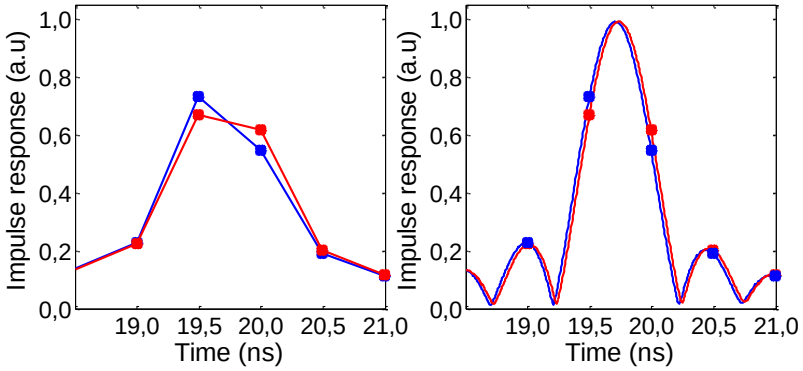

Fig. 2.9. Simulation of an FBG peak in the impulse response for two different situations. Blue trace: FBG at the initial situation. Red trace: FBG after experiencing a temperature change. Left: without zero padding, right: with zero padding. The dots are the values without zero padding (same as on a)), plotted for comparison.

2.5 Experimental measurements

As mentioned in the previous section, the DUT consisted on seven FBGs at different Bragg wavelengths. The widths and shapes of the reflected spectrum were also different, as shown in Fig. 2.10. The variations in reflected power are caused by the use of a SLED with non-uniform spectral power. Electrical measurements were performed following the scheme in Fig. 2.6 in a bandwidth B = 20 GHz. Due to the small length (6.83 km) of SMF no carrier suppression effects were observed within this frequency span. In any case, carrier suppression amounts to low-pass filtering the electrical response (2.2), and thus induce an additional widening of the peaks in the impulse response (2.3), but does not change their positions. The proposed method is expected to tolerate situations with moderate carrier suppression, or other low-pass filtering effects such as moderate limitations in modulation or detection bandwidths.

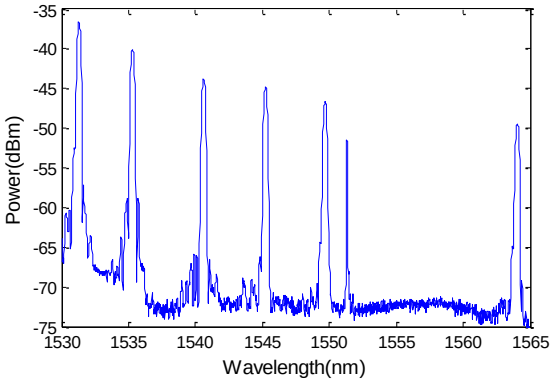

Fig. 2.10. Reflected spectrum of the FBGs array

The measurements were performed by scanning the system's 20-GHz electrical response with 32,000 data points at an intermediate-frequency bandwidth of 1 kHz. The scanning or acquisition time is ~20 s. At the same time, the optical spectrum reflected by the FBGs was monitored in an optical spectrum analyzer (OSA) in order to have a comparative measurement of the shifts in Bragg wavelengths, which were induced by heating the DUT at different positions. In Fig. 2.11 are shown the shifts observed in the OSA when the FBG at 1,540.6 nm was heated. The reference FBG position is determined by a Bragg wavelength of 1,540.6067 nm at room temperature, which shifts by 0.5711 nm to a final Bragg wavelength of 1,541.1778 nm.

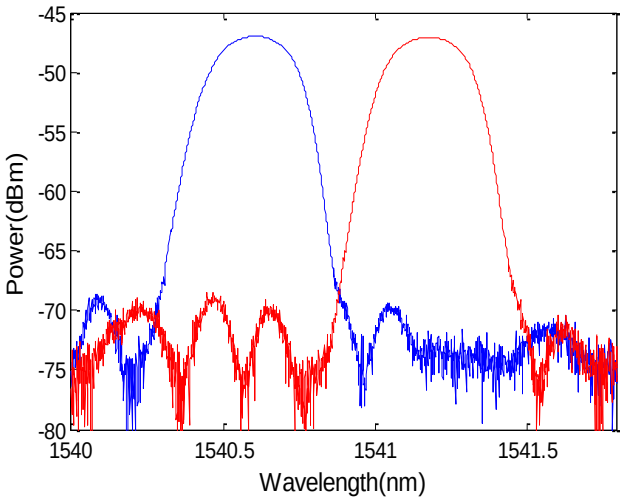

Fig. 2.11. Bragg wavelength shift in the FBG at 1,540.6 nm measured with the OSA. Blue trace: reference position; red trace: FBG heated.

The system's electrical frequency response (2.2) was captured simultaneously and it is shown in Fig. 2.12. The traces show a typical wavy form due to the composition of seven oscillations. Afterwards, the impulse responses were computed before and after heating by use of the IFT once zero-padding the raw traces to one million points. This gives an effective bandwidth $B´$= 625 GHz or a temporal resolution in the impulse response $\Delta t´$= 1.6 ps. From (2.4), and using a typical value of dispersion D = 17 ps/nm·km, the system's wavelength shift resolution in these experiments is around $\Delta\lambda_B$ = 14 pm.

The impulse response, centered at the peak generated by the heated FBG, is shown in Fig. 2.13. The time axis does not correspond to the true delays experienced by the microwave signal in the SMF line since it is aliased due to the large frequency step used in the VNA measurements (Δf =20 GHz / 32,000 = 625 kHz). Since the present method is based on relative time measurements, this fact does not affect its performance.

It can be observed that the impulse response's peaks corresponding to the two situations arrive at different times: the blue trace (not heated) has its maximum at 479.202 ns, whereas the maximum of the red trace (heated) is at 479.267 ns. After (2.4) application, and using a measured dispersion at the Bragg wavelength equal to 16.9036 ps/nm·km (dispersion value for 1,540.6 nm), it is obtained a Bragg wavelength shift of 0.5631 nm. The difference with the OSA measurement is as low as 8.0 pm, under the expected resolution of the present implementation of the method.

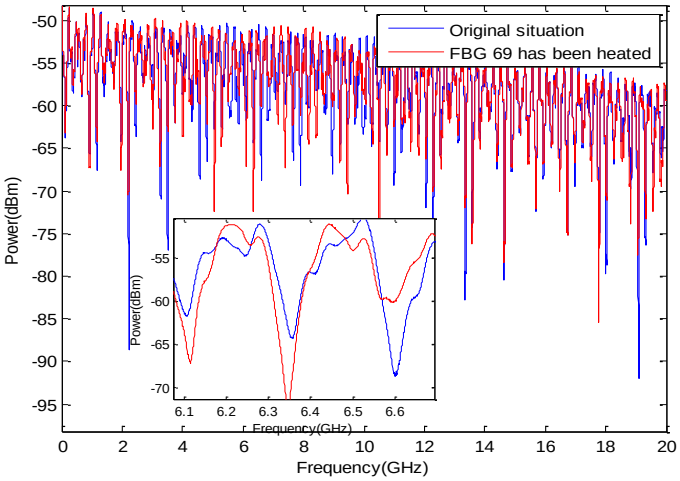

Fig. 2.12. Electrical spectrum in the initial situation (blue trace) and when the FBG 69 (FBG at 1,540.6 nm) is heated (red trace). Inset: Zoom view centered around 6.4 GHz.

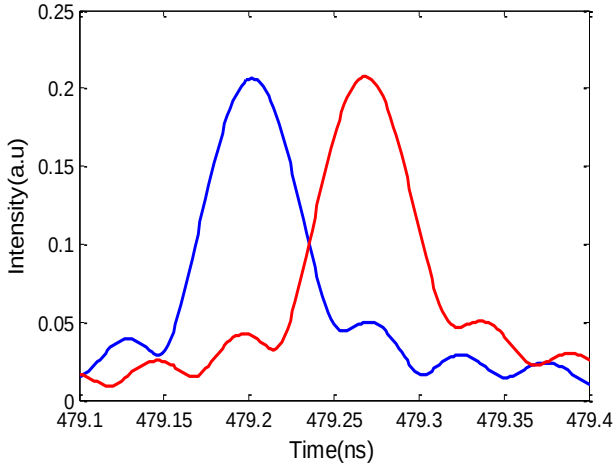

Fig. 2.13. Peak in the system's impulse response generated by the FBG at 1,540.6 nm at the reference position (blue trace) and when it is heated (red trace).

Different FBGs were heated in order to show that neither their shape nor the reflected power have influence in the interrogation method. The results of one of these measurements, performed with the same set of parameters, has been depicted in Fig. 2.14. The measured displacement in Bragg wavelength from the OSA was 0.5021 nm, whereas the outcome of the analysis of the impulse response provides a shift of 0.4972 nm, using D = 16.5067 ps/nm·km at the Bragg wavelength (FBG at 1,531.3 nm). The difference of 4.9 pm is again under the expected resolution.

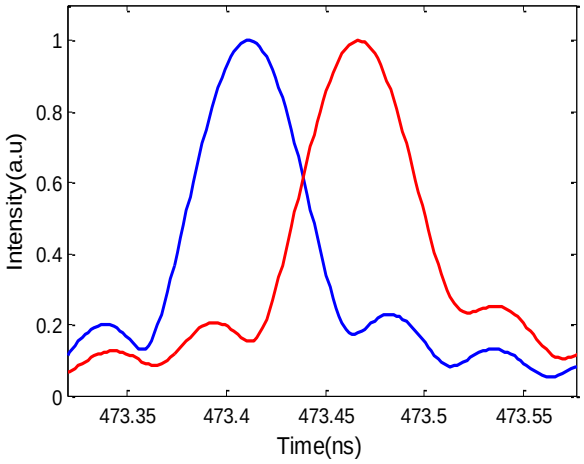

Fig. 2.14. Peaks in the system's impulse response generated by the FBG at 1,531.3 nm at the reference position (blue trace) and when it is heated (red trace).

In addition, as it has been stated previously, zero padding allows for reducing the measurement bandwidth B without degradation in resolution. To show this, the 32,000 points of the raw VNA data for the initial bandwidth B=20 GHz were low-pass filtered to the first 8,000 points lying in the range below 5 GHz. After truncation, zeros were added after the data points before the IFT computation in two different configurations. The resulting string lengths were 100,000 (effective bandwidth B'= 62.5 GHz) and one million (B'= 625 GHz). In the first case, impulse responses from 5-GHz data with lower resolution are obtained ($\Delta t'$ = 16 ps), whereas in the second case it is obtained an equivalent as before ($\Delta t'$=1.6 ps). The four traces are shown in Fig. 2.15.

Comparison of Figs. 2.15 and 2.13 shows that the peak width has been enlarged by a factor of four due to the decrease in measurement bandwidth. Despite this fact, when the 5-GHz VNA data is zero-padded up to one million points, it is obtained the same value of the difference (8 pm) as with the original 32,000 points, 20-GHz trace in Fig. 2.13. This is because the resolution in the peak determination depends on the sampling step $\Delta t'$ and not to the peak's width. On the other hand, the Bragg wavelength shift measured after zero-padding up to

only 100,000 points is 0.5546 nm, which represents a difference of 16.5 pm with the measured trace with the OSA. This increment is due to the tenfold increase in sampling step. It is thus apparent that zero padding is a powerful tool that allows not only for a reduction of the measurement bandwidth, but also for reaching compromises between resolution and processing time through the decrease in the dimensionality of the zero-padded signal.

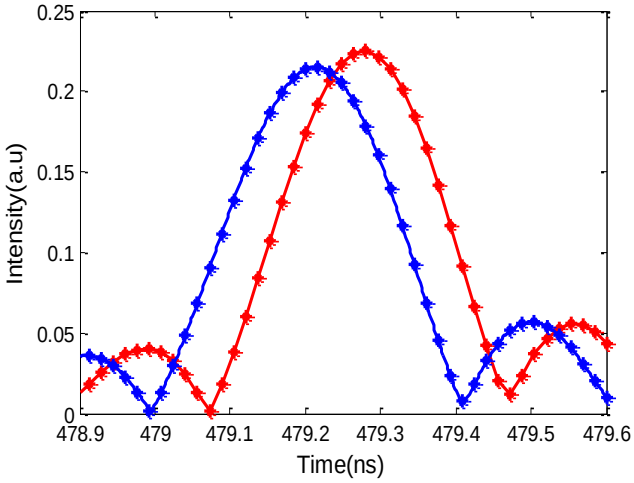

Fig. 2.15. Peaks in the system's impulse response generated by the FBG whose Bragg wavelength is 1,540.6 nm with different impulse response resolution or temporal separation (crosses = 16 ps, dots = 1.6 ps) when the FBG is at the reference temperature (blue) and after heating (red). The high-resolution traces in dots are depicted as continuous curves. The IFT is computed by zero-padding the frequency response to one million points (dots) or 100,000 points (crosses).

Finally, it is worth studying the stability of the samples of the FBGs that are not heated. In Fig. 2.16. it is shown the sample of one FBG in the initial situation and when a different FBG is heated for different bandwidths (5, 10 and 20 GHz). As can be seen the different samples have the same center but different amplitude. The difference in amplitude is caused by source drifting, but it is not important since the Bragg wavelength is extracted from the temporal position of the FBG created sample, independently of the amplitude of the sample.

2.6 Conclusions

In this chapter, has been shown the wavelength to radio-frequency delay mapping interrogation method of FBGs in cascade for its use as quasi-distributed temperature/strain sensors. The principle is based on the usage of Microwave Photonics techniques to map wavelength shifts into group delay shifts in the impulse response of a fiber optics link. The measurement is performed in the frequency domain by a VNA, and then the response translated to the time domain by numerical computation of the IFT. The scale for

wavelength to delay conversion is determined by the total link's dispersion. Thetechnique has been experimentally investigated in a cascade of seven FBGs with unequal reflected power and Bragg wavelength separation.

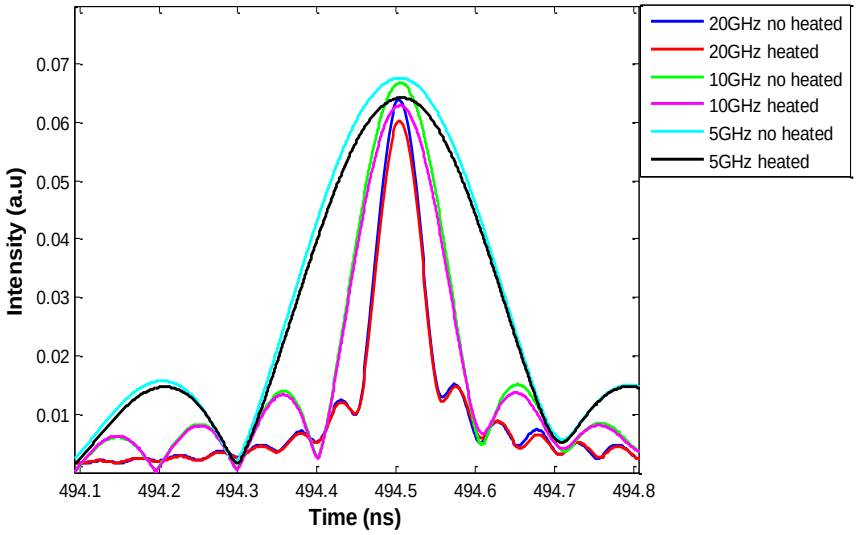

Fig. 2.16. FBG sample for different bandwidths of the electrical measurement (5, 10 and 20 GHz) when a different FBG is in the initial situation and when it is heated.

The resolution in the measurement of the Bragg wavelength is around 14 pm, and is determined by the total dispersion used, the zero padding length of the raw VNA data, and its RF bandwidth. In principle, this resolution could be improved by enlarging the zero padding length up to a certain limit without requiring corrections of the linear relationship (2.4) (limit of 4 pm for a 1 nm of Bragg wavelength shift as stated in Section 2.4). Below this limit, an increase of resolution, a larger Bragg wavelength shift or both would require to take into account higher-order dispersion corrections to (2.4), and evaluate limitations due to overlapping of the impulse response peaks in (2.3). Besides, it has been shown that, for a given resolution, the total RF measurement bandwidth required to implement the technique is scalable. Despite the increase in the peak's width, feasible wavelength shifts have been measured when the RF bandwidth is reduced from 20 to 5 GHz, thus avoiding the use of broadband microwave components. The method also shows an additional compromise between IFT processing time and resolution, through the length of the zero-padded signals. Finally, for a given processing effort, i.e., for a given temporal resolution in the impulse response $\Delta t'$, the resolution can also be improved simply by enlarging the total dispersion in (2.4).

Although the cost of the equipment used, mainly the VNA, is important, its operational bandwidth could be reduced (for 20 to 5 GHz), or it could even be

directly replaced by a tunable electrical oscillator and a dedicated digital signal processor to perform the same kind of measurements. Besides the flexibility, as exemplified in the above tradeoffs, the advantage over conventional approaches is that the proposed scheme does not require a tunable laser. To conclude, the same principle of operation can be used with cascaded FBG sensors where the gratings have the same Bragg wavelength and/or with a constant spectral separation between adjacent gratings.

References

[1] K. O. Hill and G. Meltz, "Fiber Bragg grating technology fundamentals and overview," in *Journal of Lightwave Technology*, vol. 15, no. 8, pp. 1263-1276, Aug 1997.

[2] A. D. Kersey *et al*., "Fiber grating sensors," in *Journal of Lightwave Technology*, vol. 15, no. 8, pp. 1442-1463, Aug 1997.

[3] Yiping Wang, Yiping Cui and Binfeng Yun, "A fiber Bragg grating sensor system for simultaneously static and dynamic measurements with a wavelength-swept fiber laser," in *IEEE Photonics Technology Letters*, vol. 18, no. 14, pp. 1539-1541, July 2006.

[4] H. Y. Fu, H. L. Liu, W. H. Chung and H. Y. Tam, "A Novel Fiber Bragg Grating Sensor Configuration for Long-Distance Quasi-Distributed Measurement," in *IEEE Sensors Journal*, vol. 8, no. 9, pp. 1598-1602, Sept. 2008.

[5] M. Buric, K. P. Chen, M. Bhattarai, P. R. Swinehart and M. Maklad, "Active Fiber Bragg Grating Hydrogen Sensors for All-Temperature Operation," in *IEEE Photonics Technology Letters*, vol. 19, no. 5, pp. 255-257, March1, 2007.

[6] D. C. Betz, G. Thursby, B. Culshaw and W. J. Staszewski, "Advanced layout of a fiber Bragg grating strain gauge rosette," in *Journal of Lightwave Technology*, vol. 24, no. 2, pp. 1019-1026, Feb. 2006.

[7] H. Zhang, F. Deng, Q. Wang, L. Yan, Y. Dai and K. Kim, "Development of Strain Measurement in Superconducting Magnet Through Fiber Bragg Grating," in *IEEE Transactions on Applied Superconductivity*, vol. 18, no. 2, pp. 1419-1422, June 2008.

[8] M. Zaynetdinov, E. M. See, B. Geist, G. Ciovati, H. D. Robinson and V. Kochergin, "A Fiber Bragg Grating Temperature Sensor for 2–400 K," in *IEEE Sensors Journal*, vol. 15, no. 3, pp. 1908-1912, March 2015.

[9] B. Zhang and M. Kahrizi, "High-Temperature Resistance Fiber Bragg Grating Temperature Sensor Fabrication," in *IEEE Sensors Journal*, vol. 7, no. 4, pp. 586-591, April 2007.

[10] Eric Udd; William B. Spillman, "Distributed and Multiplexed Fiber Optic Sensors," in *Fiber Optic Sensors:An Introduction for Engineers and Scientists* , 1, Wiley Telecom, 2011, pp. 512.

[11] Q. Sun, D. Liu, L. Xia, J. Wang, H. Liu and P. Shum, "Experimental Demonstration of Multipoint Temperature Warning Sensor Using a Multichannel Matched Fiber Bragg Grating," in *IEEE Photonics Technology Letters*, vol. 20, no. 11, pp. 933-935, June1, 2008.

[12] K. Kajiwara and K. Hotate, "Multiplexing of Long-Length Fiber Bragg Grating Distributed Sensors Based on Synthesis of Optical Coherence Function," in *IEEE Photonics Technology Letters*, vol. 23, no. 21, pp. 1555-1557, Nov.1, 2011.

[13] C. Hu, H. Wen and W. Bai, "A Novel Interrogation System for Large Scale Sensing Network With Identical Ultra-Weak Fiber Bragg Gratings," in *Journal of Lightwave Technology*, vol. 32, no. 7, pp. 1406-1411, April1, 2014.

[14] Y. Koyamada, Y. Sakairi, N. Takeuchi and S. Adachi, "Novel Technique to Improve Spatial Resolution in Brillouin Optical Time-Domain Reflectometry," in *IEEE Photonics Technology Letters*, vol. 19, no. 23, pp. 1910-1912, Dec.1, 2007.

[15] J. Song, W. Li, P. Lu, Y. Xu, L. Chen and X. Bao, "Long-Range High Spatial Resolution Distributed Temperature and Strain Sensing Based on Optical Frequency-Domain Reflectometry," in *IEEE Photonics Journal*, vol. 6, no. 3, pp. 1-8, June 2014.

[16] http://lunainc.com/

[17] J. Yao, "Microwave Photonics," in *Journal of Lightwave Technology*, vol. 27, no. 3, pp. 314-335, Feb.1, 2009.

[18] A. J. Seeds, "Microwave photonics," in *IEEE Transactions on Microwave Theory and Techniques*, vol. 50, no. 3, pp. 877-887, Mar 2002.

[19] A. J. Seeds and K. J. Williams, "Microwave Photonics," in *Journal of Lightwave Technology*, vol. 24, no. 12, pp. 4628-4641, Dec. 2006.

[20] J. Hervás *et al*., "Microwave Photonics for Optical Sensors," in *IEEE Journal of Selected Topics in Quantum Electronics*, vol. 23, no. 2, pp. 327-339, March-April 2017.

[21] Clement, Juan & Hervás, Javier & Fernandez-Pousa, Carlos & Barrera, David & Pastor, D & Sales, Salvador & Capmany, J. (2015). Interrogation of a cascaded FBG sensor using a wavelength-to-delay mapping technique. 96344S-96344S. 10.1117/12.2194977.

[22] J. Hervás, C. R. Fernández-Pousa, D. Barrera, D. Pastor, S. Sales and J. Capmany, "An Interrogation Technique of FBG Cascade Sensors Using Wavelength to Radio-Frequency Delay Mapping," in *Journal of Lightwave Technology*, vol. 33, no. 11, pp. 2222-2227, June1, 1 2015.

[23] T. Komukai and M. Nakazawa, "Fabrication of high-quality long-fiber Bragg grating by monitoring 3.1-eV radiation (400 nm) from GeO defects," in *IEEE Photonics Technology Letters*, vol. 8, no. 11, pp. 1495-1497, Nov. 1996.

[24] J. Herrera, F. Ramos and J. Marti, "Compensation for dispersion-induced carrier suppression effect in microwave/millimetre-wave optical links using optical phase conjugation in semiconductor optical amplifiers," in *Electronics Letters*, vol. 42, no. 4, pp. 238-239, 16 Feb. 2006.

[25] A. Ricchiuti, D. Barrera, S. Sales, L. Thevenaz, and J. Capmany, "Long fiber Bragg grating sensor interrogation using discrete-time microwave photonic filtering techniques," Opt. Express 21, 28175-28181 (2013).

[26] J. Proakis and D. Manolakis, *Digital Signal Processing*, 4th. ed. Prentice-Hall, Upper Saddle River, NJ, 2006.

Chapter 3

The KLT based interrogation technique

3.1 Introduction

Two of the most important parameters that are being attempted to improve over the traditional interrogation techniques are the interrogation speed [1-2] and the resolution [3-4]. OFDR [5-6] techniques need to make a whole sweep of the tunable laser bandwidth in order to guarantee both small time and spatial resolutions. This leads to a measuring time of at least several seconds. OTDR [7-8] techniques show measurement times ranging from slightly below a second to several minutes. BOTDA [9-10] and BOTDR [11-12] techniques show sweep times shorter than one second, but the necessity to perform hundreds or even thousands of measurements in order to improve the SNR of the extracted signal makes the measuring time to range from several seconds to several minutes, depending on the desired accuracy and resolution.

Microwave Photonics [13-15] techniques are not immune to this. For example, the technique showed in the previous chapter [16] shows a measuring time of several seconds. It can be shorten using more dedicated hardware (to the scale of milliseconds). But there is also a computational time that is quite long taking into account that the inverse Fourier transform is performed over one million point traces and that, afterwards, maxima search must be performed to locate the FBGs generated samples in time, in order to measure the centre of the sinc shaped sample to calculate the Bragg wavelength change.

In this chapter, the wavelength to delay mapping interrogation technique [16] is used to retrieve the sensing information of a fiber array but this time the Karhunen-Loeve transform is used to increase the resolution of the Bragg wavelength determination from the RF impulse response without the use of the computationally costly zero-padding procedure. This way, the IFFT number of points is reduced in three orders of magnitude, reducing the computational effort and the measurement time.

3.2 The KLT transform

The Karhunen-Loève Transform (KLT) [17-19] is a representation of a stochastic process as a series of orthogonal functions. It is also called the Eigenvector Transform.

Compared to a Fourier series [20-22] in which the coefficients are fixed numbers and the expansion is based on sinusoidal functions, the coefficients in

the Karhunen–Loève Transform are random variables and the expansion basis is dependent on the process. In fact, the orthogonal basis functions used in this

representation are determined by the covariance function of the process. Therefore, the Karhunen–Loève Transform adapts itself to the process in order to produce the best possible basis for its expansion.

Imagine a 3D object, for example a smartphone, and a three axis orthogonal reference framework oriented arbitrarily with respect to the object. Taking into account classical Newtonian mechanics, the properties of the smartphone are describe by a 3x3 matrix, known as the Inertia Matrix. The elements of this matrix are normally different from zero. It is easy to understand that a matrix with all components being non-zero is harder to handle compared to a diagonal matrix (a matrix in which all components are zero except for those in the diagonal). So, it would be perfect to find a transformation or a set of axis that leads to an inertia matrix which is a diagonal matrix. There is only a set of axis that yields a diagonal inertia matrix: these three axis must coincide with the so called "principal axis" or "eigenvectors" of the smartphone. And this transformation can be found with the procedure of finding the eigenvectors of a square matrix. In a similar way, any stochastic process can be described using the autocorrelation. This autocorrelation is the conversion of the inertia matrix. Therefore, if the eigenvectors of the autocorrelation are found, the simplest description of the stochastic process is achieved.

Furthermore, if noise is added to a deterministic signal, what is called "noisy signal" is obtained. The signal+noise is a random function dependent on time. Assuming that the autocorrelation of this signal+noise is known, the orthonormal functions are just the eigenvectors of the correlation. These eigenvectors are the best basis to represent this signal+noise, far better than any Fourier transformation [23].

The conclusion is that the KLT adapts itself to fit the signal+noise and this adaptability is the main advantage over other type of transformations.

3.3 The KLT routine

The KLT routine [24] is the routine that is applied to the impulse response retrieved through inverse fast Fourier transformation (IFFT) of the electrical response raw data in order to extract the sensing data of the samples generated by each one of the FBGs.

In the previous chapter, in order to improve the resolution, the zero-padding technique was used. It consisted in filling with zeroes the electrical response raw data in order to shorten the temporal separation between consecutive points in the impulse response. But this brings a problem with regards to computational effort. In order to have a resolution close to 1 ºC in terms of temperature (10 pm in terms of Bragg wavelength movement) the number of points prior to IFFT calculation must be enlarged up to one million points, adding zeroes to the raw data prior to IFFT calculation.

The KLT routine is used to retrieve the information of the impulse response but with no zero padding. That means that we can no longer find a clear sinc-shaped sample in the impulse response. Instead, what it can be found in the impulse response is what it is showed in Fig. 3.1. As can be seen, the Bragg wavelength of the FBG changes by 0.1nm but the maximum of the FBG sample is at the same position, being impossible to address the question of how much the Bragg wavelength has changed. Furthermore, the center of the sinc shaped sample can be no longer determined since there is no longer such sinc-shaped sample, visually speaking of course. However, a center estimation could be carried out in order to estimate the center of the sinc-shaped sample. The problem is that, with the number of points that belong to the main lobule, the resolution would be dozens of pm, which is not very good. Here is where the KLT is applied in order to extract the information of this impulse response with a resolution smaller than the one achieved using centroid estimation and much smaller compared to the resolution given by the distance between consecutive points in the impulse response.

As it has been explained in the previous section of this chapter, what we have in the impulse response is signal affected by noise, and the work of the KLT is to find the eigenvectors (and also the eigenvalues) that best fit this signal+noise and therefore the best and simplest way to represent this signal+noise would be obtained. After doing that, the temperature/Bragg wavelength experienced by the FBG can be retrieved easily studying the eigenvalues.

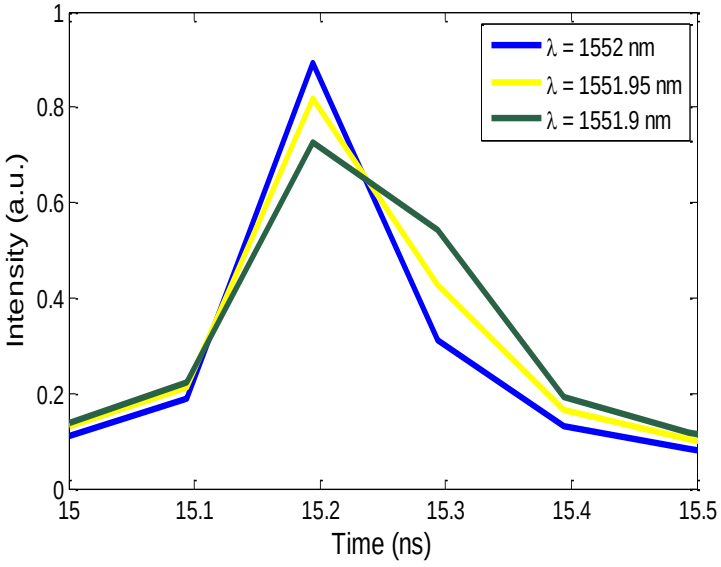

Fig. 3.1. (Simulation) FBG created sample in the impulse response for different Bragg wavelengths and after undergoing dispersion.

The complete measurement routine follows this procedure:

1) The Vector Network Analyzer performs a sweep from 0 to 2.5 GHz with 2,501 points. This means an almost tenfold reduction in the frequency bandwidth and an even larger decrease in the number of points of the measurement compared to the wavelength to radio-frequency delay mapping technique.

2) The IFFT is applied to the raw VNA data. This means a 400-fold reduction in the number of points in which the IFFT is computed.

3) Determination of the FBGs samples position inside the impulse response amplitude vector. This can be done with a maxima search through the impulse response data vector and setting some constraints and conditions.

4) Select the four points that best represent the FBG sample.

5) The KLT routine is applied following Maccone's approximation [23-24]. It starts with the calculation of the fast Fourier transformation (FFT) of the four points that represent the FBG sample, which is presented as a vector $\mathbf{G}=[G(f_1)\ G(f_2)\ G(f_3)\ G(f_4)]$.

6) Then, these 4 components of the vector are rearranged in order to construct a Toeplitz matrix $\mathbf{M}=(M_{ij})$. A Toeplitz matrix is a square matrix in which diagonals are constant from left to right. In this case it is a 4x4 matrix in which the components of the matrix are $M_{ij}=G(f_{|i-j|+1})$.

7) The kernel of the routine is applied to the matrix **M**. It is based on the determination of an orthonormal basis **V** of the matrix **M** which can be calculated easily performing the singular value decomposition (SVD) to the matrix **M**:

$$M= V\ D\ V^{-1} \tag{3.1}$$

where **D** is a matrix that contains in its diagonal the four eigenvalues of **M**. The amplitude of the highest-rank eigenvalue of this set, records the amplitude change of the *sinc* peak allowing measuring the wavelength change continuously.

A simulation set was used in order to prove the interrogation technique using the KLT routine. A Microwave Photonics filter with four taps (four FBGs) was simulated. The dispersive media simulated was a chirped FBG with a dispersion slope of -170 ps/nm. The four FBGs were equally spaced between 1,550 and

1,553 nm (1nm difference between consecutive FBGs) and had a 1 m spatial separation among them. The electrical spectrum of such a filter was simulated in a 10 GHz bandwidth and with 2,501 points, which led to a $\Delta t = 0.1$ ns in the impulse response retrieved after IFFT calculation. The Bragg wavelength of the third FBG was continuously shifted from 1,552 to 1,556 nm in 10 pm steps and the impulse response of the filter was calculated for each one of the different situations. Finally, the KLT routine is applied to the 4 points that best represent the FBG that is experiencing Bragg wavelength changes and the eigenvalues are extracted. It can be seen in Fig. 3.2 that the greater eigenvalue $\xi \equiv \xi_1$ follows the movement of the FBG, but in a periodical way. The period is around 600 pm of Bragg wavelength change, so that the ξ value cannot track the Bragg wavelength beyond this period and an initial coarse determination of the Bragg wavelength must be performed. This could be achieved easily with a centroid estimation in order to locate the eigenvalue in the correct period, followed by the fine calculation of the Bragg wavelength change using the more accurate KLT routine, as schematically shown in Fig. 3.3.

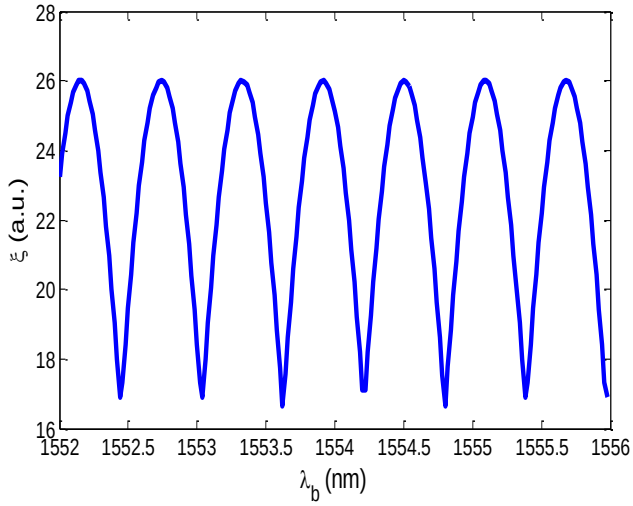

Fig. 3.2. Highest eigenvalue calculated in the simulation test for different Bragg wavelengths.

This eigenvalue period is related to the RF measurement bandwidth in the capture of the electrical frequency response and the wavelength to time delay mapping scale. As mentioned before, the temporal interval between consecutive points in the impulse response, Δt, is 0.1 ns for the bandwidth B of 10 GHz employed in our simulations. The chirped FBG provides a dispersion of D=-170 ps/nm, so the result in terms of Bragg wavelength change ($\Delta\lambda=\Delta t/D$) is 588 pm. This means that the KLT can follow a variation of around 60 ºC within a single period, assuming a standard temperature coefficient of an FBG with Bragg wavelength around 1,550 nm of $\delta\lambda_B/\delta T \approx 10$ pm/ºC. The eigenvalue period can

be increased either by decreasing the RF measurement bandwidth, *B*, or the value of dispersion, *D*.

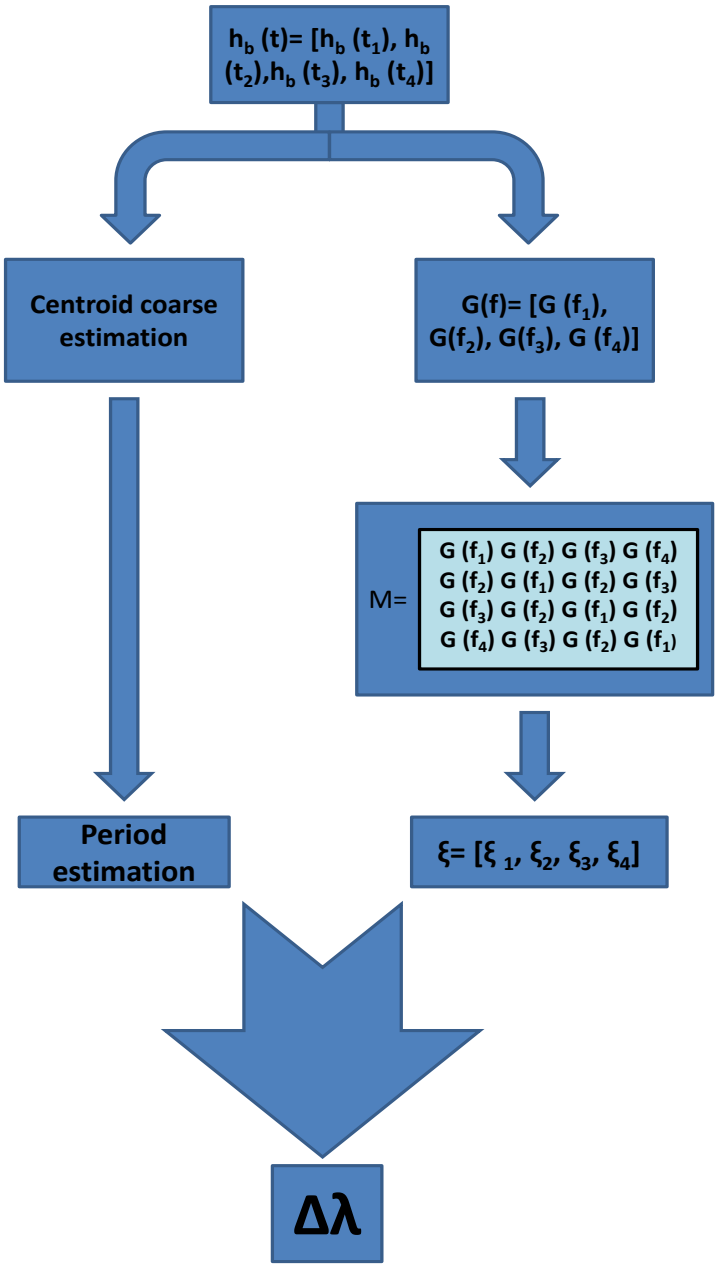

Fig.3.3. Flowchart of the KLT routine

3.4 Dispersive media

Dispersion is what causes the FBG created sample movement in time in the impulse response when the FBG is under a temperature or strain change. In the previous chapter this role was carried out by 6.8 km of standard single mode fibre.

The problem whit this dispersive media is the non-linearity of the dispersion in the working window. In the previous technique, in which the centre of the sinc-shaped sample was assessed thanks to the usage of the zero-padding technique, which increased the measurement resolution, to have a non-linear dispersion has no effect as long as this non-linearity has been measured and it is taken into account to calculate the Bragg wavelength drift.

Nevertheless, when the KLT routine is applied and no zero-padding is used, there is neither a centre measurement nor a Bragg wavelength conversion from the sample delay. On the contrary, there is a translation between the behaviour of the biggest eigenvalue calculated and its relation to the Bragg wavelength of the FBG.

Having a non-linear dispersion means that the behaviour of the greater eigenvalue is no longer periodical and it can affect the accuracy of the interrogation technique. This is the main reason why in this interrogation technique the dispersive media is changed from the fiber coil to a long chirped FBG with a dispersion slope of -170 ps/nm. In Fig. 3.4 it can be seen the dispersion for each of the wavelengths. As can be seen the dispersion is completely linear in the entire bandwidth (1,540 to 1,560 nm). The chirped FBG is physically encapsulated to make it temperature and strain action-free. Losses and the physical space used are also smaller compared to the fiber spool alternative. The only inconvenient is the working wavelength range, which is in this case 20 nm compared to the full band of the standard telecom fiber.

An important aspect to take into account is the carrier suppression effect present in analogue links. This effect has been simulated for this fiber and in Fig. 3.5 it is shown the carrier suppression effect from 0 to 20 GHz. It can be observed that there is no effect in the working bandwidth (0-2.5 GHz) of the technique. As it has been stated in the first technique chapter, the carrier suppression effect is like a low-pass filtering effect which causes a broadening of the temporal sample retrieved in the impulse response. This does not change the position of the sinc-shaped sample but it can affect the amplitude of that sample, affecting the eigenvalue used by the KLT routine to assess the Bragg wavelength change experienced by the FBG.

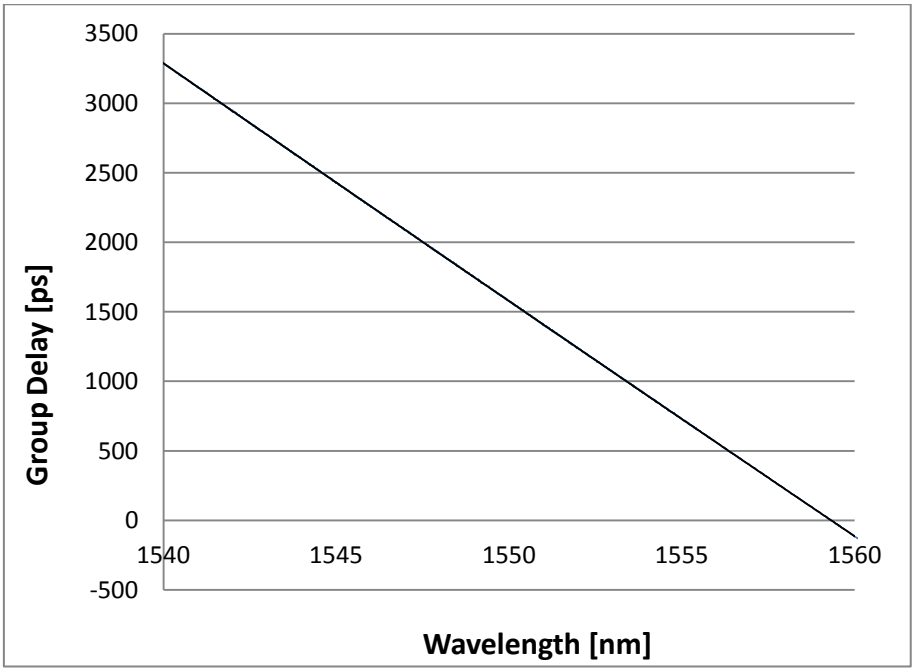

Fig. 3.4. Dispersion values of the chirped FBG

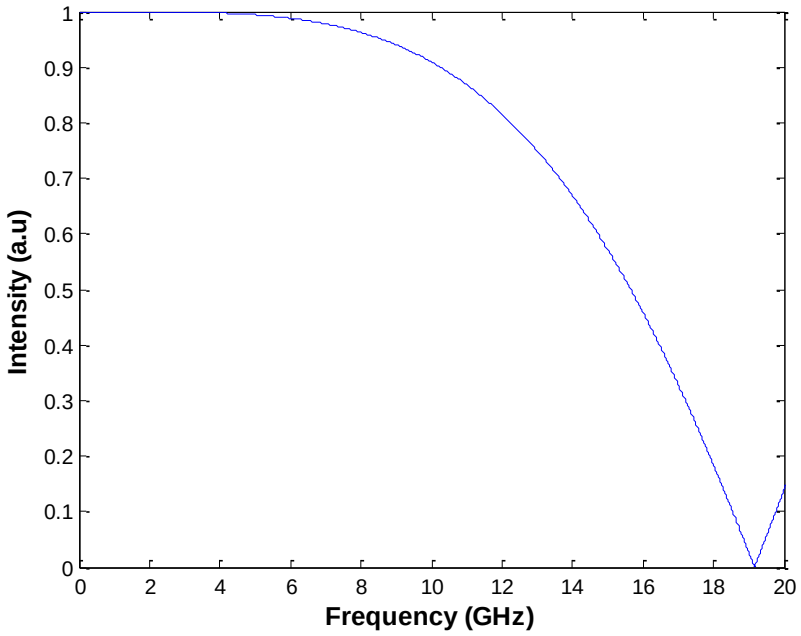

Fig. 3.5. Carrier suppression effect due to the chirped FBG from 0 to 20 GHz.

3.5 Noise effect

The KLT performance is based in the extraction of the eigenvalues of the Toeplitz matrix constructed with the amplitude values retrieved in the impulse response. These amplitude values in the impulse response are affected by the noise of the electrical spectrum measurement, therefore noise can affect the interrogation technique performance.

In order to assess the noise impact, a set of measurements was carried out. The signal to noise ratio (SNR) of the impulse response is directly related to the SNR of the electrical spectrum measurement performed by the VNA. In this case and for a given modulating and working power, the SNR comes mainly from the intermediate frequency (IF) filter used to perform the measurement. The IF filter sets the bandwidth in which the VNA is going to integrate the received power to retrieve the final value at that discrete frequency. To have a wider filter means a greater noise power due to a larger integration bandwidth, but also a faster measurement.

The setup used to perform the measurements is depicted in Fig. 3.6.

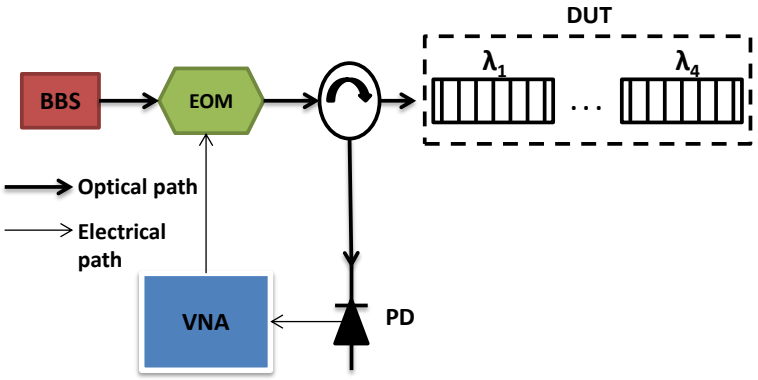

Fig.3.6. Setup used to assess the noise impact

It consists of a broadband source, a modulator in which light is modulated by the microwave signals coming from the VNA, a circulator, a 4 FBGs array and a photodetector. The idea was to measure the electrical spectrum of the microwave photonics filter using different IF bandwidths and to retrieve the impulse response of these, in order to observe the impact of noise in the FBGs generated samples.

As can be seen in Fig. 3.7 the noise floor grows linearly with the IF bandwidth. This noise floor has been measured with no DUT, it is to say, with a direct connection between modulator and photodetector and no electrical signal driving the modulator. For an IF bandwidth of 100 Hz the noise floor is around

-85 dBm, for 1 KHz it is around -75 dBm, for 3 KHz it is close to -70 dBm and for 10 KHz it is around -65 dBm.

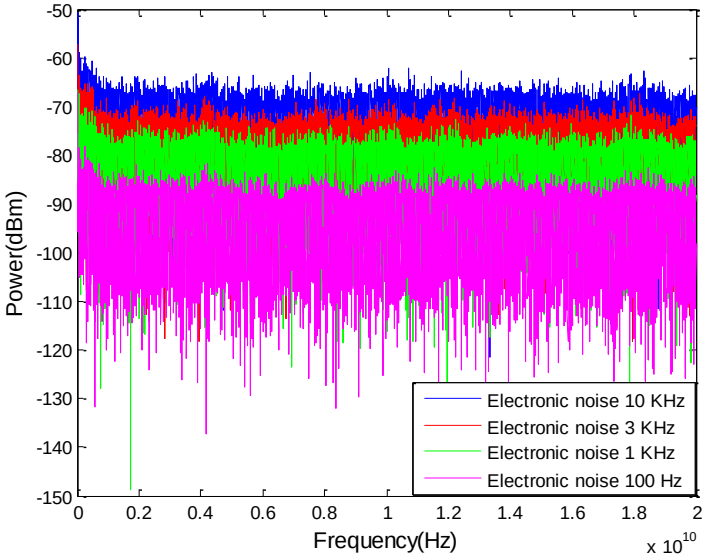

Fig. 3.7. Noise floor for different IF bandwidths (100 Hz and 1,3 and 10 KHz)

But, as it has been stated before, the IF bandwidth also affects the measurement time. In table 3.1 it can be found the measurement time for different IF bandwidths (electrical bandwidth-20GHz, number of points-32,001).

IF Bandwidth	Measurement time
1 KHz	29.000 s
10 KHz	3.862 s
100 KHz	340.800 ms
200 KHz	151.467 ms
360 KHz	75.733 ms
1 MHz	22.933 ms

Table 3.1. Measurement times for different IF bandwidths

The measurements carried out with the setup showed in Fig. 3.6 are depicted in Fig. 3.8. These measurements were carried out in a 20 GHz bandwidth, with 32,001 points and a modulation electrical power of 0 dBm. In Fig. 3.8 it is shown a zoom view centred at 6.75 GHz for different IF bandwidths.

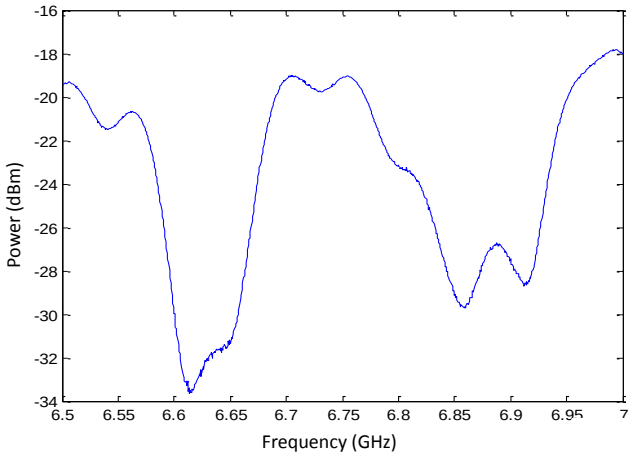
Power (dBm)
-16
-18
-20
-22
-24
-26
-28
-30
-32
-34
6.5
6.55
6.6
6.65
6.7
6.75
6.8
6.85
6.9
6.95
7
Frequency (GHz)

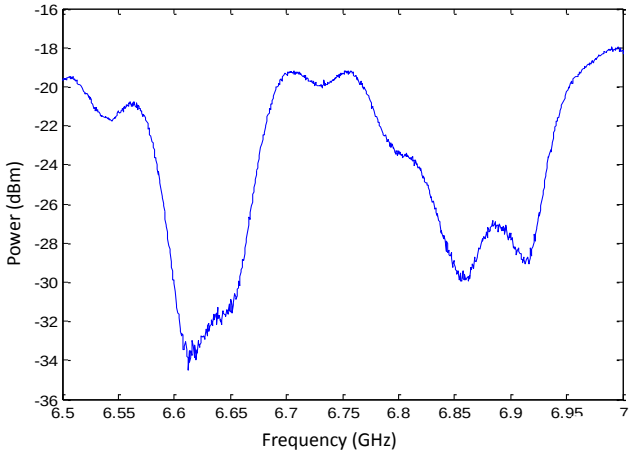
Power (dBm)
-16
-18
-20
-22
-24
-26
-28
-30
-32
-34
-36
6.5
6.55
6.6
6.65
6.7
6.75
6.8
6.85
6.9
6.95
7
Frequency (GHz)

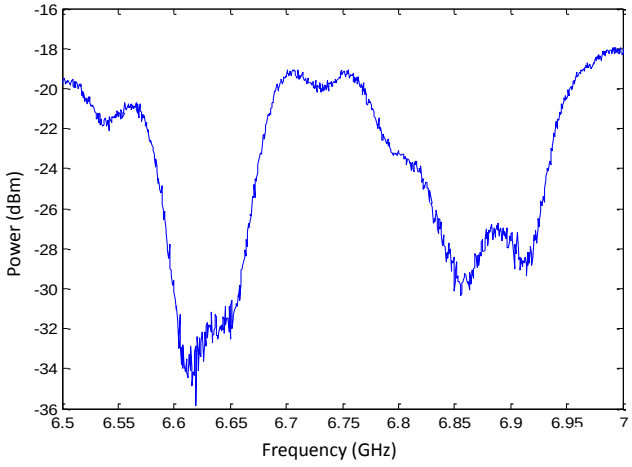
Power (dBm)
-16
-18
-20
-22
-24
-26
-28
-30
-32
-34
-36
6.5
6.55
6.6
6.65
6.7
6.75
6.8
6.85
6.9
6.95
7
Frequency (GHz)

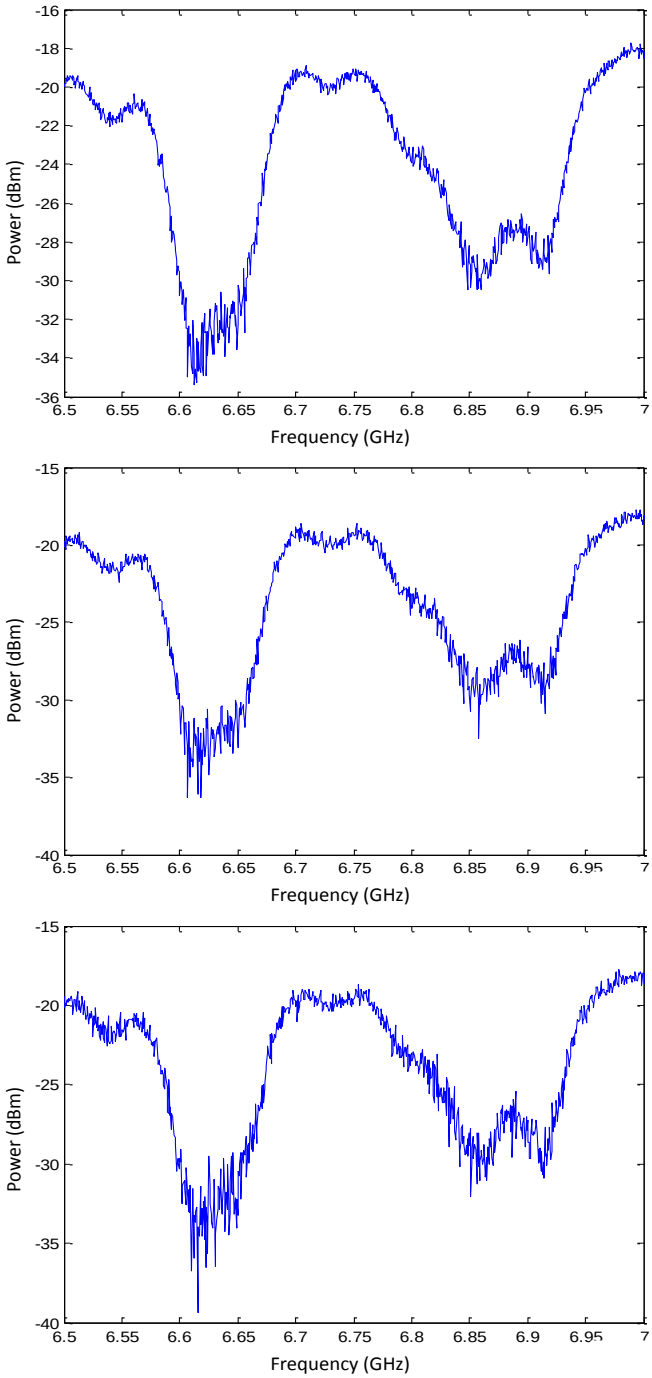

Fig. 3.8. Electrical response centred at 6.75 GHz for different IF bandwidths (1, 10, 50, 100, 200 and 360 KHz)

As can be seen in Fig. 3.8 the trace is more and more affected by noise when the IF bandwidth becomes higher, but even with a 360 KHz bandwidth the signal envelope can be still observed.

In order to assess how this noise affects the samples in the impulse response, the inverse fast Fourier transformation of the electrical responses showed above was calculated. In Fig. 3.9 are shown two different samples of two different FBGs.

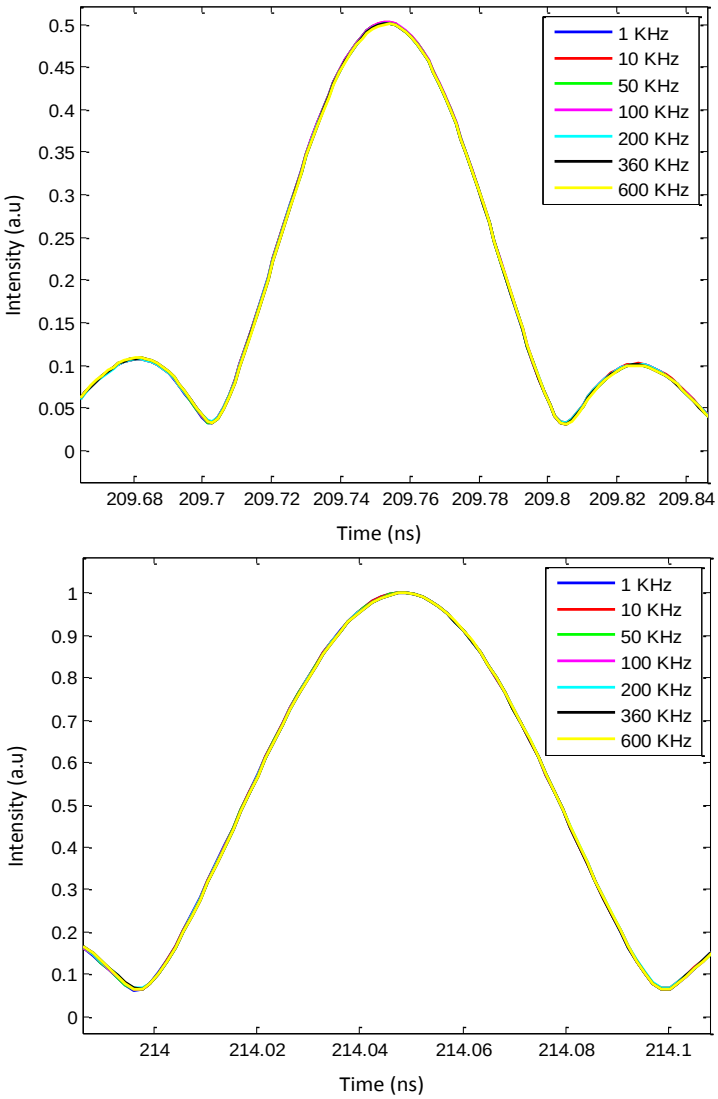

Fig. 3.9. FBGs created samples for different IF bandwidths

As can be seen in Fig. 3.9 the created samples are identical for different IF bandwidths, even for 600 KHz. Therefore, the calculated impulse response is quite robust against low SNR scenarios and high IF bandwidths can be used with the KLT interrogation technique to make it even faster.

3.6 Experimental measurements

The setup shown in Fig. 3.10 was mounted in the lab in a room in order to experimentally demonstrate that the KLT routine is able to measure temperature changes below the actual resolution of the measurement, given by the temporal distance between consecutive points.

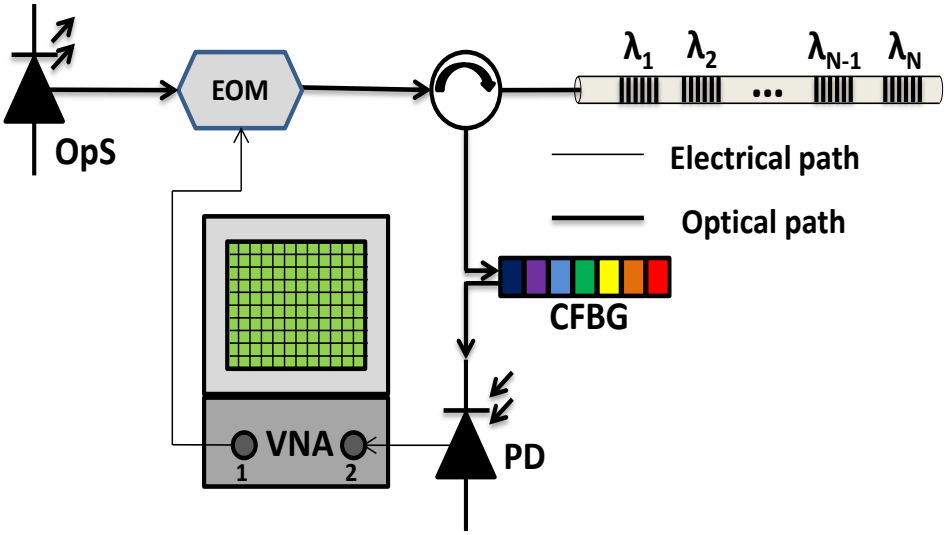

Fig. 3.10. Setup used to perform the experimental measurements (OpS: Optical source, EOM: Electro-optic modulator, CFBG: Chirped FBG, PD: photodetector, VNA: Vector network analyzer)

The only difference between this setup and the one depicted in Fig. 3.6 is the usage of the chirped FBG (CFBG) as a dispersive media in order to introduce dispersion, that as it has been explained before, is what causes a temporal drift in the temporal samples created by each one of the FBGs, which are retrieved in the impulse response after calculation of the IFFT, when they experience a Bragg wavelength change.

The KLT performance is based on the extraction of the eigenvalues of the Toeplitz matrix created after fast Fourier transformation of the amplitude of the impulse response amplitude values. Therefore, additionally to noise (which has been explained in the previous section), a drift in the optical power feeding the system or a drift in the modulation point (initially set to the Q point) can lead to changes in the amplitude values retrieved by the impulse response.

Regarding the optical power, the broadband source role was played by a C&L band amplified spontaneous emission (ASE) source from NP Photonics, which has a 0.01 dB power variation when the temperature is constant. In terms of modulation point drifting, the modulator used in the experiment shows a steady operation in the CW regime.

Nonetheless, if these parameters are not controlled, the system can show wavelength reading errors. But there is an easy way to overcome them. It consists in the use of a reference reflector. This reflector should be free of strain and temperature effects in order not to suffer wavelength changes and to be able to show only the amplitude changes due to power drifting in the source or a Q point drift in the modulator or any other possible effect (like curvature losses). The easiest way to compensate this power changes is just to normalize all the impulse response amplitude values using this reference FBG amplitude value.

An array of four FBGs was fabricated for these experimental measurements. The reflection spectrum of these FBGs is shown in Fig. 3.11.

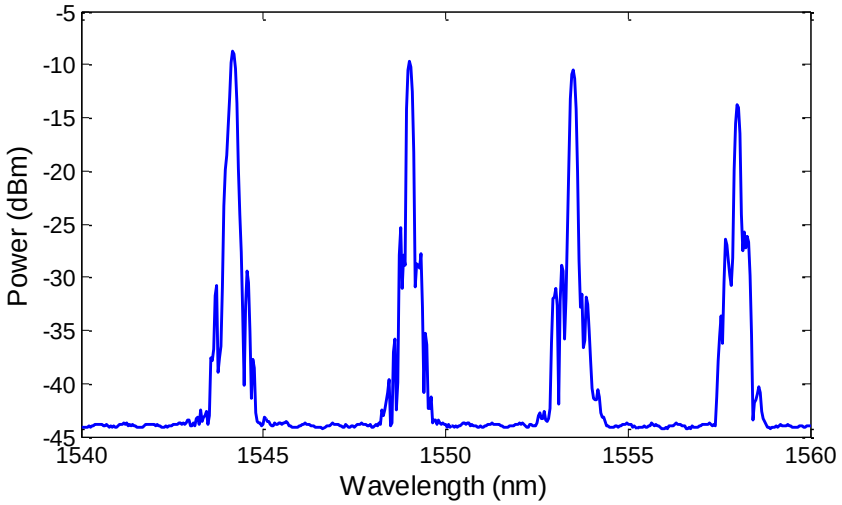

Fig. 3.11. Reflection spectrum of the FBGs array used to perform the experimental measurements.

As can be seen in the previous figure, the FBGs are equally spaced and they have been inscribed inside the CFBG bandwidth (from 1,540 to 1,560 nm). The CFBG showed a dispersion slope of -170 ps/nm with a variation under 3 ps.

In order to perform the measurements, the last one of the FBGs (the 1,558 nm FBG) was fixed inside a climatic chamber in order to produce a temperature ramp to assess if the KLT routine is able to measure temperature changes far

below the resolution of the electrical measurement with no zero padding. The measurement procedure was as follows:

1) The first step was to fix the FBG inside the climatic chamber being careful not to produce any strain effect and switch on the climatic chamber and set its objective temperature to -20 ºC.

2) Once the climatic chamber has reached the -20 ºC objective temperature it is important to keep the temperature at that level for some time in order to homogenize the temperature inside the climatic chamber and to avoid the appearance of temperature gradients that could lead to measurement errors.

3) After the climatic chamber has been at -20 ºC for some time the climatic chamber is switched off in order to avoid vibration problems during the measurement and keep it in that way for 20 minutes in order to homogenize the temperature inside the chamber and avoid again temperature gradient and air currents.

4) Once the temperature is constant inside the climatic chamber the measurement set starts.

5) The electrical response of the system is recorded thanks to the VNA when the temperature experiences an increment of 0.5 ºC. The increment of the temperature is really slow and it is produced by the temperature difference between the room and the climatic chamber. This makes the temperature change really smooth avoiding temperature gradients and air currents inside the chamber, phenomena that could affect the behavior during the measurement set.

6) The last step is the calculation of the IFT of each one of the electrical responses in order to retrieve the system impulse response and the implementation of the KLT routine for the measurement of the temperature variation following the amplitude change of the FBG sample.

The electrical frequency response was recorded with a frequency span from 0-2.5 GHz. This means that the temporal distance between consecutive points in the impulse response is 0.4 ns. Taking into account this, the resolution of the measurement, in terms of wavelength, should be ($\Delta\lambda=\Delta\tau/D$) around 2.353 nm. Therefore, if no zero padding is used and the KLT routine is not performed, only a wavelength change of that scale can produce a measurable change. If the KLT routine is applied, the real resolution is going to be much smaller and it can be affirmed that the KLT eigenvalue period is going to be 2.353 nm, which in terms of temperature should be around 235 ºC.

The measurement set began with a climatic chamber temperature of -16.5 ºC (the temperature when the climatic chamber was switch off was -20 ºC but after taking some time to homogenize the oven temperature it dropped to -16.5 ºC)

and it last until the climatic chamber reached -1 ºC. This means a temperature change of 15.5 ºC, impossible to measure if the KLT routine was not being used. An electrical frequency response measurement was recorded when the temperature dropped 0.5 ºC from the previous value and the impulse response was calculated for every measurement and the highest eigenvalue of the sample created by the FBG inside the climatic chamber was extracted. As can be seen in Fig. 3.12 the highest eigenvalue follows the temperature change (the eigenvalue value is around a minimum of one period).

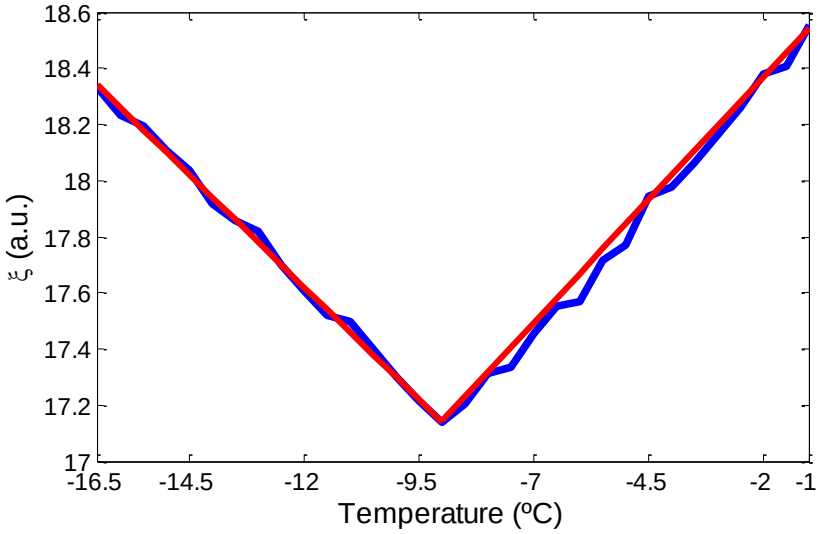

Fig. 3.12. Highest rank eigenvalue calculated by the KLT routine for the sample generated by the FBG fixed inside the climatic chamber (blue trace) and linear fitting (red trace)

As can be seen, from Fig. 3.12, the eigenvalue follows the temperature change with a resolution at least smaller than 0.5 ºC (5 pm of Bragg wavelength change). Although the eigenvalue behavior is not as linear as it was expected. This effect is created by the poor accuracy of the climatic chamber in retrieving the actual value of the temperature inside the chamber. This accuracy is around 1 ºC. If the real measurement (blue trace) is compared to the linear fitting (red trace), the maximum error introduced is 0.4 ºC, under the temperature change interval between consecutive measurements. Source power fluctuations, modulator Q-point drifts and dispersion changes of the chirped FBG are expected to be minimal since the temperature was controlled in the room along the entire experiment.

In order to have the same resolution using the wavelength to radio-frequency delay mapping presented in the previous chapter, taking into account the dispersive media used, the temporal distance between consecutive points in the impulse response should be 0.85 ps. This means an equivalent electrical

frequency bandwidth of 1,176.5 GHz. In order to accomplish this requirement, around 500 zeroes should have been added between two consecutive raw data points. This would produce a great decreasing in the interrogation speed and it would make the interrogation technique much less attractive from the computational perspective.

A different FBG was fixed inside the climatic chamber in order to perform a different measurement and to assess again the interrogation technique. This time, it was the third FBG the chosen one (1,554 nm) and the measurement bandwidth was increased to 20 GHz. The produced temperature ramp was in this occasion from -18 ºC to 0 ºC. In Fig. 3.13 it is shown the sample created by this FBG for the different temperatures.

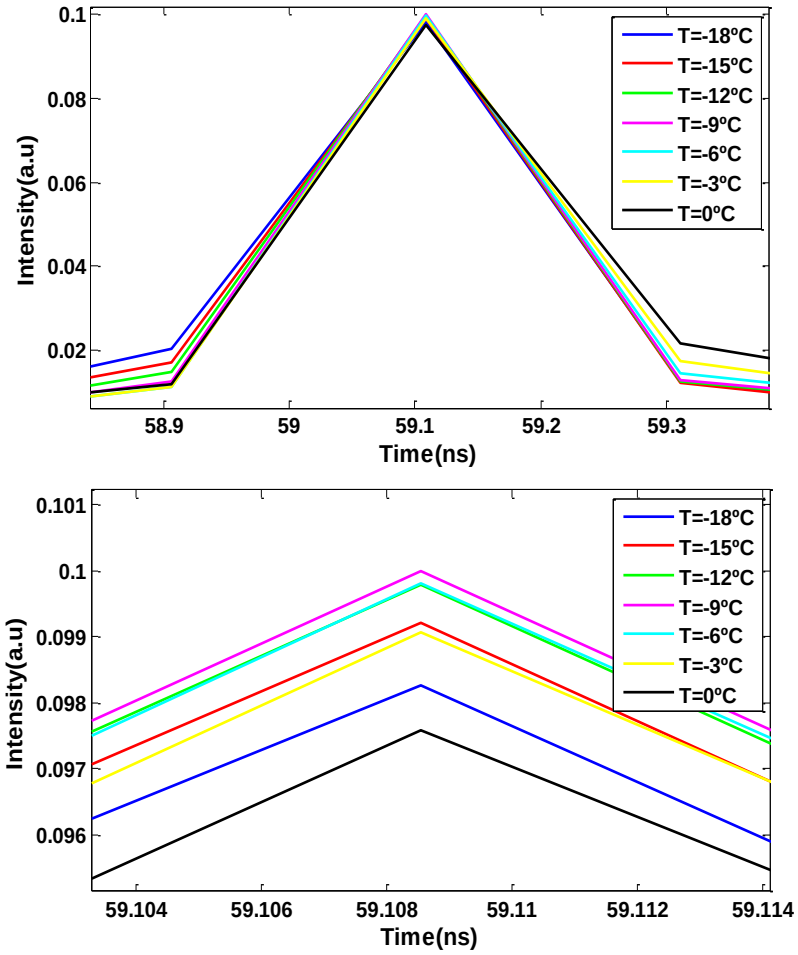

Fig. 3.13. Upper: FBG created sample in the impulse response for different temperatures. Lower: Zoom view of the sample maximum

As can be seen, the maximum value changes for the different temperatures but not its position. The KLT routine, as it is shown in Fig. 3.14, is able to retrieve the temperature change, regardless.

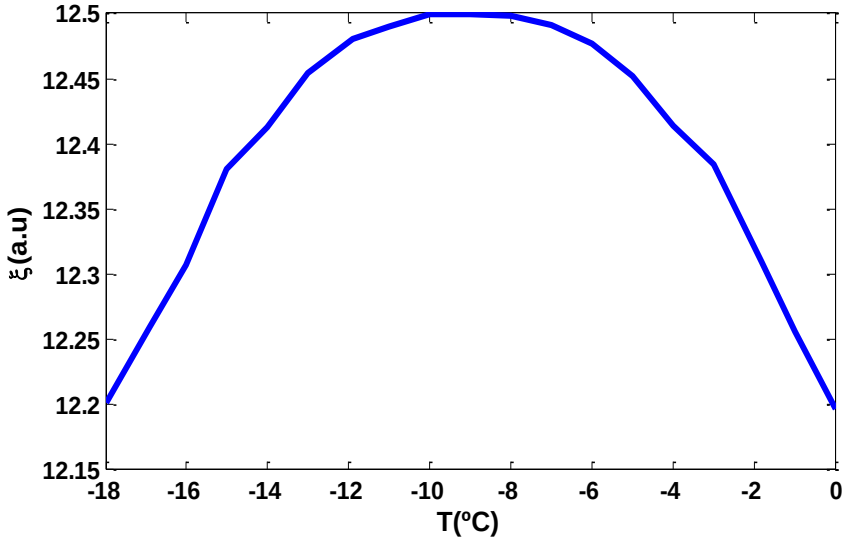

Fig. 3.14. Values of the highest rank eigenvalue for different temperatures

3.7 Conclusions

In this chapter, the Karhunen-Loeve transform is used to retrieve the sensing information of a multiplexed sensor formed by four FBGs in cascade. The working principle of the system is based on the use of a filtering microwave photonics technique to record the Bragg wavelengths of several FBGs in cascade in the radio-frequency delays on the impulse response of the fiber optics link. Additionally, the wavelength mapping is performed by a dispersive media, role played here by a chirped FBG.

The radio-frequency waves generated by a VNA modulate the light coming from a broadband source in the electro-optic modulator in order to capture the electrical frequency response of the system. Through IFFT calculation the impulse response of the system is retrieved, impulse response where the FBG samples are embedded in a *sinc* peak. Thanks to the coarse sampling in the impulse response, the *sinc* shaped samples are depicted only by four points, causing that any environmental change would be seen as an amplitude sample shift instead of a sample delay shift. These amplitude changes are followed by the eigenvalues calculated by the KLT routine, allowing to measure

continuously the temperature change although the delay change produced is smaller than the temporal resolution in the impulse response.

The measurement resolution does not depend on the RF bandwidth or the dispersion as in the technique explained in the previous chapter. These parameters are important in order to ensure that the delay samples are not overlapped, it is to say not aliasing is present in the impulse response.

This interrogation technique has been experimentally demonstrated with a fiber link where four FBGs with different wavelengths and reflected power are written. A temperature change smaller than the resolution given by the temporal distance between consecutive points in the impulse response has been produced, proving that the KLT routine improves the resolution of the system without the need to insert zeroes in the raw VNA data. Temperature changes of 0.5 ºC (Bragg wavelength changes of 5 pm) have been followed by the highest eigenvalue calculated by the KLT routine, reducing by a 500 fold the number of points needed to do so with the previous technique presented.

An increment in the number of sensors only implies a small increment in the computational complexity and measurement time, since the electrical spectrum measurement and IFFT calculation times are not dependent on the number of sensors. Once the impulse response has been calculated only four points are needed for the correct interrogation of each sensor.

Finally, it is important to notice the advantages of this new interrogation technique over conventional interrogation methods based on tracking the Bragg wavelength of the FBG in the optical spectrum. In particular, the present technique does not require tunable sources or receivers, showing at the same time an improvement in the accuracy of wavelength determination to the sub-pm level and the possibility to demodulate arrays of FBGs with the same nominal wavelength.

References

[1] A. Javernik and D. Donlagic, "High-Speed Interrogation of Low-Finesse Fabry–Perot Sensors Using a Telecom DFB Laser Diode," in *Journal of Lightwave Technology*, vol. 35, no. 11, pp. 2280-2290, 1 June1, 2017.

[2] T. Yamaguchi and Y. Shinoda, "Multichannel High-Speed Fiber Bragg Grating Interrogation System Utilizing a Field Programmable Gate Array," in IEEE Sensors Letters, vol. 2, no. 1, pp. 1-4, March 2018, Art no. 5500204.

[3] M. Perry, P. Orr, P. Niewczas and M. Johnston, "Nanoscale Resolution Interrogation Scheme for Simultaneous Static and Dynamic Fiber Bragg Grating Strain Sensing," in Journal of Lightwave Technology, vol. 30, no. 20, pp. 3252-3258, Oct.15, 2012.

[4] C. Wang and J. Yao, "Ultrafast and Ultrahigh-Resolution Interrogation of a Fiber Bragg Grating Sensor Based on Interferometric Temporal Spectroscopy," in *Journal of Lightwave Technology*, vol. 29, no. 19, pp. 2927-2933, Oct.1, 2011.

[5] U. Glombitza and E. Brinkmeyer, "Coherent frequency-domain reflectometry for characterization of single-mode integrated-optical waveguides," in Journal of Lightwave Technology, vol. 11, no. 8, pp. 1377-1384, Aug. 1993.

[6] K. Yüksel, M. Wuilpart, V. Moeyaert and P. Mégret, "Novel Monitoring Technique for Passive Optical Networks Based on Optical Frequency Domain Reflectometry and Fiber Bragg Gratings," in *IEEE/OSA Journal of Optical Communications and Networking*, vol. 2, no. 7, pp. 463-468, July 2010.

[7] L. Zhou *et al*., "Distributed Strain and Vibration Sensing System Based on Phase-Sensitive OTDR," in *IEEE Photonics Technology Letters*, vol. 27, no. 17, pp. 1884-1887, 1 Sept.1, 2015.

[8] M. Ohashi, "Novel OTDR Technique for Measuring Relative-Index Differences of Fiber Links," in *IEEE Photonics Technology Letters*, vol. 18, no. 24, pp. 2584-2586, Dec.15, 2006.

[9] A. Domínguez-López, A. López-Gil, S. Martín-López and M. González-Herráez, "Signal-to-Noise Ratio Improvement in BOTDA Using Balanced Detection," in *IEEE Photonics Technology Letters*, vol. 26, no. 4, pp. 338-341, Feb.15, 2014.

[10] C. A. Galindez Jamioy and J. M. Lopez-Higuera, "Decimeter Spatial Resolution by Using Differential Preexcitation BOTDA Pulse Technique," in *IEEE Sensors Journal*, vol. 11, no. 10, pp. 2344-2348, Oct. 2011.

[11] F. Wang, W. Zhan, X. Zhang and Y. Lu, "Improvement of Spatial Resolution for BOTDR by Iterative Subdivision Method," in Journal of Lightwave Technology, vol. 31, no. 23, pp. 3663-3667, Dec.1, 2013.

[12] Q. Li, J. Gan, Y. Wu, Z. Zhang, J. Li and Z. Yang, "High Spatial Resolution BOTDR Based on Differential Brillouin Spectrum Technique," in *IEEE Photonics Technology Letters*, vol. 28, no. 14, pp. 1493-1496, 15 July15, 2016.

[13] Yao, "Microwave Photonics," in *Journal of Lightwave Technology*, vol. 27, no. 3, pp. 314-335, Feb.1, 2009.

[14] R. A. Minasian, "Photonic signal processing of microwave signals," in *IEEE Transactions on Microwave Theory and Techniques*, vol. 54, no. 2, pp. 832-846, Feb. 2006.

[15] J. Hervás *et al*., "Microwave Photonics for Optical Sensors," in *IEEE Journal of Selected Topics in Quantum Electronics*, vol. 23, no. 2, pp. 327-339, March-April 2017, Art no. 5602013.

[16] J. Hervás, C. R. Fernández-Pousa, D. Barrera, D. Pastor, S. Sales and J. Capmany, "An Interrogation Technique of FBG Cascade Sensors Using Wavelength to Radio-Frequency Delay Mapping," in *Journal of Lightwave Technology*, vol. 33, no. 11, pp. 2222-2227, June1, 1 2015.

[17] A. Amar, A. Leshem and M. Gastpar, "Recursive Implementation of the Distributed Karhunen-Loève Transform," in *IEEE Transactions on Signal Processing*, vol. 58, no. 10, pp. 5320-5330, Oct. 2010.

[18] Yingbo Hua and Wanquan Liu, "Generalized Karhunen-Loeve transform," in *IEEE Signal Processing Letters*, vol. 5, no. 6, pp. 141-142, June 1998.

[19] Xiang-Gen Xia and B. W. Suter, "On vector Karhunen-Loeve transforms and optimal vector transforms," in *IEEE Transactions on Circuits and Systems for Video Technology*, vol. 5, no. 4, pp. 372-374, Aug. 1995.

[20] Levent Sevgi, "Fourier Transform and Fourier Series," in *Electromagnetic Modeling and Simulation* , , IEEE, 2014, pp.

[21] William M. Siebert, "Fourier Transforms and Fourier's Theorem," in *Circuits, Signals, and Systems* , , MITP, 1985, pp.

[22] J. C. Das, "Fourier Analysis," in *Power System Harmonics and Passive Filter Designs* , , IEEE, 2015, pp.

[23] C. Maccone, "Advantages of Karhunen–Loève transform over fast Fourier transform for planetary radar and space debris detection," Acta Astronaut., vol. 60, nos. 8–9, pp. 775–779, May 2005.

[24] D. Tosi, "KLT-based algorithm for sub-picometer accurate FBG tracking with coarse wavelength sampling", IEEE Phot. Tech. Letters, vol. 27, no. 20, pp. 2134-2137, Oct. 2015.

Chapter 4

Coherent regime MWP interrogation technique

4.1 Introduction

One of the main applications of optical sensors is structural health monitoring [1-5]. In this field, the fiber is embedded in the structure of a building (bridge, tunnel, dam, pillar, etc) and monitors the condition of the structure in order to measure any change that could happen. The data provided by the sensor make it possible to assess whether the new condition or any change that has been produced is a threat for the safe operation of the structure or not.

To play this structure assessment role, distributed sensors [6] have been extensively used. Brillouin [7-9] and Rayleigh [10-11] scattering are the most used optical phenomena to ensure the safe condition of civil structures around the world. The main advantage of these techniques is the ability to use a standard single mode fiber as a continuous distributed sensor of up to several dozens of kilometers. But they also have several drawbacks. The main disadvantage is the poor signal to noise ratio (SNR) these kind of techniques show. On the one hand, Rayleigh scattering is an isotropic process in which light is scattered in every direction, so only a small portion of the scattered light is back reflected and therefore detected. This reduces a lot the efficiency of the process. On the other hand, in Brillouin scattering the gain spectrum is severely affected by noise. This reduces the accuracy of this technique and therefore it forces to average hundreds and even thousands of measurements in order to reduce noise effect.

FBGs, on the contrary, are efficient devices since they couple the reflected light at the Bragg wavelength in the back direction [12]. This increases the SNR and the efficiency of the whole process drastically. The problem is that an FBG is a point sensor, so only the places in which these gratings are inscribed inside the fiber are active and able to sense.

The best way to unite the advantages of all these scattering processes would be to fabricate a continuous long weak FBG [13]. But this represents a real challenge since the FBG length is limited in every fabrication setup around the world.

In this chapter, a cost-effective and viable alternative as well as a suitable interrogation technique are developed [14-15]. Instead of having a continuous long weak FBG, a series of weak FBGs are used. These FBGs are 9mm long and the distance between consecutive FBGs is 1mm. There are 500 FBGs in a 5 m piece of fiber but it could be scalable up to tens of thousands of FBGs. This

alternative maintains almost untouched the power efficiency of the continuous weak grating and surpass the complexity of the technological challenge of fabricating a long continuous weak FBG.

In order to interrogate such a device, a coherent MWP filtering technique has been developed and experimentally demonstrated. Hot spot detection and temperature measurement have been proved showing that this alternative is feasible and it shows some advantages compared to other scattering processes.

4.2 Operational principle

The operational principle of the interrogation technique is based on the interrogation of the sensor formed by the 500 FBGs as a MWP [16-18] filter but under coherent regime operation. The schematic representation of the system used to interrogate the sensor is depicted in Fig. 4.1.

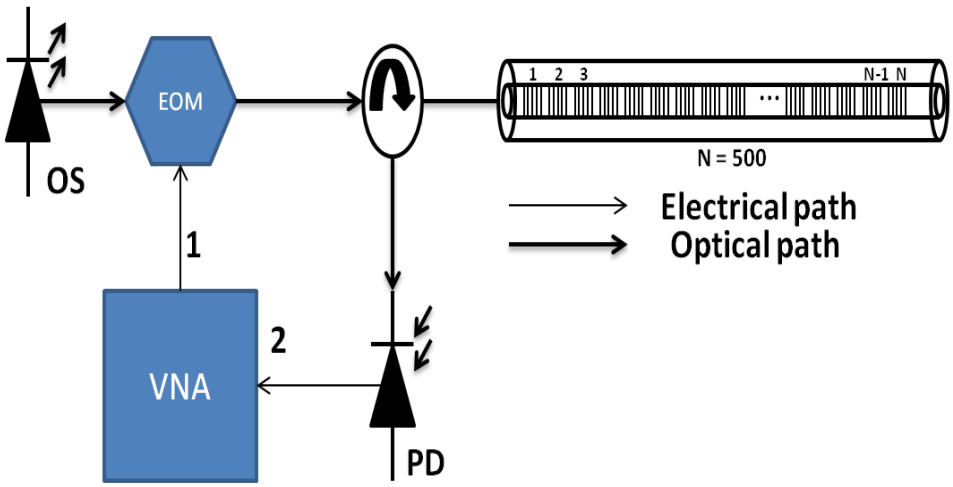

Fig. 4.1. Schematic of the setup used to interrogate the FBGs fiber. OS: optical source; EOM: electro-optic modulator; PD: photodetector; VNA: vector network analyzer.

The setup is based on the determination of the scattering parameter S_{21}. To measure this parameter, the VNA relates the outgoing signal in port 1 with the incoming signal in port 2. This scattering parameter is in this case the electrical response of the system.

The light coming from an optical source (OS) is modulated in the electro-optic modulator (EOM) by the microwave signals coming from the VNA. After this optical signal has been reflected by the FBGs, it reaches the photodetector in which the optical signal is photodetected and then fed to the VNA, in which the electrical response of the system is calculated.

The electrical response of the system is made up of the summation of the signals reflected by the FBGs and its appearance depends on the coherence time of the optical source. The coherence time can be calculated as follows:

$$\tau_c = \frac{1}{\Delta\nu} \tag{4.1}$$

being Δν the linewidth of the source in units of frequency. This coherence time is going to determine whether the samples created by the FBGs are going to interfere one to each other or, otherwise, they are going to be incoherently added.

If the coherent time is smaller compared to the time interval between consecutive samples, there is no coherent interaction between the reflections coming from the FBGs and the system would work under incoherent regime. On the contrary, if the coherent time is larger enough compared to the separation between consecutive samples, the system will work under coherent regime conditions. Incoherent regime is stable against environmental changes but it cannot provide so much information as the coherent operation does.

4.3 Incoherent regime

The incoherent regime is active when the coherence time of the source is smaller than the temporal distance between consecutive FBGs. This is accomplished through a filtered broadband source [19]. The bandwidth of this source is set to 2 nm, which means a coherence time of 4 ps (0.8 mm).

In this case, the electrical response is the summation of the samples created by the FBGs and can be expressed as [20]:

$$H(\omega) = \sum_{k=0}^{N-1} a_k e^{-j\Omega\tau_k} \tag{4.2}$$

where N is the number of FBGs, a_k is the sample weight (related to the FBGs reflectivity and thus positive), Ω is the angular frequency and τ_k is the sample delay.

As it has been said before, the fiber acting as sensor consisted of 500 equally spaced 9 mm long FBGs with a separation of 1mm between consecutive FBGs (one FBG every centimeter). The FBGs feature the same Bragg wavelength and a reflectivity smaller than 0.1%, so all the FBGs reflect a small portion of the incoming light. The temporal distance between consecutive samples would be in this case 100 ps.

With regards to filtering theory, this fiber could be seen as an incoherent FIR filter of 500 taps. As the samples generated by the FBGs are equally spaced, the

electrical response of the filter shows a periodical behavior. The period is commonly known as *Free Spectral Range* (FSR) and it is inversely proportional to the temporal distance between consecutive samples (T):

$$FSR = {}^{1}/_{T} \tag{4.3}$$

T is 100 ps in this particular case, so the FSR should be around 10 GHz. The measured electrical spectrum of this fiber can be seen in Fig. 4.2 a). As can be seen there are two passbands at 10 and 20 GHz respectively. It is also known from filtering theory that between two consecutive FSR, the electrical response must feature N-1 minima. This is precisely the principle that can be used in order to make use of such device as a sensor under incoherent regime conditions.

The FSR cannot change since the physical distance between consecutive FBGs is constant. If a section of the fiber is under a temperature or a strain change, the FBGs of that particular spot will experience a Bragg wavelength shift. So, if an optical filter is used to select only the particular wavelengths that these FBGs are reflecting and block the wavelengths reflected by the FBGs that are not suffering any temperature/strain change, the electrical response would feature the same FSR but the number of minima within that range would be smaller, since the number of samples would have change due to that only the reflections of the FBGs that are in the hot spot are contributing to this electrical response. This phenomenon can be seen in Fig. 4.3.

So, if this new situation is compared to the initial one, the FSR is the same but the number of minima and therefore the minima spacing should have change. This change can be used to measure the length of the fiber that is under this temperature/strain change.

In order to calculate in which precise part of the fiber is located the hot spot, a reference tap must be used. A reference tap is a unique reflector located far away from the fiber, in order to separate its contribution from the FBGs fiber contribution. When a reference tap is used in the system, the electrical response changes. This change can be seen in Fig. 4.2 b), in which the electrical response changes from the blue to the green one. The electrical response is quite similar to an impulse response of an amplitude modulated signal. On the one hand, the "period of the carrier" allows to calculate the distance between the reference tap and the center of the hot spot, locating this way the hot spot inside the FBGs fiber, as long as you know the distance between the end of the fiber and the reference tap. On the other hand, the "period of the modulating wave", which is the minima spacing within the initial situation, gives the length of the hot spot (how many FBGs are under the temperature/strain change).

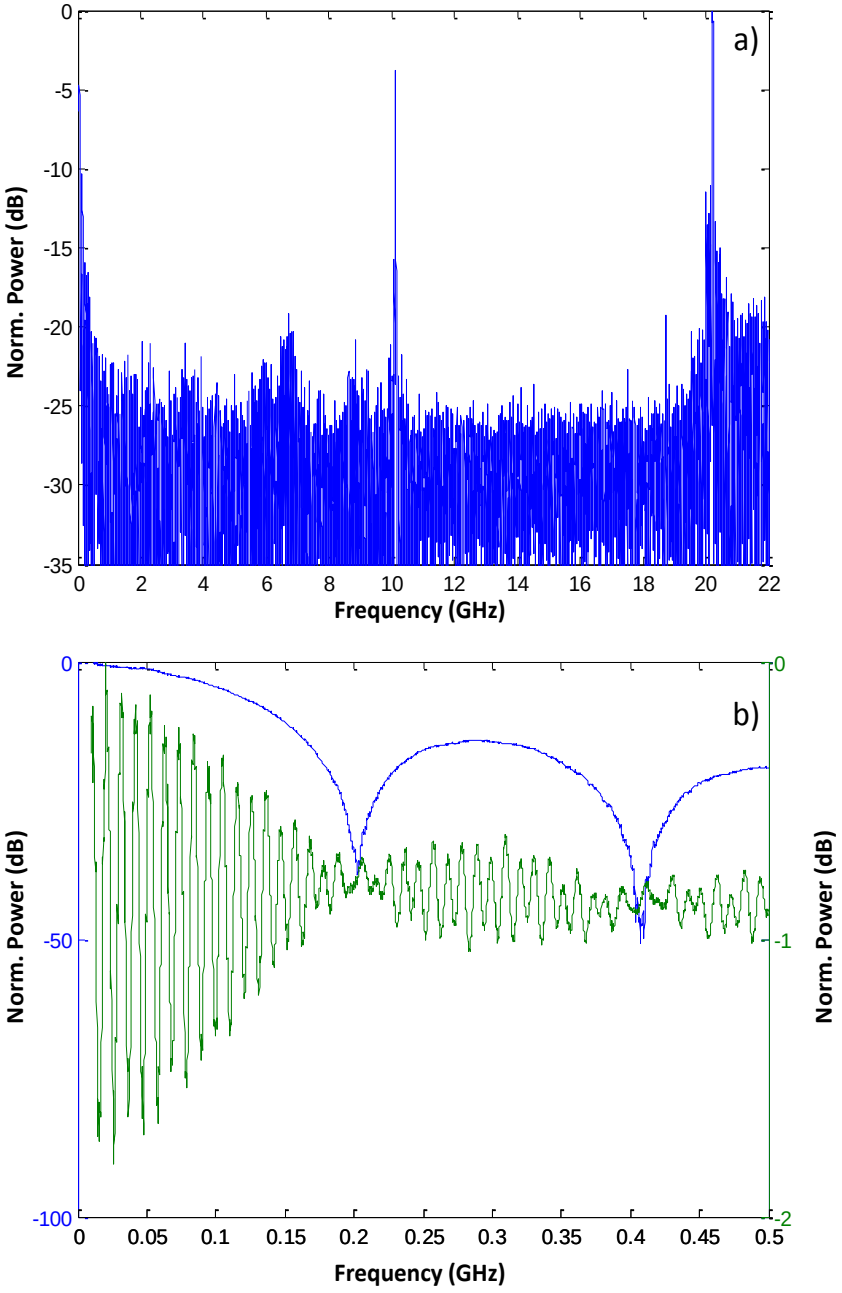

Fig. 4.2. a) Electrical spectrum of the FBGs fiber with passbands every 10 GHz. b) Zoom view of the electrical response around 500 MHz in the initial situation (blue trace) and when a reference tap is being used (green trace).

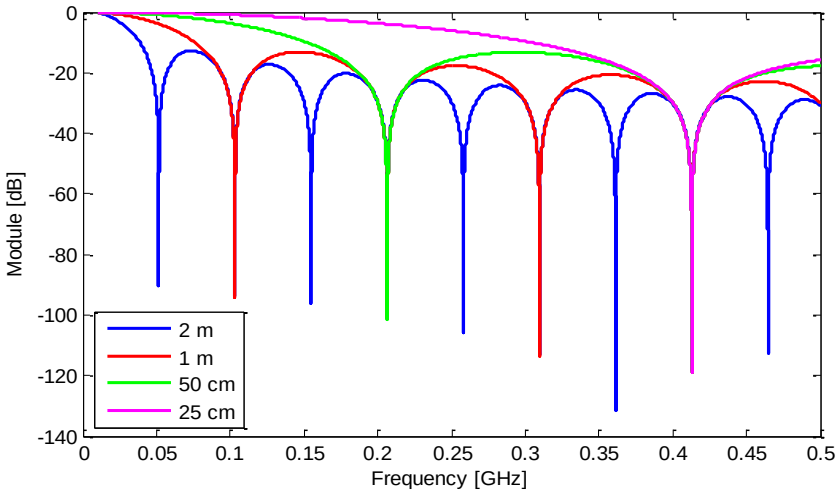

Fig. 4.3. Minima spacing for different number of FBGS (simulation)

However, this technique has some drawbacks. First, the position and length of the hot spot can be calculated with the electrical response as it has been explained in the previous page, but the temperature/strain experienced cannot be retrieved from this electrical spectrum. To do so, an optical spectrum analyzer should be used in order to measure the Bragg wavelength excursion to calculate, using the Bragg wavelength change coefficient related to temperature or strain, the temperature/strain change. The situation would be the one showed in Fig. 4.4 in which it can be seen the spectrum of the FBGs, both those which are still in the initial situation as well as those which are experiencing the temperature/strain change.

Moreover, the necessity to use the optical spectrum to calculate the temperature/strain change brings the second drawback. As the FBGs feature the same Bragg wavelength and the FBGs are weak, the initial temperature/change that the FBGs must suffer to be able to separate their contribution from the FBGs that are still in the initial situation is quite big. This would mean that small temperature/strain changes cannot be measured using this technique. Finally, there is a third inconvenient. As the optical filter only allows to monitor the condition of the FBGs that are inside the filter bandwidth, any FBG that remains outside this bandwidth will not be actively interrogated. So, the necessity to use the optical filter makes it impossible to monitor and check the condition of all the FBGs at the same time.

In order to overcome these drawbacks, the coherent regime interrogation is implemented [14].

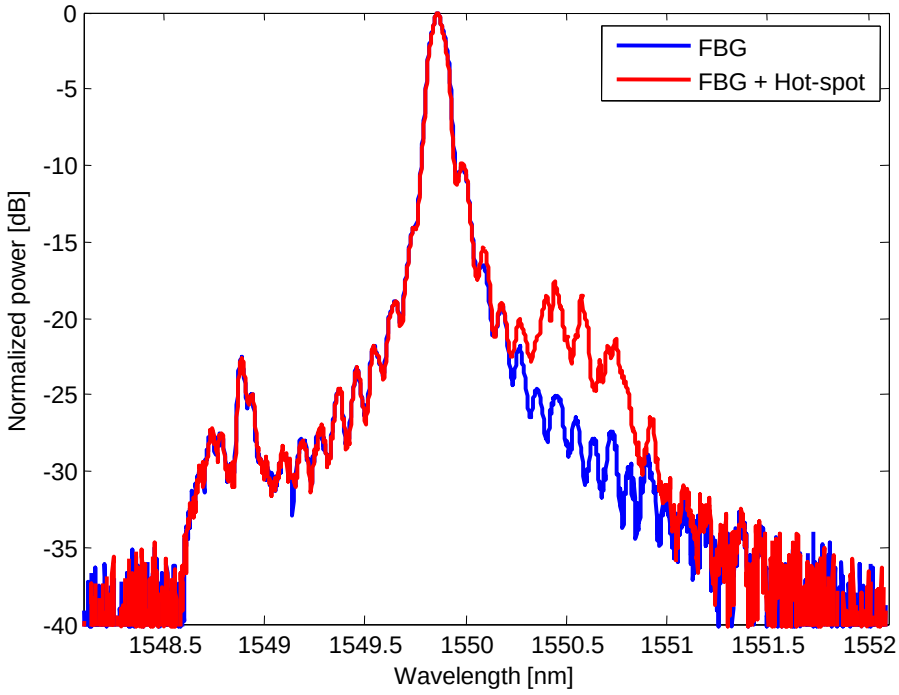

Fig. 4.4. Optical spectrum of the FBGs fiber in the initial situation (blue trace) and when a hot spot is created somewhere along the fiber (red trace).

4.4 Coherent regime

The main consequence of working under a coherent regime is that it makes the system sensitive to the optical phase, therefore the system is unstable due to environmental fluctuations but more information can be extracted from data [21]. This regime is acquired replacing the filtered broadband source with a laser diode. This laser features a linewidth of 10 MHz, which sets a coherence time of 31.83 ns (6.36 m), more than enough to guarantee coherent operation.

Dependency on the optical phase changes completely the appearance of the electrical spectrum. As can be seen in Fig. 4.5 a), the electrical response is completely different to the one showed in Fig. 4.2 a), effect created by the coherent interaction between the different samples reflected by the FBGs. Although the electrical response seems noisy, a data pattern can be extracted from the magnitude and phase information of the electrical response. It cannot be extracted using an eye-based strategy, as it was the case of the incoherent interrogation, but it can be extracted calculating the impulse response thanks to the calculation of the inverse fast Fourier transform (IFFT) of the electrical spectrum, which is a cost-effective algorithm, computationally speaking. This

way the sensing information recorded in the physical parameters of the sensor can be easily accessible.

The impulse response of the system can be expressed as:

$$h_B(t) = B\sum_{k=0}^{N-1} a_k e^{j\pi B(t-\tau_k)} sinc[B(t-\tau_k)] \quad (4.4)$$

where B is the electrical bandwidth, a_k is the sample complex coefficient (directly related to the reflectivity of each FBG at the laser working wavelength), and sinc(x)=sin(πx)/πx. As can be extracted from (4.4), every sample created by any of the FBGs is embedded in a sinc peak in the impulse response, sinc peak whose linewidth is inversely proportional to the bandwidth of the electrical measurement [22]. This can be seen in Fig. 4.6, in which an FBG created sample in the impulse response is showed for different bandwidths. As can be seen, the higher the bandwidth, the smaller the linewidth of the sinc peak of the sample in the impulse response.

In Fig. 4.5 b), it can be seen the impulse response of the 5 m of fiber. As can be observed, this impulse response is all but random. The 5m of fiber appear clearly (signal from 290 to 340 ns approximately), with an SNR higher than 16 dB. This impulse response has been acquired after averaging 15 impulse responses with the fiber under the same conditions. This is performed in order to reduce noise and to smooth the saw tooth appearance typical of coherent measurements [21]. This 15 measurements averaged represent a trade-off between quality and speed of the measurement and it is a small number compared to the hundreds or even thousands of measurements that need to be averaged in Brillouin or Rayleigh scattering based systems.

The electrical response shown in Fig. 4.5 a) was recorded while the laser was emitting at the Bragg wavelength of the FBGs (the difference in power seen in the impulse response of Fig. 4.5 b) is due to small Bragg wavelength errors in the inscription of the FBGs during fabrication process and coherent effects typical of this kind of measurements).

Therefore, as the laser is emitting at the Bragg wavelength, if any of the FBGs experiences a temperature/strain shift, the Bragg wavelength would change accordingly and as a consequence the reflected power coming from that FBG at the laser particular wavelength would be smaller. This is graphically pictured in Fig. 4.7.

This reduction in power will appear in the impulse response trace, allowing this way not only to locate the section of the fiber that is under the temperature/strain change but the temperature/strain change itself at the same time while the rest of the fiber is still being monitored. This is in opposition to

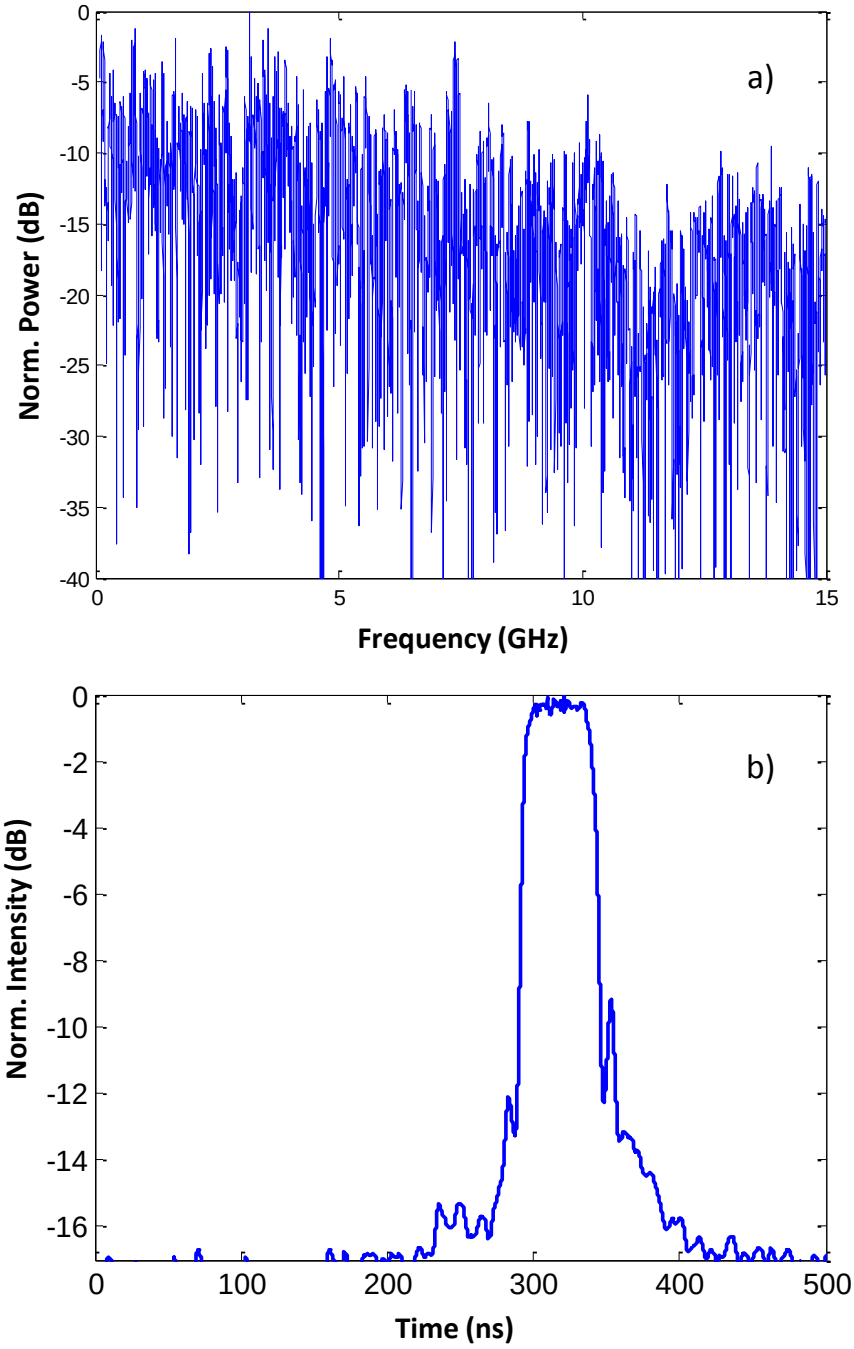

Fig. 4.5. a) Electrical response of the 5m fiber when the system works under coherent regime. b) Impulse response acquired after averaging 15 measurements recorded when the fiber is under the same conditions

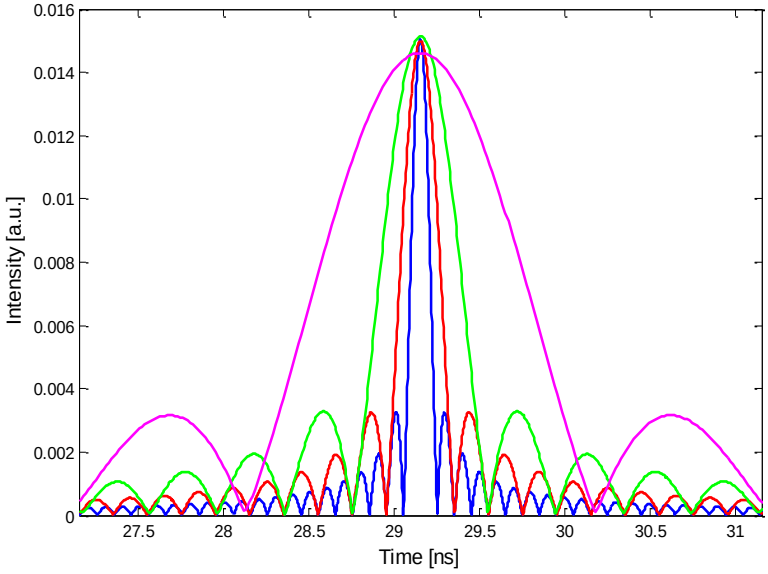

Fig. 4.6. FBG created sample for different bandwidths. Blue: 10 GHz; Red: 5 GHz; Green: 2.5 GHz; Purple: 1 GHz.

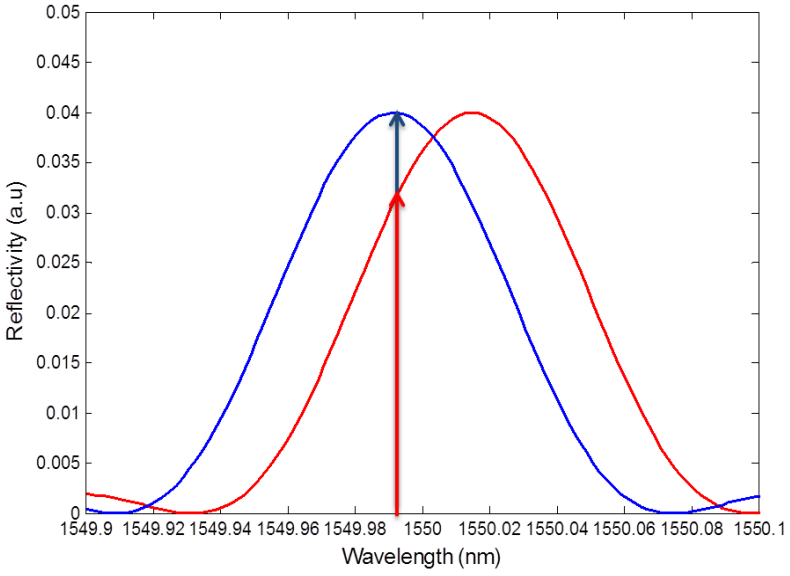

Fig. 4.7. Graphical representation of principle of operation of the sensing system under coherent regime. Blue and red traces represent the FBG in the initial situation and when a temperature/strain change is produced. Blue and red arrows represent the laser reflected power in both previous situations.

what happened with the interrogation under incoherent regime, in which was impossible to locate the hot spot and measure the temperature at the same time using the electrical measurements.

4.5 Sensor characteristics

The sensor has been fabricated using the so called Draw Tower Grating (DTG) technique. This technique is based on the inscription of the gratings during the fabrication process of the fiber. Prior to coating application, the fiber is exposed to ultra-violet (UV) light in order to inscribe a grating in a controlled way. The length and location of the gratings are controlled by the synchronization of the laser exposure and the pulling speed of the system.

In the traditional FBG inscription process, the fiber is uncoated before the FBG is inscribed, mainly because the regular coating materials used with standard fiber are not UV transparent. This process creates problems involving fiber strength, which ultimately can derive in problems with real applications like structural health or platform monitoring limitations. Moreover, if an array of FBGs needs to be fabricated following this traditional fabrication process, probably there will be a limitation in the number of sensors that can be cascaded or there will be some sort of splicing or connection that will threaten the structural strength of the fiber. Any of these problems are not present when the DTG technique is used [23-24] to fabricate the sensing device since there is no limitation in the number of sensors, there is no necessity to splice or connect different fibers and there are no uncoated or recoated sections along the fiber.

Examples of thousands of small weak FBGs cascaded in a single fiber have been already published proving the critical strength and the opportunities this fabrication technique brings about. In the particular case of this work, the fiber used was just a proof of concept used to validate the kind of sensor device and the interrogation technique.

The fiber that was used to validate the interrogation technique is a 5 m long fiber featuring five hundred 9 mm long FBGs with a 1 mm separation between the end and the beginning of two consecutive FBGs. This means an FBG every centimeter. The reflectivity of each one of the FBGs is smaller than 0.1%, which guarantees both that enough light is going to reach the last FBG as well as that the light reflected by the last FBG is going to reach the detector and is not going to be extremely depleted by reflection in the rest of the FBGs.

In Fig. 4.8 it can be seen the overall spectrum of the fiber, which is the superimposed spectra of the 500 FBGs.

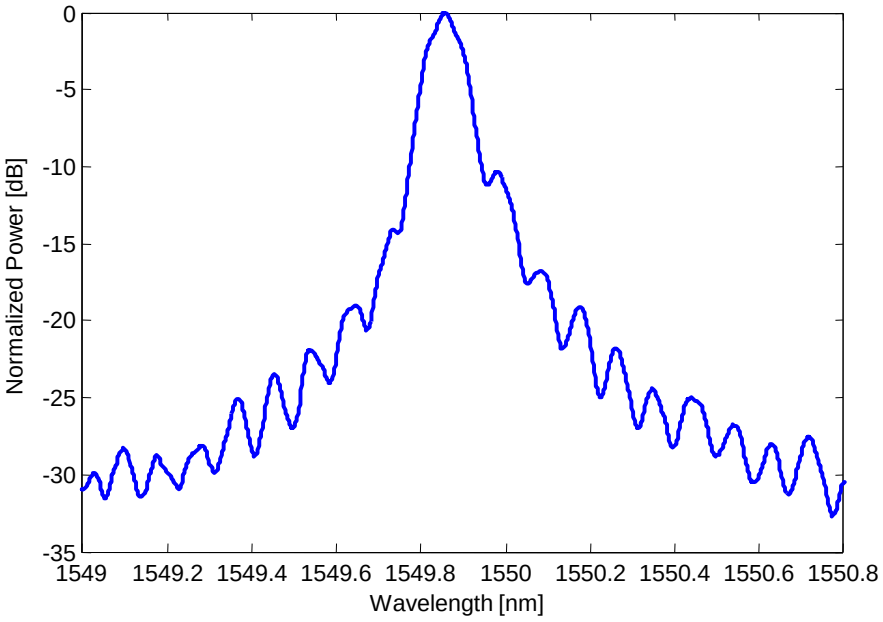

Fig. 4.8. Reflection spectrum of the 5m fiber

The Full Width Half Maximum (FWHM), which is the bandwidth at -3 dB from the maximal value, is 0.1 nm. This spectrum is the superposition of the FBGs spectrum, superposition that causes a broadening in the spectrum. So it is expected that the spectrum of the individual FBG is actually narrower than the one showed in Fig. 4.8.

Running a simulation to get the measured result showed in Fig. 4.8 (-3 dB bandwidth of 0.1 nm and an overall reflectivity of 24.77%) it is found that the actual bandwidth of one of the 9 mm FBGs to have an overall reflectivity of 24.77% is 0.085 nm, and the individual reflectivity should be 0.06%. To find these values a 9 mm FBG has been simulated and it has been calculated the overall spectrum of having 500 FBGs such as that one. The simulated FBG is a uniform one and the parameter that has been modified in each case is the refractive index change caused by the UV light, Δn.

Taking the FBG shown in Fig. 4.9 as the model used to create the 500 FBGs fiber, the overall reflectivity is 24.7% but the overall bandwidth is around 0.09 nm, slightly smaller compared to the bandwidth of the real fiber. The difference in bandwidth between the real fiber and the simulation probably is created by a slight detuning in the Bragg wavelength of the real FBGs [25]. A small deviation around the desired value would be seen in the superimposed spectrum as a widening of the passband. This would mean that, likely, the reflectivity of

the individual real FBGs is probably a bit greater than the theoretical value calculated.

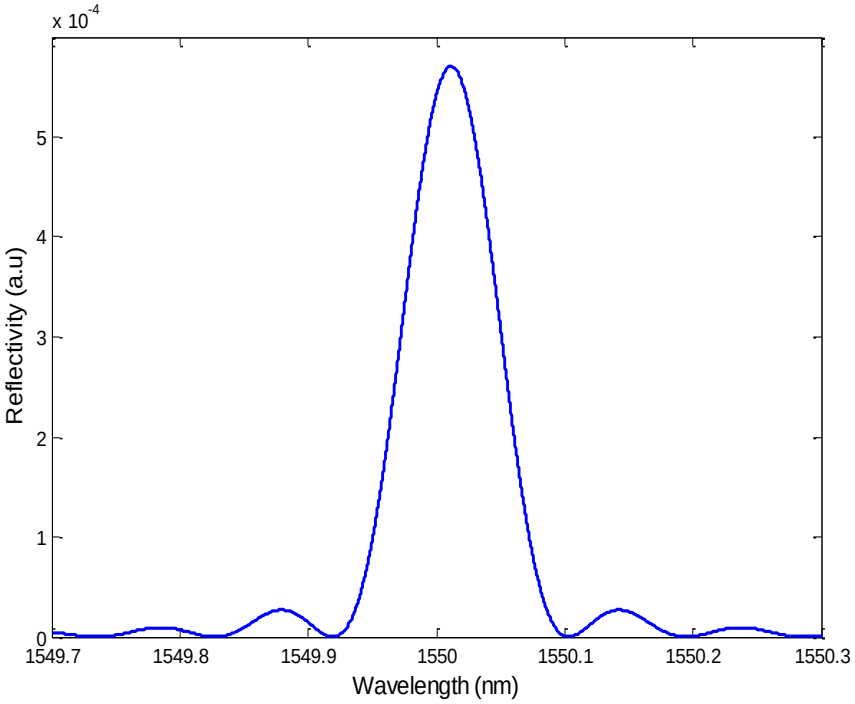

Fig.4.9. Simulated individual FBG

4.6 Experimental measurements

The experimental setup used to perform the measurements is shown in Fig. 4.10. This setup was used to perform two different sets of measurements. In the first measurement set, the last section of the fiber (2 m approximately) was fixed inside a climatic chamber in order to produce a temperature ramp and measure the technique sensitivity related to a temperature change. In the second set, a section of the fiber close to the center of it was kept in a hot bath. The goal of this second measurement set was to measure the relationship between the resolution of the interrogation technique and the bandwidth of the electrical measurement. For this two sets of measurements the trade off of averaging 15 measurements was kept. As it has been said before this means a compromise between speed of the measurement and the quality of it.

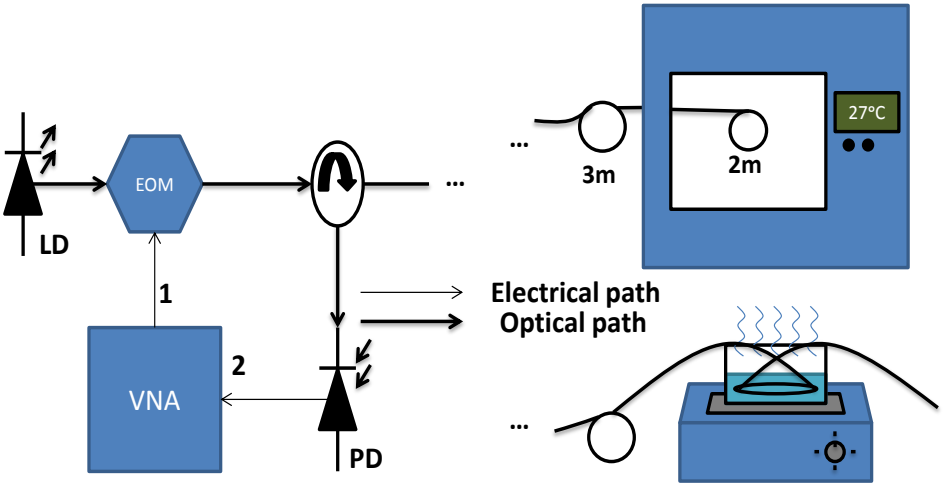

Fig. 4.10. Measurement setup used to perform the two different measurement sets

For the two sets of measurements the laser was emitting at 1,549.86 nm, the central wavelength of the superposed FBGs spectrum, and its output power was 8 dBm.

As it has been stated before, the first set of measurements started with the last two meters of the fiber inside the climatic chamber and the first 3 meters of the fiber were out of the climatic chamber in a temperature controlled situation (room temperature around 22 ºC). The climatic chamber had a resolution of 1 ºC. Therefore the temperature ramp was set up with a step of 2 ºC. The programmed total temperature change was 10 ºC (from 22 ºC to 32 ºC). The VNA measurement bandwidth was 15 GHz and the number of points used in this measurement was 16,001. Although the electrical spectra measured by the VNA had the noisy appearance showed in Fig. 4.5 a), the calculation of the impulse responses retrieved the data that can be seen in Fig. 4.11 a). As can be seen the FBGs section is still visible and the power reflected by the end portion of the fiber is decreasing as the temperature increases, which is in complete agreement with the theoretical expectations. As the laser is emitting all the time at the same wavelength, any temperature change will shift the Bragg wavelength of the FBGs in the hot spot. This makes these FBGs reflect less power (see Fig. 4.7), what can be finally extracted from the impulse response of Fig. 4.11 a).

In this impulse response can be seen that the averaged intensity reflected by the last two meters of fiber suffers a decrement of 6 dB when the temperature changes 10 ºC. But the intensity variation related to temperature is not linear, as can be seen in Fig. 4.11 b). The reflected power decrement becomes sharper for

higher temperatures (bigger change compared to the initial situation) which is in complete agreement with the regular shape of the FBGs.

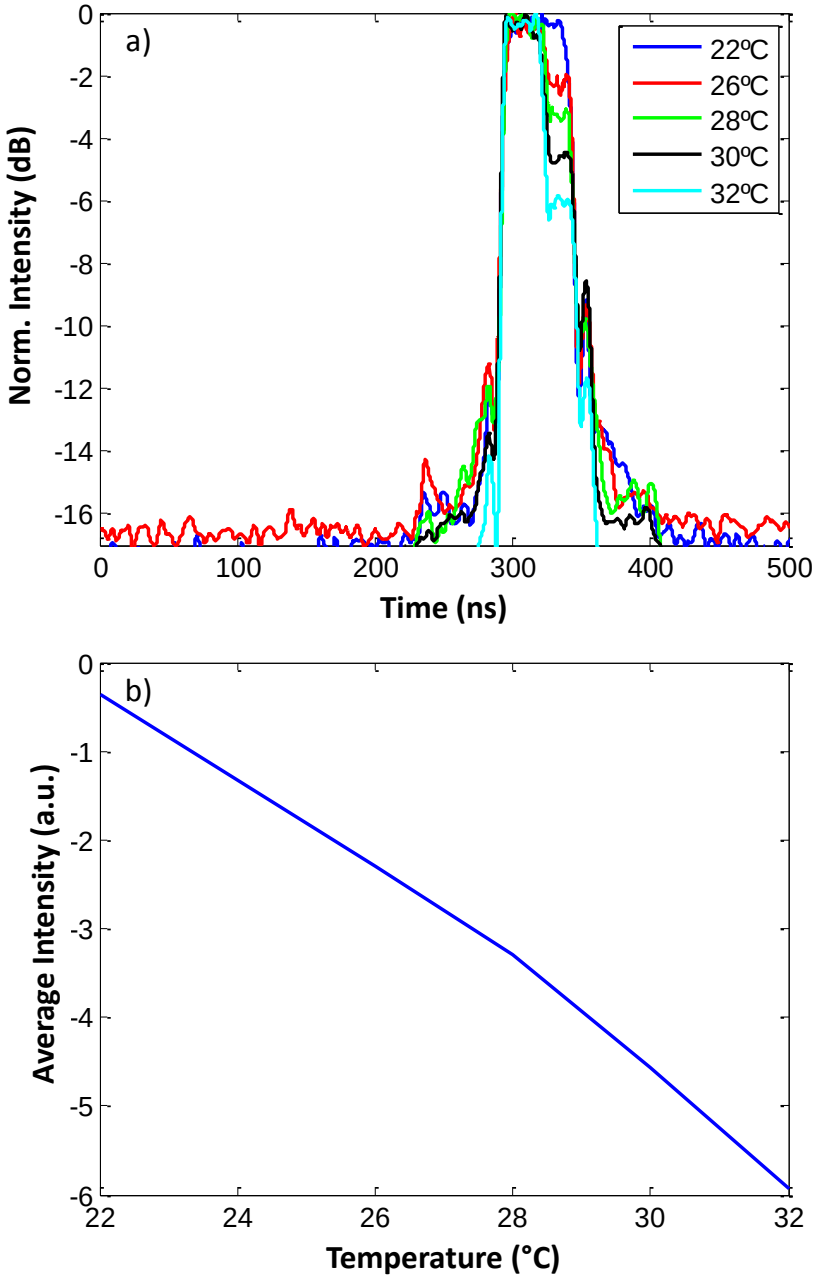

Fig. 4.11. a) Impulse response retrieved for different temperatures. b) Average intensity of the last 2m of fiber related to temperature

In the second measurement set 20 cm of the fiber located around the middle of it were fixed at the bottom of a small container in order to fill it with water and perform a hot bath. In order to study the relationship between the electrical parameters of the measurement and the resolution of the interrogation technique, the same situation was measured with different electrical bandwidths (15 and 1 GHz respectively). In both measurements the distance between consecutive points in the electrical measurement was 1 MHz. The results of the measurement can be seen in Fig. 4.12.

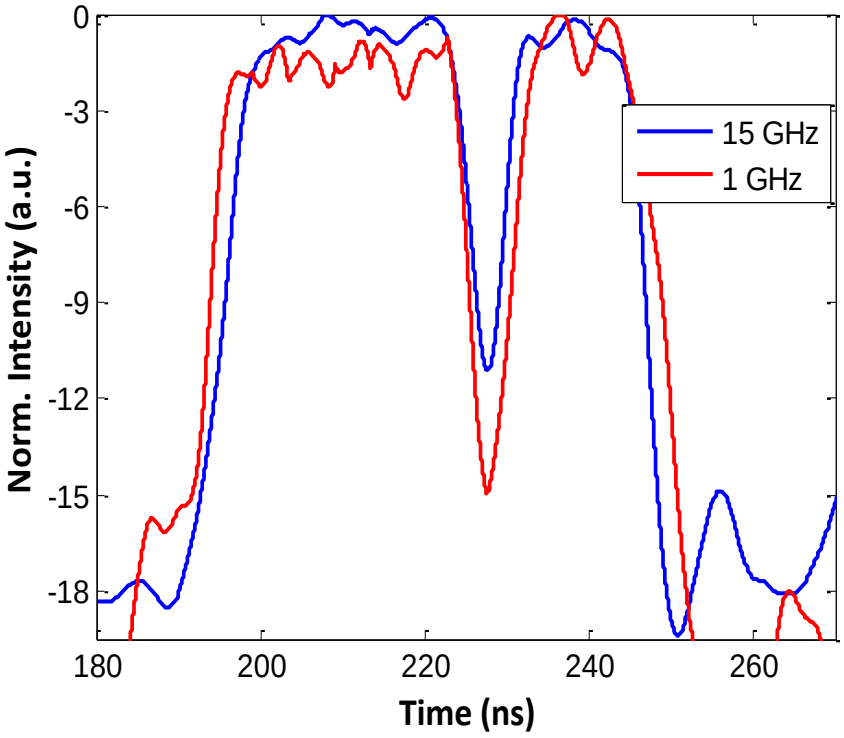

Fig. 4.12. Impulse response of the fiber for different bandwidths used in the electrical measurement.

As can be observed the same spot appears as heated in both measurements but there are some differences. The first difference is that the notch of the 1 GHz measurement is deeper than the other. This is caused by the temperature of the water, temperature that was not being controlled through this set of measurements so the water temperature was different for both situations (40 ºC and 47 ºC for the 15 GHz and the 1 GHz measurement respectively, room temperature at 22 ºC).

The second difference is that the hot spot, and also the whole fiber, seem longer in the 1 GHz measurement. This is caused by the width of the sinc shaped samples of the FBGs. According to (4.4) the width of the sinc samples is inversely proportional to the bandwidth of the electrical measurement (B). So, for a lower frequency more samples are interfering at the same spot. This makes the spot and the entire fiber look longer. Therefore the resolution in this kind of measurements is inversely proportional to the electrical bandwidth, just like in the incoherent measurement (the higher the bandwidth the better the resolution). It also creates bigger ripples at the top of the trace in the 1 GHz case.

But as it has been proven by these experimental measurements the interrogation technique is able not only to locate the hot spot inside the fiber but to measure the temperature change as well and it would be possible to measure different hot spots experiencing different environmental conditions along the fiber.

4.7 Conclusions

In this chapter the coherent interrogation of a MWP filter formed by 500 FBGs in cascade has been experimentally proven. This is an alternative to other distributed sensor interrogation techniques like Brillouin or Rayleigh scattering or to more complex devices like a long continuous weak FBG. This technique is simpler and more efficient than the previous mentioned counterparts.

The fiber used to experimentally test the interrogation technique is a 5 m fiber with 500 weak FBGs in cascade. These FBGs are 9 mm long and there is one FBG every centimeter. The individual reflectivity is around 0.06% and since the Bragg wavelength of all of them is the same the overall reflectivity is 24.77%. The fiber configuration could be extended up to hundreds of even thousands of meters.

Such a device is interrogated using a MWP filtering technique under coherent operation. To achieve this regime, a narrowband source must be used in order to ensure that the coherence time of the source is much bigger than the temporal distance between consecutive sensors, allowing this way the reflected samples to interact coherently among them. Coherent regime is by far more unstable than incoherent regime but more information can be extracted using this method in comparison.

Although the electrical response measured by the VNA appears to be quite noisy and random it possess all the sensing information that is needed. In order to extract this information, the IFFT of the electrical response is calculated, and 15 of these impulse responses are averaged in order to reduce the noisy appearance typical from coherent measurements. The impulse response calculated this way is all but random and the signal reflected by the FBGs is clearly seen. When a section of the fiber experiences a temperature or a strain change, the Bragg wavelength of the FBGs of that section changes and therefore

the reflected power at the laser emitting wavelength coming from those FBGs is smaller. This reduction can be clearly seen in the impulse response. This way the hot spots can be detected along the fiber as well as the strain/temperature that is affecting the FBGs of those sections.

The advantages of the interrogation technique and the device used as sensor are the reduction in the amount of averaging needed and in the amount of optical power injected to the system compared to Rayleigh or Brillouin scattering systems and the simplicity of the device used compared to the long continuous weak FBG alternative.

References

[1] J. M. Lopez-Higuera, L. Rodriguez Cobo, A. Quintela Incera and A. Cobo, "Fiber Optic Sensors in Structural Health Monitoring," in Journal of Lightwave Technology, vol. 29, no. 4, pp. 587-608, Feb.15, 2011.

[2] Y. Zhao, Y. Zhu, M. Yuan, J. Wang and S. Zhu, "A Laser-Based Fiber Bragg Grating Ultrasonic Sensing System for Structural Health Monitoring," in *IEEE Photonics Technology Letters*, vol. 28, no. 22, pp. 2573-2576, 15 Nov.15, 2016.

[3] M. Vidakovic, C. McCague, I. Armakolas, T. Sun, J. S. Carlton and K. T. V. Grattan, "Fibre Bragg Grating-Based Cascaded Acoustic Sensors for Potential Marine Structural Condition Monitoring," in *Journal of Lightwave Technology*, vol. 34, no. 19, pp. 4473-4478, 1 Oct.1, 2016.

[4] A. Cusano *et al*., "Experimental modal analysis of an aircraft model wing by embedded fiber Bragg grating sensors," in *IEEE Sensors Journal*, vol. 6, no. 1, pp. 67-77, Feb. 2006.

[5] S. Jinachandran *et al*., "Fabrication and Characterization of a Magnetized Metal-Encapsulated FBG Sensor for Structural Health Monitoring," in *IEEE Sensors Journal*, vol. 18, no. 21, pp. 8739-8746, 1 Nov.1, 2018.

[6] H. Y. Fu, H. L. Liu, W. H. Chung and H. Y. Tam, "A Novel Fiber Bragg Grating Sensor Configuration for Long-Distance Quasi-Distributed Measurement," in IEEE Sensors Journal, vol. 8, no. 9, pp. 1598-1602, Sept. 2008.

[7] M. A. Soto, P. K. Sahu, G. Bolognini and F. Di Pasquale, "Brillouin-Based Distributed Temperature Sensor Employing Pulse Coding," in IEEE Sensors Journal, vol. 8, no. 3, pp. 225-226, March 2008.

[8] F. Ravet, F. Briffod, B. Glisic, M. Nikle and D. Inaudi, "Submillimeter crack detection with brillouin-based fiber-optic sensors," in *IEEE Sensors Journal*, vol. 9, no. 11, pp. 1391-1396, Nov. 2009.

[9] A. Minardo, R. Bernini, L. Amato and L. Zeni, "Bridge Monitoring Using Brillouin Fiber-Optic Sensors," in *IEEE Sensors Journal*, vol. 12, no. 1, pp. 145-150, Jan. 2012.

[10] Y. Koyamada, M. Imahama, K. Kubota and K. Hogari, "Fiber-Optic Distributed Strain and Temperature Sensing With Very High Measurand Resolution Over Long Range Using Coherent OTDR," in Journal of Lightwave Technology, vol. 27, no. 9, pp. 1142-1146, May1, 2009.

[11] Y. Lu, T. Zhu, L. Chen and X. Bao, "Distributed Vibration Sensor Based on Coherent Detection of Phase-OTDR," in *Journal of Lightwave Technology*, vol. 28, no. 22, pp. 3243-3249, Nov.15, 2010.

[12] K. Thyagarajan; Ajoy Ghatak, "Fiber Bragg Gratings," in Fiber Optic Essentials , , IEEE, 2007, pp.

[13] L. Thévenaz, S. Chin, J. Sancho and S. Sales, "Novel technique for distributed fibre sensing based on faint long gratings (FLOGs)," in *Proc. 23rd OFS*, Santander, Spain, June 2-6, 2014, p. 91576W.

[14] J. Hervás, D. Barrera, J. Madrigal and S. Sales, "Microwave photonics filtering interrogation technique under coherent regime for hot spot detection on cascaded FBG fiber," 2017 25th Optical Fiber Sensors Conference (OFS), Jeju, 2017, pp. 1-4.

[15] J. Hervás, D. Barrera, J. Madrigal and S. Sales, "Microwave Photonics Filtering Interrogation Technique Under Coherent Regime For Hot Spot Detection on a Weak FBGs Array," in *Journal of Lightwave Technology*, vol. 36, no. 4, pp. 1039-1045, 15 Feb.15, 2018.

[16] Stavros Iezekiel, "Microwave Photonic Signal Processing," in Microwave Photonics: Devices and Applications , , IEEE, 2004, pp.

[17] C. Wang and J. Yao, "A Nonuniformly Spaced Microwave Photonic Filter Using a Spatially Discrete Chirped FBG," in *IEEE Photonics Technology Letters*, vol. 25, no. 19, pp. 1889-1892, Oct.1, 2013.

[18] Y. Dai and J. Yao, "Nonuniformly Spaced Photonic Microwave Delay-Line Filters and Applications," in *IEEE Transactions on Microwave Theory and Techniques*, vol. 58, no. 11, pp. 3279-3289, Nov. 2010.

[19] A. L. Ricchiuti, J. Hervás, D. Barrera, S. Sales and J. Capmany, "Microwave Photonics Filtering Technique for Interrogating a Very-Weak Fiber Bragg Grating Cascade Sensor," in *IEEE Photon. J.*, vol. 6, no. 6, pp. 1-10, Dec. 2014.

[20] J. Ge and M. P. Fok, "Reconfigurable RF Multiband Filter With Widely Tunable Passbands Based on Cascaded Optical Interferometric Filters," in *Journal of Lightwave Technology*, vol. 36, no. 14, pp. 2933-2940, 15 July15, 2018.

[21] S. Liehr and K. Krebber, "Phase-OFDR for distributed disturbance measurement," in *Proc. of Sixth European Workshop on Optical Fibre Sensors*, Limerick, Ireland, May 31, 2016, p. 991624.

[22] J. Hervás, C. R. Fernández-Pousa, D. Barrera, D. Pastor, S. Sales and J. Capmany, "An Interrogation Technique of FBG Cascade Sensors Using Wavelength to Radio-Frequency Delay Mapping," in *J. Lightw. Technol.*, vol. 33, no. 11, pp. 2222-2227, June 2015.

[23] V. Hagemann, M. N. Trutzel, L. Staudigel, M. Rothhardt, H. -. Muller and O. Krumpholz, "Mechanical resistance of draw-tower-Bragg-grating sensors," in *Electronics Letters*, vol. 34, no. 2, pp. 211-212, 22 Jan. 1998.

[24] V. Hagemann, M. N. Trutzel, L. Staudigel, M. Rothhardt, H. -. Muller and O. Krumpholz, "Mechanical resistance of draw-tower-Bragg-grating sensors," in *Electronics Letters*, vol. 34, no. 2, pp. 211-212, 22 Jan. 1998.

[25] Y. Zheng, H. Yu, H. Guo, X. Li and D. Jiang, "Analysis of the Spectrum Distortions of Weak Fiber Bragg Gratings Fabricated In-Line on a Draw Tower by the Phase Mask Technique," in *Journal of Lightwave Technology*, vol. 33, no. 12, pp. 2670-2673, 15 June15, 2015.

Chapter 5

Phase modulation to intensity modulation conversion for high sensitivity FBG interrogation

5.1 Introduction

In the past years there has been an effort within the research community to develop what is known as high sensitivity sensors [1-5]. The goal of these sensors is to be able to measure small changes with a very good accuracy. The problem with this kind of application is the complexity of the alternatives proposed [2-9]. They are based on complex sensor configurations, complex interrogation systems or both.

In this chapter a high sensitivity interrogation technique for FBGs sensors is presented [10]. It is based on the phase modulation (PM) to intensity modulation (IM) conversion taking place in an FBG, so it is an intensity-based interrogation technique [11]. This kind of techniques show low complexity, fast-tracking speed and the ability to self-compensate power changes of the source [12-13].

In addition, this technique shows a great simplicity in the sensing device along with the interrogation technique and the system proposed. Furthermore, no post-processing is needed to extract the physical parameter measured by the FBG, so the interrogation speed could be extremely high.

5.2 Phase modulation to intensity modulation conversion

The phase modulation is characterized by the variation of the phase of the optical carrier following the modulating signal behavior. If the emitted light by an optical source is modulated in a phase-modulator by a microwave signal, expressed as $cos(\Omega_m t)$, the outgoing optical signal could be expressed as [10]:

$$E_{out} = E_1 e^{j\omega_1 t + j\beta \cos(\Omega_m t)} \tag{5.1}$$

where E_1 is the amplitude of the optical source, ω_1 is the angular frequency of the source and β is the modulation index, which can be formulated as $\pi V_m/V_\pi$

[14], where V_m is the amplitude of the modulating wave and V_π is the half-wave voltage of the modulator.

If small signal operation is taken into account, and the expansion of (5.1) based on the Bessel functions is performed, the output optical signal can be finally expressed as:

$$E_{out} = E_1 e^{j\omega_1 t}\left[J_0(\beta) + J_1(\beta)e^{j\Omega_m t} + J_{-1}(\beta)e^{-j\Omega_m t}\right] \quad (5.2)$$

where $J_i(\beta)$ with i=0,1 are the first kind Bessel functions.

Taking into account (5.2), it is straightforward to conclude that the optical field at the output of a phase-modulator develops equally spaced sidebands (thanks to small signal operation no higher order sidebands are present). Ideally, if this optical field is photodetected right after the modulation happens, no signal should be measured at the output, just a DC component. This is caused by the fact that both sidebands have the same amplitude but there is a π phase shift between them, which causes the cancellation when the optical wave is photodetected. But, any mismatch between the sidebands in terms of phase or power level would lead to an increment in the detected power at the output (the cancellation is no longer complete), creating this way a PM to IM conversion [15-16].

5.3 Principle of operation

The interrogation technique is based on the PM to IM conversion taking place in an FBG [17-18]. As it has been stated in the previous section, if a phase-modulated signal is driven directly towards the photodetector no microwave signal would be detected at the output due to the orthogonality of the sidebands. However, any mismatch either in power or phase between the two sidebands (small signal operation) would cause the appearance of microwave signals at the output since the cancellation between the sidebands is no longer complete (one sideband is more powerful than the other or the difference in phase between the two sidebands is no longer π). This constitutes a conversion of a PM into an IM and this is the principle that is used in order to extract the sensing information of a given FBG.

Let's assume that the system of Fig. 5.1 is set up. It consists of a tunable laser (TLS), a phase-modulator (PM), a local oscillator (LO) a circulator, an FBGs array, a photodetector (PD), a microwave amplifier and a signal analyzer (SA).

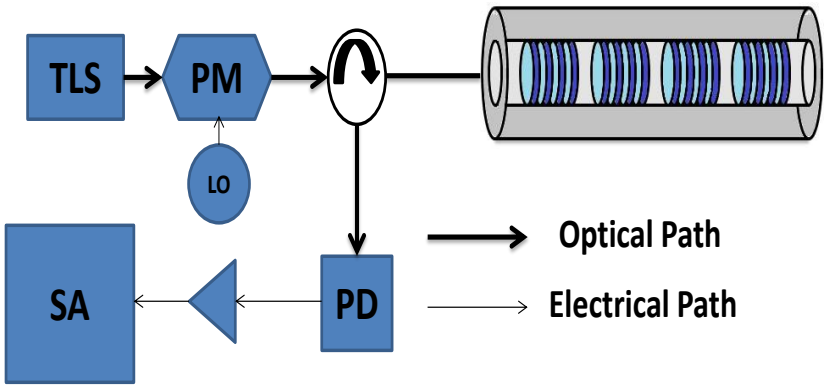

Fig.5.1. Schematic view of the system used to develop the interrogation technique.

So, the light coming from the laser is modulated by a microwave tone coming from a local oscillator at the phase-modulator. This phase-modulated light enters the FBG array where it is reflected and finally the reflected beam is headed to the photodetector to finally measure the power of the modulating tone at the output using a signal analyzer.

If no FBGs array is used in the system, no signal would be acquired at the output since both sidebands are orthogonal between them and no changes have been produced to them. Nevertheless, if this optical wave is filtered by an FBG, phase and power changes can occur, and therefore some power could be detected at the output. This is the situation pictured at Fig. 5.2.

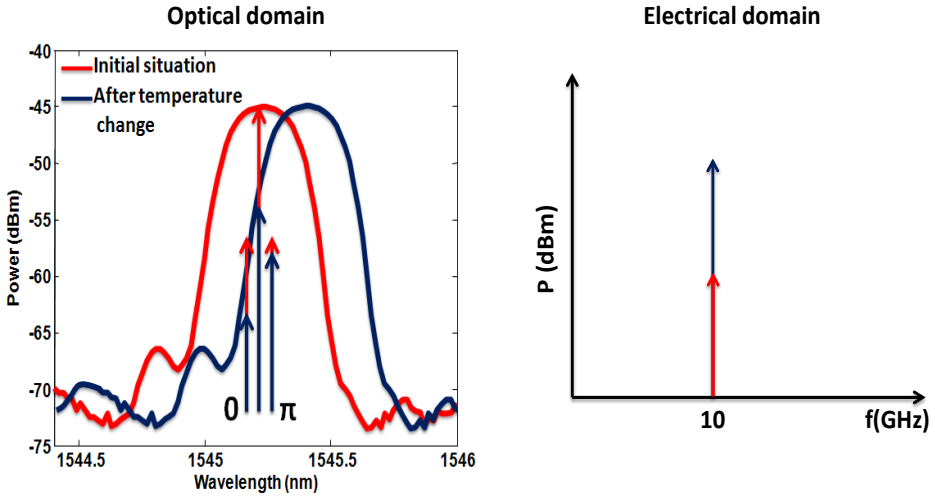

Fig. 5.2. Principle of operation

If the laser is emitting at the Bragg wavelength of the FBG, no mismatch should be produced between the two sidebands (FBG symmetry and flat delay profile of the FBG are being assumed). This is the situation pictured by the red trace. However, if the FBG suffers a Bragg wavelength change (blue trace), the two sidebands are no longer equal in power, the cancellation is no longer complete, so the power at the output is no longer zero. As this change of the output microwave power depends directly on the mismatch between both sidebands and this mismatch depends on the movement of the Bragg wavelength of the FBG, this output power can be used to retrieve the environmental conditions (temperature or strain) that are being experienced by the sensor.

The spectrum of the real FBGs that were going to be used in the experimental part of the interrogation technique development was used in order to simulate the behavior of the interrogation technique in a real scenario. The array consisted of 6 different FBGs. There were uniform and apodized FBGs. The spectrum of all the FBGs can be seen in Fig. 5.3.

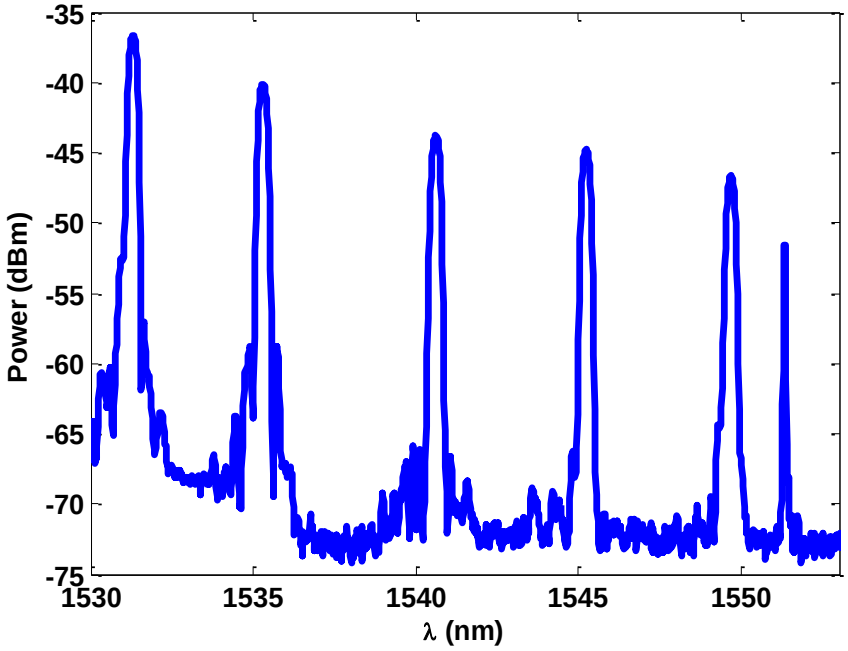

Fig. 5.3. Spectrum of the FBGs of the array used for the experimental measurements

The FBG at 1,545.2 nm was selected to run some simulations in order to study the interrogation technique in an ideal way. The spectrum of this FBG can be seen in Fig. 5.4.

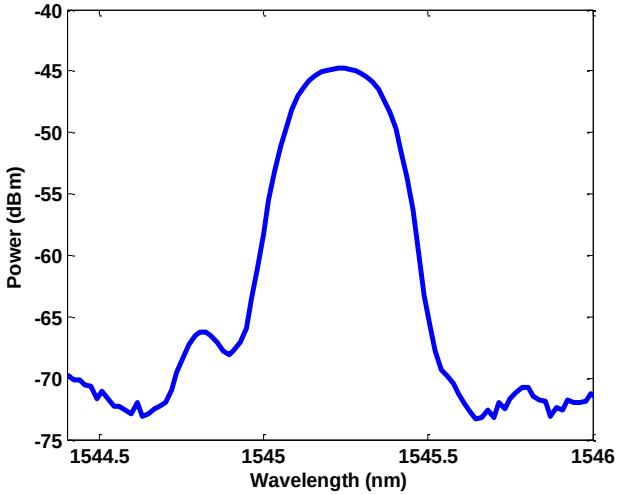

Fig. 5.4. Spectrum of the FBG used for the simulation set

The goal of this simulation set was to relate the Bragg wavelength change suffered by the FBG with the variation of the radiofrequency (RF) power measured by the signal analyzer at the output. To do so, first step is to select the RF signal that is going to modulate the light emitted by the tunable laser. In this case, the RF signal chosen is a pure RF tone. The selected frequency for the tone was 10 GHz.

Second step was to measure the real spectrum of the FBG showed in Fig. 5.4. To do so, an optical spectrum analyzer was used. The resolution of the apparatus was set to the smallest possible value, 1 pm.

The simulation starts with the laser centered at the Bragg wavelength of the FBG and then the Bragg wavelength is shifted towards longer and shorter wavelengths with a step of 1 pm. In each one of the situations, the photodetected power at the output caused by the mismatch between both sidebands is calculated. Having a 10 GHz modulating wave means that the distance between the two sidebands is around 160 pm (125 GHz → 1 nm, 10 GHz → 80 pm). Assuming that no mismatch comes from any of the equipment used in the system, the mismatch can only be caused by the FBG spectrum differences. In order to calculate these created differences, the points that are 80pm away at both sides of the carrier location need to be subtracted in order to calculate the difference in terms of power that is going to be created by the FBG. Ideally, when the laser is emitting at the Bragg wavelength no power should be detected at the output since the same power is being reflected at both sidebands (FBG is symmetric). Nevertheless, as the spectrum of a real FBG is being used for the simulation, this hypothesis is not true. Even when the laser is totally centered, some power can be read at the signal analyzer.

The formula used in order to calculate the difference in power between both sidebands, and therefore, the power of the 10 GHz tone that is being detected by the signal analyzer, is this one:

$$P_{n-n'}(dB) = 10\log\left(r_{n+80} - r_{n-80}\right)^2 \quad (5.3)$$

where P is the measured RF tone power, n is the wavelength position of the laser, n' is the Bragg wavelength of the FBG and *r* is the reflectivity of the FBG. Therefore (n-n') represents the detuning (in pm) of the laser emitting wavelength with respect to the Bragg wavelength of the FBG (n-n'=0 is the initial situation in which the laser is emitting at the Bragg wavelength) and n±80 represents the position of both sidebands. The difference between reflectivities must be squared due to the fact that the photodetector provides electrical current at the output but the signal analyzer measures power.

In order to calculate the measured power at the output with respect to the wavelength difference between laser and FBG, (5.3) is applied to the spectrum of the FBG captured that is shown in Fig. 5.4. The result calculated using (5.3) is shown in Fig. 5.5.

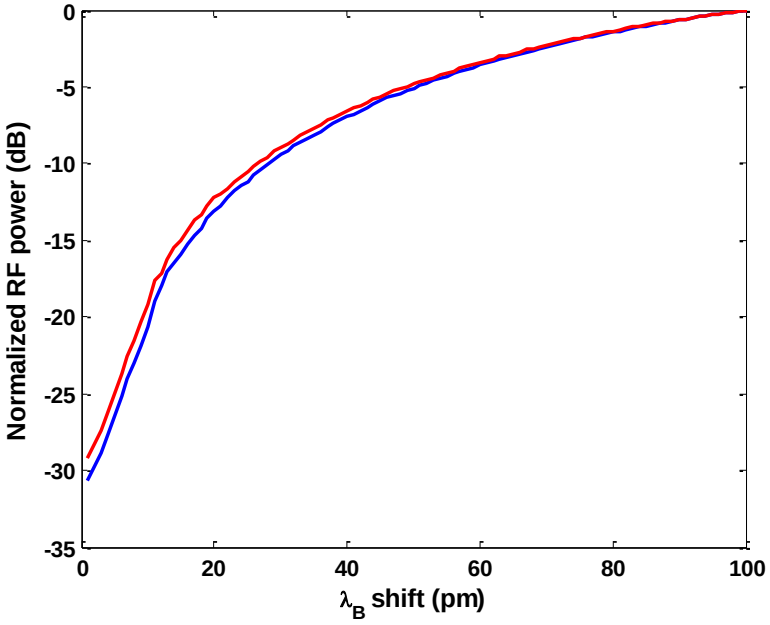

Fig. 5.5. Power distribution calculated in the simulation using (5.3) for a red (red trace) and a blue (blue trace) shift of the Bragg wavelength of the FBG

As can be seen in Fig. 5.5 there is a linear change in the detected power for Bragg wavelength movements up to around 10 pm. From that point on the

behavior of the curve changes to quadratic, losing this way sensitivity and resolution. But in the first 10 pm of measurement range, the sensitivity is 1 dB/pm (≈10 dB/ºC). This makes very easy for this technique to measure changes in the Bragg wavelength in the sub-pm scale (resolution below 0.1 ºC with high accuracy).

The linear range is not very large but the sensitivity is quite high. This kind of interrogation technique could be suitable for biomedical application in which a huge measurement range is not always needed and a high sensitivity and accuracy is desirable [19]. Anyway, to increase the linear range of the measurement the tunable laser can be swept in order to follow the FBG movement or ultra-short FBGs with wide spectrum could be used [20].

Ideally, the variation in power measured at the output comes uniquely from the difference in power between both sidebands. But in a real scenario, there are some other aspects that must be taken into account since these can lead to measurement errors or to a resolution change.

5.4 FBG phase and dispersion

As it has been explained in previous sections of this chapter, the filtering effect of the FBG is the principle that leads to a conversion from PM to IM and therefore the power reading at the signal analyzer can be used to measure the difference between the laser emitting wavelength and the Bragg wavelength of the FBG, being possible this way to calculate the difference in temperature or strain that is being experienced by the FBG at that particular moment.

However, any other effect that creates a difference either in power or in phase between both sidebands is going to change the power measured by the signal analyzer, increasing this way the amount of error of the output data.

With regards to power differences between the two sidebands that are not created by the filtering effect, these differences can be created by the devices of the system. The modulator and photodetector responses can change with time due to temperature or bias change. Nevertheless, these changes would affect both sidebands in the same proportion so no distortion is expected from these devices. Furthermore, power differences in the laser emission are self compensated since it affects both sidebands also.

Regarding phase changes that can affect both sidebands unilaterally, there are two components that must be addressed: the phase profile of the FBG and the chromatic dispersion inside the system.

In relation to the phase profile of the FBG, a measurement of this phase was carried out in the lab. To do so, the electrical phase of the FBG was measured with a vector network analyzer (VNA). A 2 nm sweep around the Bragg

wavelength of the FBG was performed using a tunable laser. The modulating frequency was set to 100 MHz. The electrical power received and the electrical phase was measured for every wavelength of the sweep. To calculate the optical phase of the grating, a conversion must be done from the electrical phase. The first step is to calculate the electrical delay from the electrical phase. This can be done using this formula:

$$\tau_{opt} = \frac{\phi_{RF}}{2\pi f_{RF}} \tag{5.4}$$

Once the optical delay has been calculated, the optical phase can be retrieved using:

$$\tau = \frac{d\phi}{d\omega} \tag{5.5}$$

So the phase profile can be retrieved through integration of the optical delay calculated using (5.4). The perfect phase for this application is a linear phase, so no matter how much the FBG movement has been, the difference in phase between the two sidebands is kept constant. To have a linear phase means that the difference between consecutive points in the phase profile is constant, in other words, the optical delay is flat inside the FBG spectrum. These differences were calculated, through subtraction of consecutive points, and the results are shown in Fig. 5.6, along with the power values retrieved by the VNA. As can be seen in Fig. 5.6 the phase differences are constant inside the bandwidth of the FBG (linear profile of the phase).

With regards to the chromatic dispersion effect, as long as the calibration and the real scenario are the same, dispersion can affect the sensitivity and resolution of the interrogation technique but it would still be able to retrieve the temperature change suffered by the FBG. Anyway, the difference in dispersion between both sidebands would be in this case around 0.0064 ps/(nm·km) (calculated using the dispersion profile of the fiber measured in chapter 2 for two different wavelengths around 1,545.2 nm and a difference of 160 pm between them) and if the effect of dispersion is too high due to the fact that the fiber link used is too long, the effect can be easily eliminated using dispersion compensation techniques.

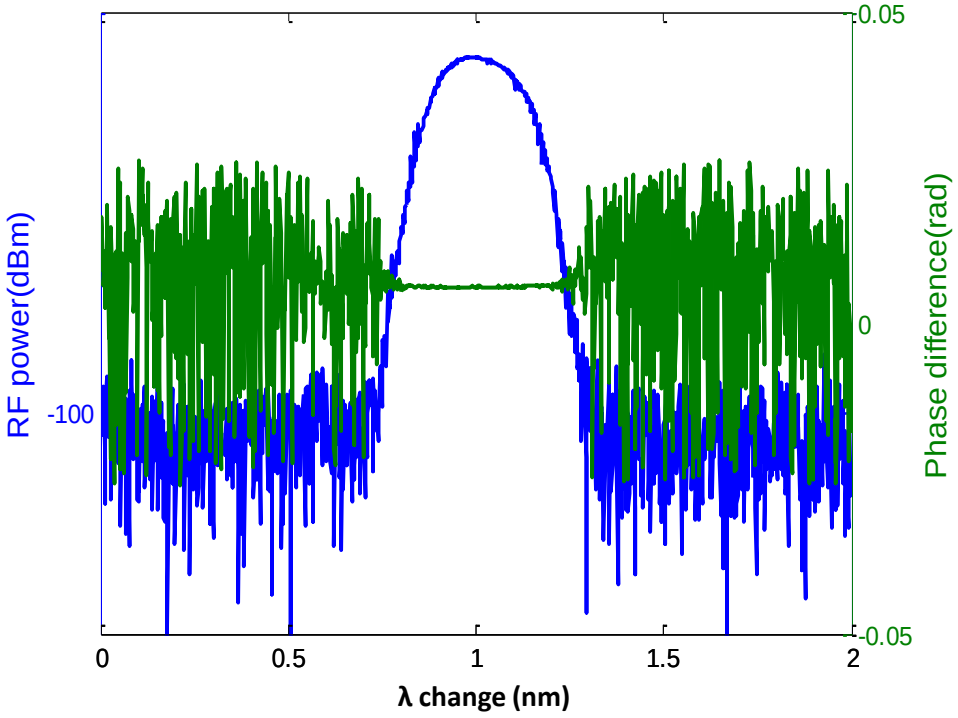

Fig. 5.6. Electrical magnitude recorded (peak value -30dBm) and phase differences calculated with the electrical phase conversion

5.5 Effect of the FBG and RF frequency

In this interrogation technique there are mainly two variables that can be controlled. One is the modulating frequency and the other is the characteristics of the FBG (bandwidth, apodization, etc).

With regards to the characteristics of the FBG a simulation set was performed in order to study the effect of the bandwidth of the FBG in the sensitivity of the technique. To perform this simulation, four different FBGs were simulated. They all had the same peak reflectivity and the only difference was the bandwidth. In terms of apodization, gaussian shaping of the refractive index profile was chosen. The reason why this is the apodization chosen is because in order to have a good linearity in the measurement, a parabolic shaped FBG is desired for the measurement. Another reason to use gaussian apodization in the FBG is the linearity of the phase [21]. Uniform FBGs show a not so linear phase profile which can lead to non-linearities in the power vs Bragg wavelength movement curve. The spectra of the FBGs used in the simulation are shown in Fig. 5.7.

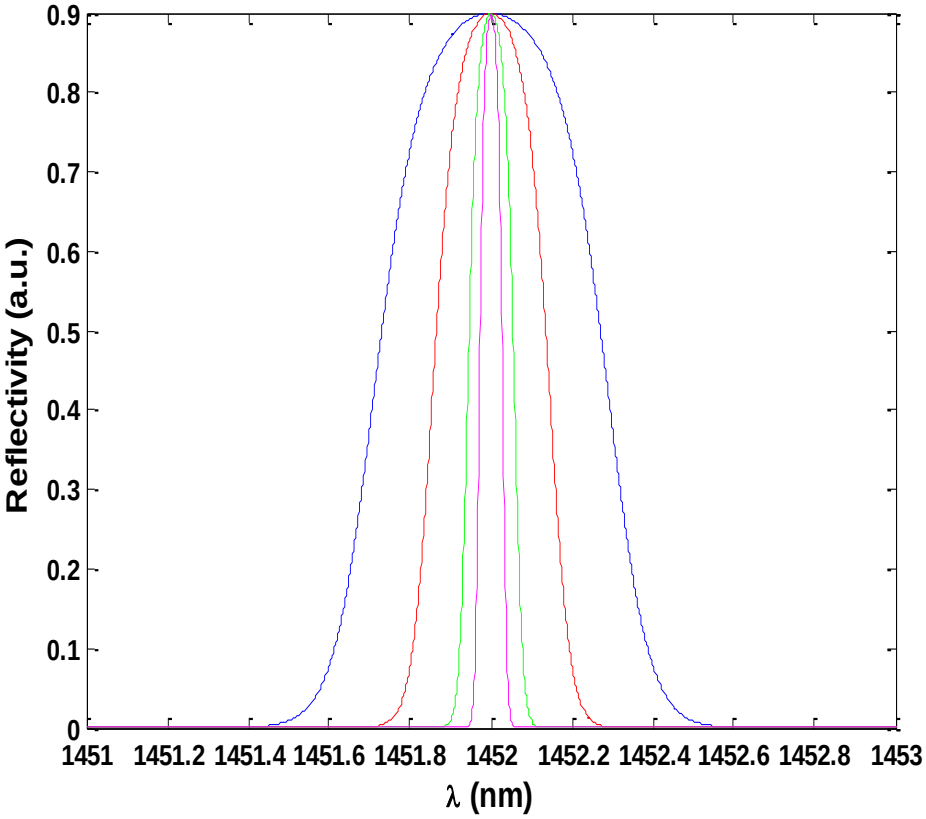

Fig. 5.7. Linear spectra of the simulated FBGs

The Full Width Half Maximum (B_{-3dB}) of the simulated FBGs were 565, 283, 113 and 57 pm respectively. The peak reflectivity was set to 90%. The modulating frequency for this measurement was set to 1GHz.

Fig. 5.8 shows the result of the simulation carried out. The sensitivity is higher and the linear range is wider for the narrower FBGs but the range with positive change is smaller compared to wider FBGs. This seems quite reasonable since narrower FBGs have a sharper spectrum but at the same time as the spectrum is narrower the measurement range is shorter.

The other parameter studied was the effect of the modulating frequency. To study its effect, the procedure explained in Section 5.3 of this chapter was applied to the spectrum of the wider FBG shown in Fig. 5.7 (the blue one). The studied frequencies were 10, 5, 2.5 and 1 GHz. When (5.3) is applied to this spectrum for the different frequencies the same result is achieved when the calculations are normalized. The only difference between the calculations for

the different frequencies is the starting value of the power distribution. The 1pm movement power level for 1 GHz is around -60 dBm while it is -45 dBm for a 10 GHz frequency. This phenomena is created by the perfect symmetry of the simulated FBGs. Therefore the only difference between different frequencies is the signal to noise ratio (SNR) of the measurement. The higher the frequency,

the higher the SNR while keeping the same sensitivity and resolution. The same procedure was applied to the real FBG spectrum shown in Fig. 5.4 in order to study the effect of the non-symmetry of the spectrum. The results can be seen in Fig. 5.9.

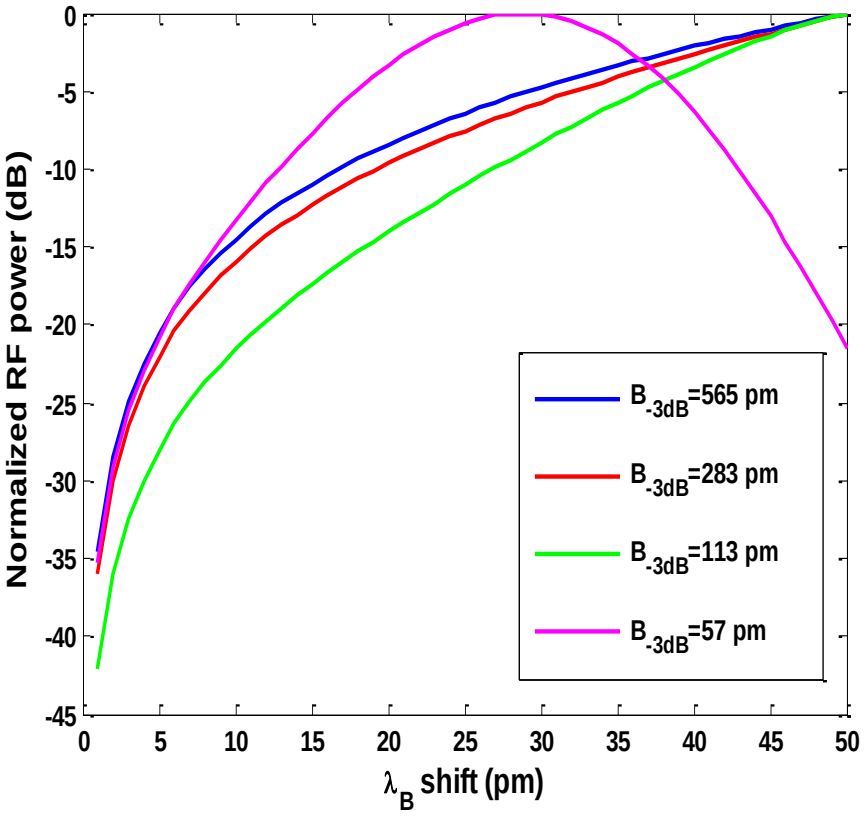

Fig. 5.8. Power variation versus λ_B change for different FWHM (simulation)

The four traces showed in Fig. 5.9 are quite similar although it can be seen that the lower frequencies are more affected by the FBG asymmetry (saw-tooth appearance). As in the previous simulation, the SNR is higher for higher frequencies, despite the fact that the sensitivity and linear range are practically the same for all the frequencies studied.

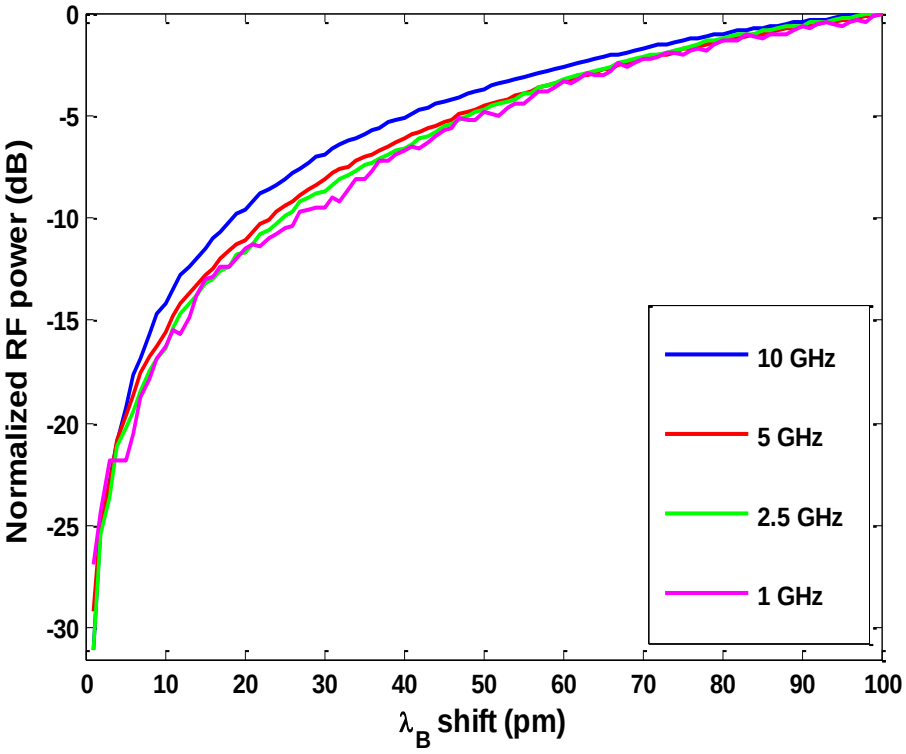

Fig. 5.9. Power distribution for different modulating frequencies

Finally, if both parameters (frequency and FBG bandwidth) are taken to the extreme (narrow bandwidth and high frequency) the best result is shown. Fig. 5.10 shows the result of interrogating the narrowest FBG of Fig. 5.7 with a frequency of 10 GHz.

It can be observed that the variation is nigh-on linear for the first 50 pm of change and the sensitivity is around 2 dB/pm. The only problem in this case would be that the starting power detected would be too low, <100 dB for normalized power (Fig. 5.10), so in the real scenario the laser should start emitting in the middle of the linear slope in order to have a suitable SNR or equipment with a very high sensitivity must be used in order to detect such a low initial power level.

This final result opens the door to FBG tailoring in order to create extremely sensitive sensors with an improved linear range [22].

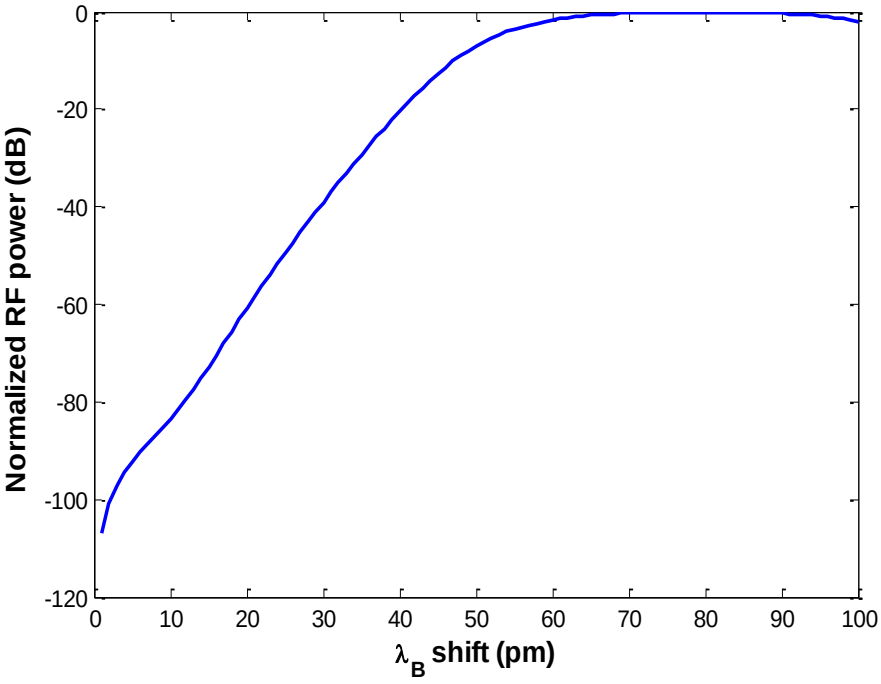

Fig. 5.10. Power distribution of the narrowest FBG interrogated by a modulating frequency of 10GHz

5.6 Experimental results

The system depicted in Fig. 5.1 was set up in the lab in order to test the interrogation technique in a real scenario. The tunable laser was set to emit at 1,545.22 nm, the Bragg wavelength of the FBG (Fig. 5.4). The V_π of the modulator is 11 V so the peak amplitude of the RF modulating signal was set to 0.4 V in order to have a low modulation index, β, close to 0.1 to suppress higher-order harmonics ($J_n \approx 0$ for $n>1$, see table 5.1) [23].

β	$J_0(\beta)$	$J_1(\beta)$	$J_2(\beta)$	$J_3(\beta)$
0	1	0	0	0
0.1	0.9975	0.0466	0.0012	0
0.2	0.99	0.0995	0.005	0.0002
0.3	0.9776	0.1483	0.0112	0.0006
0.4	0.9604	0.196	0.0197	0.0013

Table 5.1. Bessel identities for different β values

A local RF oscillator generated the 10GHz tone that phase-modulated the light coming from the tunable laser. Then, the modulated light was directed into the FBG array where it was back reflected to finally be photodetected and analyzed in the signal analyzer (Agilent MXA Signal Analyzer). Here the 10 GHz tone power was monitored in order to retrieve the temperature change experienced by the FBG.

The interrogated FBG was 1cm long and the refractive index profile was apodized using a Gaussian window in order to reduce sidelobes and to linearize the phase profile. The -3 dB bandwidth (FWHM) was 0.3 nm. This FBG was placed on a peltier cooler in order to produce the temperature change. The temperature change was produced in steps of 0.2 ºC (2 pm of Bragg wavelength change taking into account the standard temperature coefficient of FBGs which is around 10 pm/ºC). Fig. 5.11 shows the normalized power distribution with regards to the Bragg wavelength change for a blue shift of up to 100 pm.

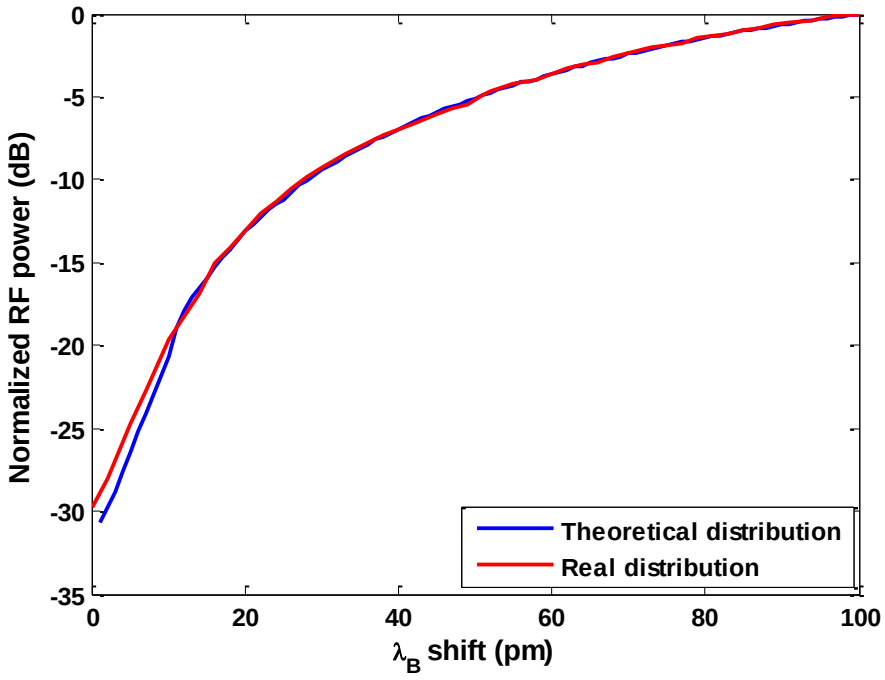

Fig. 5.11. Photodetected (theoretical -blue trace- and real -red trace-) power of the RF tone at 10 GHz for a blue shift of the Bragg wavelength up to 100pm

The power variation related to the movement of the FBG shown in Fig. 5.11 is almost the same compared to the theoretical result predicted by simulations. The slight difference happens in the beginning of the linear range and is probably caused by three main factors. First factor is the RF amplifier that is being used

to amplify the signal prior to analysis done by the signal analyzer. Second factor is noise. For small movements of the FBG, the similarity between both sidebands is still big, so the detected power is small (around -50 dBm) what causes a larger noise effect created by a smaller SNR. Finally, the third factor is an initial small misalignment between the laser and the Bragg wavelength of the FBG. The alignment of the laser and the FBG was performed using an optical spectrum analyzer (OSA) with a 1 pm resolution which is not so good for this particular procedure. For a 2 pm change of the Bragg wavelength, the difference between the theoretical and the experimental result is 1.5 dB, so the misalignment, taking into account the other factors, should be around 1 pm.

However, the power level of the 10 GHz tone still varies with the Bragg wavelength which provides the ability to interrogate such a sensor with a very high sensitivity as it is shown in Fig. 5.11. In Fig. 5.12 are shown the traces acquired from the signal analyzer.

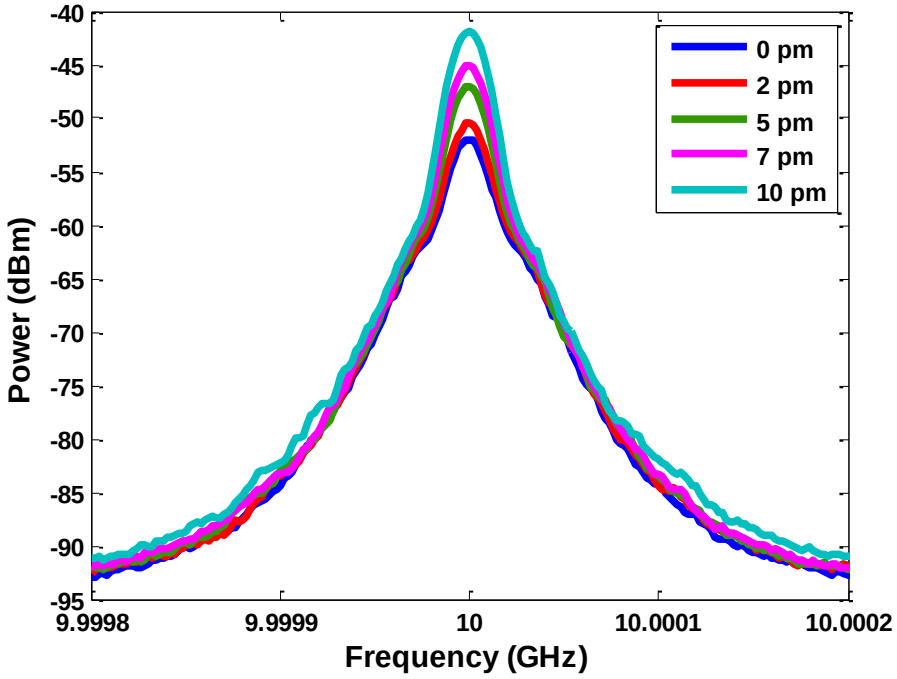

Fig. 5.12. Signal analyzer acquired traces for different Bragg wavelength movements

The peak power of these traces was used to found the curve shown in Fig. 5.11. The slope of the curve (Fig. 5.11) still shows a sensitivity of 1 dB/pm as in the theoretical result. The linear range is shown in Fig. 5.13. In this zoom view of this section of the curve it can be seen that the power values are almost perfectly linearly fitted, just like in the theoretical expected result.

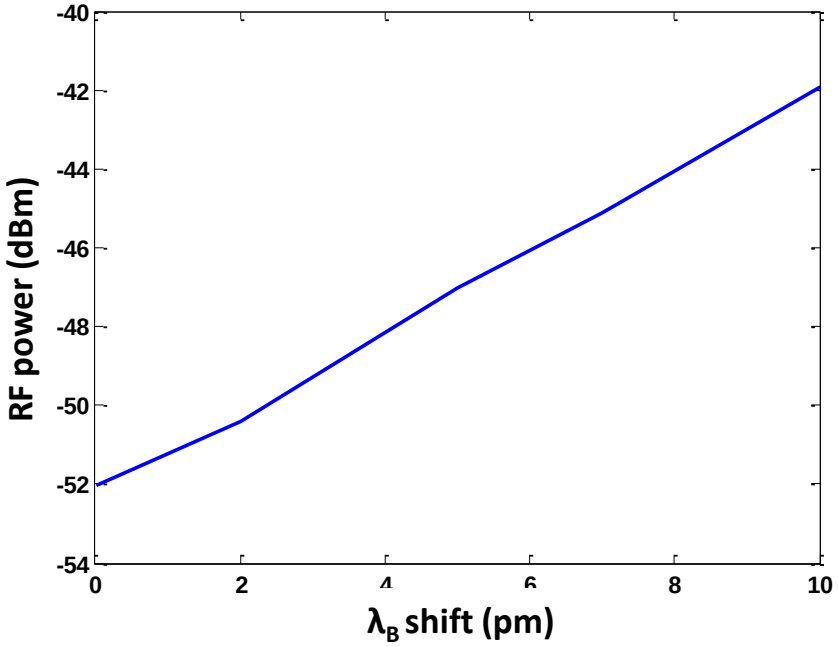

Fig. 5.13. Zoom view of the linear range of the curve shown in Fig. 11 (these data are not normalized)

This experimental measurements prove that this interrogation technique is a suitable technique to retrieve small Bragg wavelength changes with high sensitivity and accuracy.

5.7 Conclusions

In this chapter the interrogation technique based on the PM to IM conversion that takes place in an FBG has been presented. The orthogonality of both modulation sidebands is altered by the FBG movement, movement that can be retrieved using the power level of the photodetected 10 GHz tone used to phase-modulate the light coming from a tunable laser. This technique shows a very high sensitivity, 1 dB/pm.

A tunable laser emitting at the Brag wavelength of a given FBG is phase-modulated by a microwave tone coming from a local oscillator. The modulation index is kept close to 0.1 in order to avoid the appearance of higher harmonics ($J_n \approx 0$ for $n>1$, see table 1). This phase-modulated wave is then reflected by the FBG. Initially, the level of power detected at the output is quite small due to the orthogonality of both sidebands and the similarity in the power level of both sidebands as well. When the FBG suffers a temperature or a strain change, its Bragg wavelength changes causing a mismatch between both sidebands in terms

of power. This misalignment increases the power level of the MW tone detected at the output. This change in the power at the output can be used to measure the Bragg wavelength change with an extremely high sensitivity and accuracy. The high sensitivity of this technique makes it easy to measure Bragg wavelength changes smaller than 1 pm with high precision.

The MW power to Bragg wavelength movement relationship shows a linear range of around 10 pm. After that, the distribution shift to a quadratic behavior, which represents a reduction in sensitivity and resolution. Anyway, the tunable laser can be tuned in order to follow the FBG changes in order to keep the sensitivity in its higher values.

Compared to other techniques that also show a high sensitivity, this technique is less complex and no post-processing must be used to extract the sensing information since the raw power measurement can be directly related to the Bragg wavelength status. This last feature provides the ability to monitor the FBG condition with a fast tracking speed.

References

[1] X. Wen *et al*., "High-Sensitive Microdisplacement Sensor Based on Fiber Mach–Zehnder Interferometer," in *IEEE Photonics Technology Letters*, vol. 26, no. 23, pp. 2395-2398, 1 Dec.1, 2014.

[2] Y. H. Kim, M. J. Kim, B. S. Rho, M. Park, J. Jang and B. H. Lee, "Ultra Sensitive Fiber-Optic Hydrogen Sensor Based on High Order Cladding Mode," in *IEEE Sensors Journal*, vol. 11, no. 6, pp. 1423-1426, June 2011.

[3] L. Li *et al*., "Ultrahigh Sensitive Temperature Sensor Based on Fabry–Pérot Interference Assisted by a Graphene Diaphragm," in *IEEE Sensors Journal*, vol. 15, no. 1, pp. 505-509, Jan. 2015.

[4] H. Chen, S. Li, J. Li, Y. Han and Y. Wu, "High Sensitivity of Temperature Sensor Based on Ultracompact Photonics Crystal Fibers," in *IEEE Photonics Journal*, vol. 6, no. 6, pp. 1-6, Dec. 2014, Art no. 6803006.

[5] J. Zhang *et al*., "Highly-Sensitive Temperature Sensor Using a Hi-Bi Fiber Tip Probe," in *IEEE Sensors Journal*, vol. 12, no. 6, pp. 2077-2080, June 2012.

[6] Y. Geng, X. Li, X. Tan, Y. Deng and Y. Yu, "High-Sensitivity Mach–Zehnder Interferometric Temperature Fiber Sensor Based on a Waist-Enlarged Fusion Bitaper," in *IEEE Sensors Journal*, vol. 11, no. 11, pp. 2891-2894, Nov. 2011.

[7] M. Yang, K. Yang, J. Tang, C. Li and F. Shang, "High-sensitivity quasi-distributed temperature sensors based on weak FBGs Fabry-Perot structure with

metal coating," *2017 16th International Conference on Optical Communications and Networks (ICOCN)*, Wuzhen, 2017, pp. 1-3.

[8] F. Gu, H. Yu, W. Fang and L. Tong, "Nanoimprinted Polymer Micro/Nanofiber Bragg Gratings for High-Sensitivity Strain Sensing," in *IEEE Photonics Technology Letters*, vol. 25, no. 1, pp. 22-24, Jan.1, 2013.

[9] Y. Zhang, L. Xue, T. Wang, L. Yang, B. Zhu and Q. Zhang, "High Performance Temperature Sensing of Single Mode-Multimode-Single Mode Fiber With Thermo-Optic Polymer as Cladding of Multimode Fiber Segment," in *IEEE Sensors Journal*, vol. 14, no. 4, pp. 1143-1147, April 2014.

[10] J. Hervás, D. Barrera, J. Madrigal and S. Sales, "Phase modulation to intensity modulation conversion for sensitive FBG sensor interrogation," *2017 25th Optical Fiber Sensors Conference (OFS)*, Jeju, 2017, pp. 1-4.

[11] R. Cheng, L. Xia, Y. Ran, J. Rohollahnejad, J. Zhou and Y. Wen, "Interrogation of Ultrashort Bragg Grating Sensors Using Shifted Optical Gaussian Filters," in IEEE Phot. Technol. Lett., vol. 27, no. 17, pp. 1833-1836, Sept. 2015.

[12] C. Vazquez, J. Montalvo, D. S. Montero and J. M. S. Pena, "Self-Referencing Fiber-Optic Intensity Sensors Using Ring Resonators and Fiber Bragg Gratings," in *IEEE Photonics Technology Letters*, vol. 18, no. 22, pp. 2374-2376, Nov.15, 2006.

[13] A. Wang, H. Xiao, J. Wang, Z. Wang, W. Zhao and R. G. May, "Self-calibrated interferometric-intensity-based optical fiber sensors," in *Journal of Lightwave Technology*, vol. 19, no. 10, pp. 1495-1501, Oct. 2001.

[14] H. Chi, X. Zou and J. Yao, "Analytical Models for Phase-Modulation-Based Microwave Photonic Systems With Phase Modulation to Intensity Modulation Conversion Using a Dispersive Device," in *Journal of Lightwave Technology*, vol. 27, no. 5, pp. 511-521, March1, 2009.

[15] J. Li, Y. Zhang, S. Yu and W. Gu, "Optical Sideband Processing Approach for Highly Linear Phase-Modulation/Direct-Detection Microwave Photonics Link," in *IEEE Photonics Journal*, vol. 6, no. 5, pp. 1-10, Oct. 2014, Art no. 5501110.

[16] Jun Wang, Fei Zeng and Jianping Yao, "All-optical microwave bandpass filter with negative coefficients based on PM-IM conversion," in *IEEE Photonics Technology Letters*, vol. 17, no. 10, pp. 2176-2178, Oct. 2005.

[17] J. Marti, F. Ramos, V. Polo, J. M. Fuster and J. L. Corral, "Millimetre-wave generation and harmonic upconversion through PM-IM conversion in

chirped fibre gratings," in *Electronics Letters*, vol. 35, no. 15, pp. 1265-1266, 22 July 1999.

[18] W. Li and J. Yao, "A Wideband Frequency Tunable Optoelectronic Oscillator Incorporating a Tunable Microwave Photonic Filter Based on Phase-Modulation to Intensity-Modulation Conversion Using a Phase-Shifted Fiber Bragg Grating," in *IEEE Transactions on Microwave Theory and Techniques*, vol. 60, no. 6, pp. 1735-1742, June 2012.

[19] Y. Rao, D. J. Webb, D. A. Jackson, L. Zhang and I. Bennion, "In-fiber Bragg-grating temperature sensor system for medical applications," in *J. Lightw. Technol.*, vol. 15, no. 5, pp. 779-785, May 1997.

[20] R. Cheng, L. Xia, Y. Ran, J. Rohollahnejad, J. Zhou and Y. Wen, "Interrogation of Ultrashort Bragg Grating Sensors Using Shifted Optical Gaussian Filters," in IEEE Phot. Technol. Lett., vol. 27, no. 17, pp. 1833-1836, Sept. 2015.

[21] A. Carballar and M. A. Muriel, "Phase reconstruction from reflectivity in fiber Bragg gratings," in *Journal of Lightwave Technology*, vol. 15, no. 8, pp. 1314-1322, Aug. 1997.

[22] B. A. L. Gwandu and W. Zhang, "Tailoring the temperature responsivity of fibre Bragg gratings [temperature/strain sensors]," *SENSORS, 2004 IEEE*, Vienna, 2004, pp. 1430-1433 vol.3.

[23] H. B. Dwight, "A five-figure table of the bessel function $I_n(x)$," in *Electrical Engineering*, vol. 60, no. 3, pp. 135-136, March 1941.

Chapter 6

High-voltage sensing using poled fibers with FBGs

6.1 Introduction

Silica fiber possesses many ideal properties that turn it into a perfect transmission medium and into a perfect candidate to fabricate passive devices, like couplers [1-2]. However, it is intrinsically limited for the fabrication of active devices [3]. Theoretically, the electro-optic coefficient of the fiber is zero. This makes almost impossible the fabrication of devices on which this effect is used.

Nevertheless, this kind of active device would be of such an importance due to the intrinsic features of the standard fiber and the easiness of integration with fiber links. This is the reason why so much effort has been driven from the research community towards this objective in the past decades [4].

One of the trends the research community has been following is the poling of fibers [5-10]. This technique can induce a non-zero electro-optic coefficient in the fiber, which could be very useful in applications such as modulation [11] or second harmonic generation [12].

Traditionally this effect was induce by heating the fiber along with the application of a strong electric field. This procedure could enlarged dramatically the electro-optic coefficient of the standard fiber. It is what is called thermo-poling [13].

A new technique was developed afterwards, known as optical poling [14]. Optical excitation is known to free charges from silica fibers. In this kind of technique infrared (1.06 μm), its second harmonic, blue light or UV light [14] are used to create an effective $\chi^{(2)}$. One common believe about optical poling is that the induced effect is weaker compared to thermal induced effect. There was a promise that with UV poling a high nonlinear coefficient could be achieved, but its materialization failed, what caused the temporal abandonment of the optical poling technique. However, it has been boosted again in the past few years due to some unique characteristics of this particular technique compared to thermo-poling (periodical poling [15] or controlled poling removal [16]).

In this chapter, it is presented two different techniques on how optically-poled fibers with FBGs inscribed in them can be used as electric field sensors. Thanks to the physical features of the optical fiber this kind of sensors show some

intrinsic advantages compared to any other electric based sensor (distortion of the electric field being measured [17] for example).

6.2 Poling fibers

There are mainly two techniques to create a poled fiber: thermal poling [13] and optical-poling [14]. On one hand, in the thermo-poling technique, high temperature is used in order to increase the movement of charges. On the other hand, in the optical-poling technique, strong beams are used to free charges in silica fibers to create the poling effect.

The first step to pole a fiber is the fabrication of the component. The fiber used for poling have normally two holes around the center of the fiber [18] that will be filled with metal in order to create the electrodes that allow to apply an electric field that will be frozen inside the fiber after poling has taken place. Depending on the poling method that is used, the position of the holes may depend. For thermal poling, as the movement of charges happens between both electrodes, the core must be close to one of the holes in order to be inside of one of the regions affected by the electric field (the center region between both electrodes has zero charge) [19]. On the contrary, as in the optical poling technique the movement of charges only happens in the core, it can be totally centered between both electrodes (it can be still used the non-centered core fiber, but this arrangement increases the transmission losses). This two configurations can be seen in Fig. 6.1.

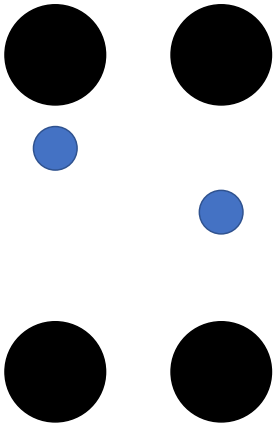

Fig. 6.1. Situation of the holes (black dots) in relation to the core (blue dot) of the fiber for thermal poling (left) and for optical poling (right)

These fibers are normally germanium-doped fibers in order to increase the number of charges available in the fiber. Once the fiber has been fabricated, the poling process starts. To do so, the application of a strong electric field must be performed. In order to apply this electric field, metallic electrodes must be

inserted in the fiber somehow. Different methods have been used to create these electrodes. Some of the techniques used are manual insertion of the electrodes or filling the holes with liquid metal that will freeze inside [20]. On the one

hand, manual insertion has the advantage of being very easy to connect these electrodes to the voltage source but it shows some restrictions in the length of the fiber and it is a quite unreliable process. On the other hand, filling the holes with liquid metal is not so restrictive but the process to connect afterwards these electrodes to the voltage source requires a step by step process that can limit the fiber performance in terms of fiber strength. In recent years, a new technique based on electrostatic induction has been developed in order to overcome some of the limitations of the above mentioned techniques [21].

The fibers used in this chapter were fibers filled with liquid metal. The filling process was performed using an oven and a pressure chamber. The filling process is a step by step process and it is as follows:

1. First step is to remove the coating of the fiber tips. This is done in order to insert these fiber tips in the liquid metal that will be pumped inside the fiber through the holes.
2. The fiber tips that have been uncoated are inserted in a special screw. The uncoated fiber tips emerge from the screw tip to be inserted in the liquid metal afterwards. This screw will be screw in the pressure chamber in order to pump the metal inside the fiber. This is showed in the next figure.

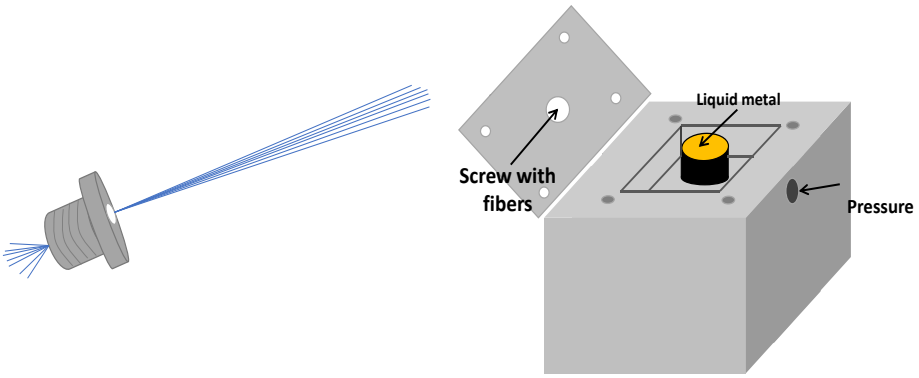

Fig. 6.2. Left: Fibers already inserted in the screw. Right: Pressure chamber.

3. The pressure chamber, with the metal already inside, is inserted inside the oven in order to heat it. The metal used for this procedure was an alloy of bismuth and tin. The objective temperature of the oven was 150 ºC (melting point around 138 ºC)..
4. Once the metal is liquid the screw with the fiber is screwed in the pressure chamber and everything is put together again inside the chamber at 150 ºC. A section of the fiber is kept out of the oven thanks to a hole in the upper part of the oven. This frontier point (oven and free space border) of the fiber is the point up to which the metal is going to be pumped (the fiber section that is out of the oven is at room temperature, so the metal solidifies when it reaches that frontier, setting the limit for the metal injection).

5. After a certain amount of time, the pressure inside the chamber where the fiber is inserted inside the liquid metal is increased in order to pump the metal into the fiber. After 15 seconds, the oven is switched off for the metal inside the fiber to solidify again.
6. Once the metal of the fiber is solidified, the fibers are removed from the metal container of the pressure chamber and the container is removed from the pressure chamber. The screw with the fibers is screwed in the pressure chamber again and the oven is switched on again to melt the metal inside the fiber.
7. Once the metal inside the fiber is liquid again, the pressure in the chamber is increased to pump the metal inside the fiber again to a new frontier point which is further than the previous one. This is done to remove the metal from the fiber tip in order to be able to splice this fiber for the experimental measurements.
8. Once the metal has been pumped again, the oven is switched off in order to solidify the metal inside the fiber. Once the metal is solid, the fabrication process is over.

At the end of this process the fiber looks like the one shown in the next figure:

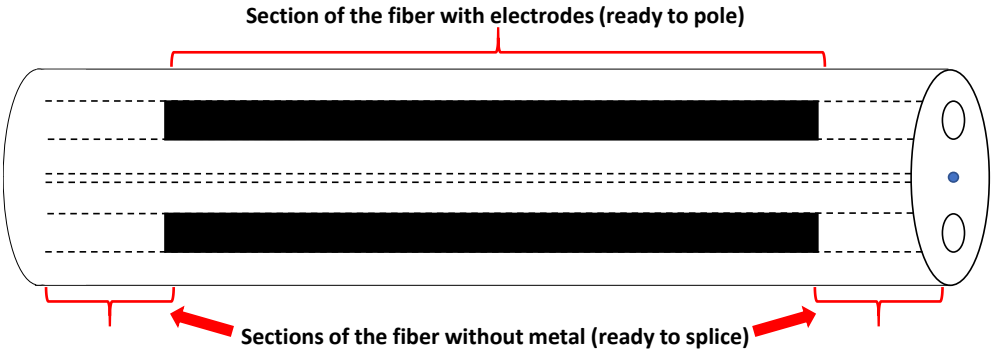

Fig. 6.3. Holed fiber after the metal insertion process

Once the electrodes are already inside, the electrodes must be connected to thin wires in order to connect the fiber to the voltage generator to pole the fiber. This is also a step by step process and it is explained here:

1. The first step is to remove the plastic coating of the fiber at a certain spot close to any of the edges of the electrodes. This coating removal can be performed using a hot acid bath, dichloromethane solution or using a scalpel
2. Once the coating has been removed, the cladding of the fiber must be polished in order to reach the electrode.
3. Once the electrode is accessible, a thin wire is placed close to the electrode and it is fixed with adhesive tape.

4. The final step is to drop a bit of conductive epoxy in order to electrically connect the thin wire and the electrode. This epoxy was cured using an oven at 90 ºC. Once the epoxy is applied and cured, the electrode and the thin wire are completely electrically connected and voltage can be applied to the fiber.
5. The process must be repeated in order to connect the other electrode.

This step by step process is showed in Fig. 6.4. Once the component is finished, the poling of the fiber can begin.

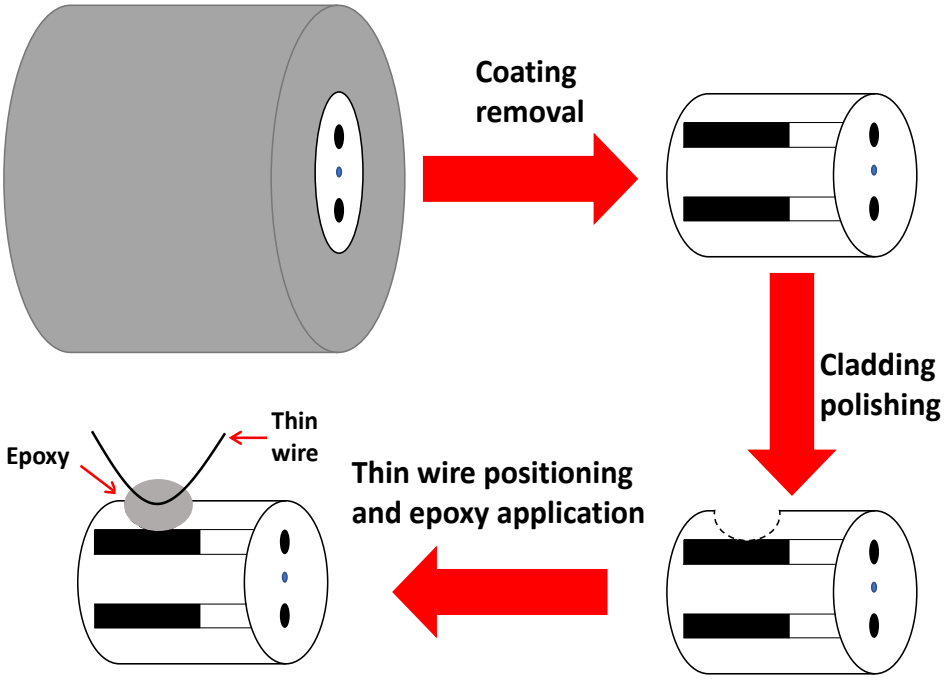

Fig. 6.4. Step by step process to connect the electrodes to thin wires

6.2.1 Thermal poling

Thermal poling [13] is a very well known technique that has been used in the past decades in order to generate higher second-order susceptibility through freezing a static electric field inside a glass fiber [22].

In this technique the fiber with electrodes is placed in a hot plate, it is exposed to high temperature (≈ 300 ºC) and a high-voltage (HV) supply is used to apply the voltage to the fiber. When this happens a space charge region is created. This is shown in Fig. 6.5.

Thanks to this process, the created second non-linearity induced by thermal poling can be expressed as follows [23]:

$$\chi^{(2)} = 3\chi^{(3)}E_{rec} \tag{6.1}$$

where $\chi^{(3)}$ is the third-order susceptibility (property of the material) and E_{rec} is the electric field recorded in the fiber. This effect comes from the movement of ions present in the fiber due to the application of the electric field at high temperatures [22]. The depletion region that is formed in the fiber is an evidence of the electric field recorded in the fiber and therefore an increment in the second-order nonlinearity of the device [24].

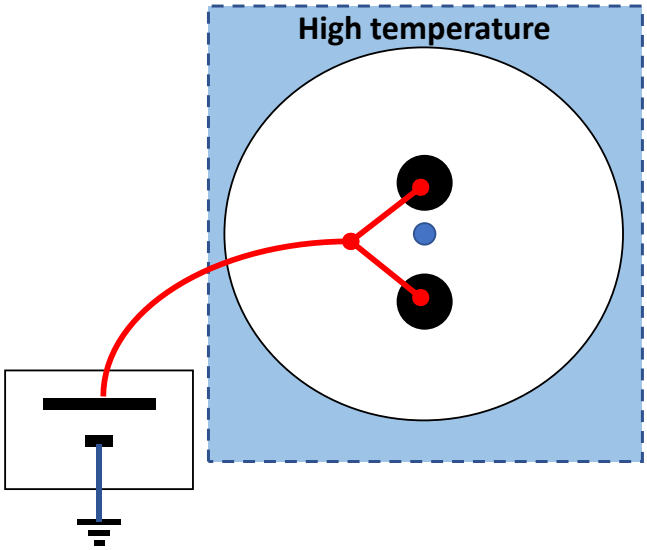

Fig. 6.5. Thermal poling setup

6.2.2 Optical poling

The setup used to optically pole the fiber is shown in Fig. 6.6 [25]. The frequency doubled Q-switched (1.2 kHz) and mode-locked (100 MHz) Nd:YAG laser operating at 1.064 µm wavelength and frequency doubled in a 3 mm KTP crystal, constitutes the green light source. The fundamental wavelength of the laser (1,064 nm) is filtered by a dichroic mirror (F1) and a KG5 filter (F2). The green beam generated through second harmonic generation could be blocked using a shutter. This green light was injected in the fiber using a mirror and a lens (a microscope objective). The injection was done in the fiber end in which the component was spliced (furthest end from the laser position). The power of this beam was around 18 mW (peak power around 7.5 kW). In the setup was also prepared the poling monitoring equipment. This monitoring process is

based on the phase change that happens in a Sagnac interferometer [26]. The light of a very incoherent light (amplified spontaneous emission of an EDFA) is coupled to port 1 of the 3 dB coupler and directed to port 2 where it is collimated using another lens. After passing through a red filter (F3), used to block the remaining green light, it is split in a beam splitter (BS), in order to be injected in the interferometer. The interferometer consists of 20 m of SMF spliced to the component that was going to be poled. Finally, the infrared light injected in the fiber is headed to port 3 of the 3 dB coupler where a detector and a digital oscilloscope are used to monitor the interferometer detected signal. Port 4 of the coupler was terminated. The polarization controller of the interferometer was used to maximize the CW signal seen in the oscilloscope.

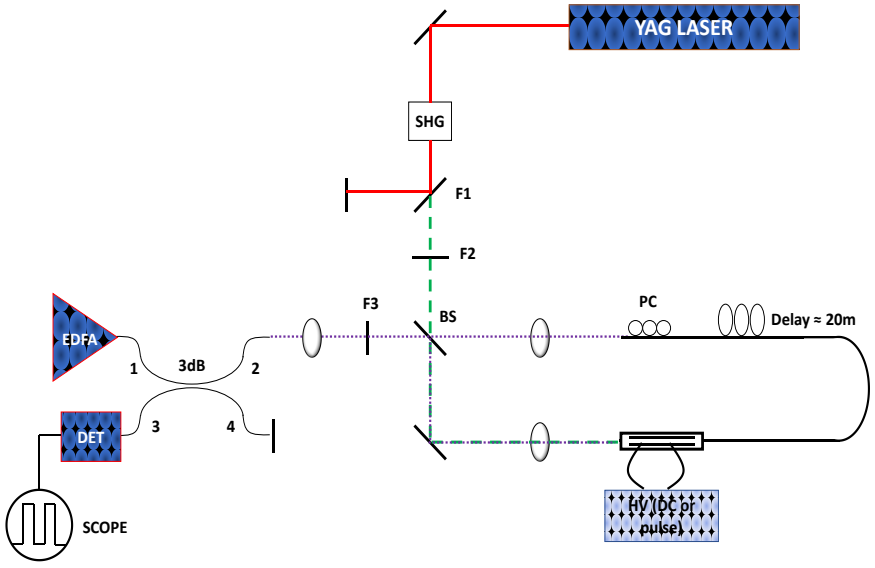

Fig. 6.6. Optical poling setup

The poling procedure starts when the voltage generator is switched on in DC mode and green light is injected to the component. This way, an electrical field starts to be recorded in the core of the fiber. From time to time, the green light was blocked, the EDFA was switched on, the voltage generator was switched to pulse mode and the signal of the interferometer was monitored. The signal measured from the interferometer is shown in Fig. 6.7 (two peaks are shown due to the two different polarizations).

As can be seen, when a pulse coming from the HV source stimulates the component, the signal detected coming from the interferometer changes (due to a phase change created by the non-symetrical position of the component inside the interferometer which creates a phase difference between the clockwise and the anticlockwise signals) [26]. The goal of these monitoring measurements is to calculate the V_π of the component. When it is not poled, the V_π is greater than

2 kV. After the poling of the fiber has started, this value decreases, meaning that the electro-optic coefficient is being increased. When the poling process is finished, the V_π could be around 600 V for a 1m-long component.

The reason why the green light beam is blocked when the V_π is being measured is due to the fact that when no voltage is being applied, the green light beam erases the electric field already recorded in the fiber [25]. The photocarriers generated by the strong beam move to cancel the charge distribution created by the poling process.

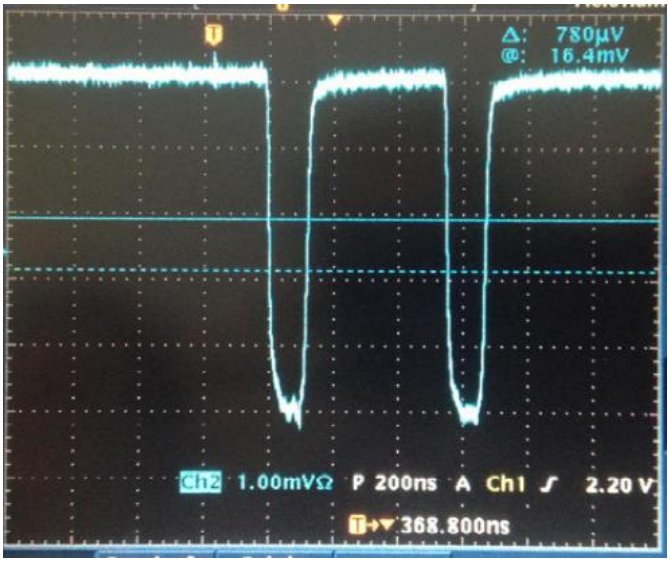

Fig. 6.7. V_π monitoring measurement

In contrast to thermal poling, in which the charges movement occurs from anode to cathode, in optical poling this can only happen in the core of the fiber, thanks to the strong beam excitation (green light). This makes the optical poling created field different compared to the thermal poled case.

In thermal poling, the amount of mobile ions is permanent once the fiber is fabricated. Nevertheless, in optical poling the amount of carriers released depends on the excitation beam, therefore it can be controlled. The charge movement is completed when the created field equals the applied field (DC voltage). This created field could be increased in the case of the thermal poling. To do so, the thickness of the sample should be much greater than the depletion region. However, this is not possible in optical fibers due to the small size, which makes thermal and optical poling equally effective at this particular scale

Another difference between both techniques is the ability of optical poling to pole fibers at room temperature.

6.3 FBG fabrication

As it has been stated in the introduction of this chapter, FBGs were going to be fabricated in the already poled fibers in order to make use of them as sensors. The first step to fabricate the FBGs with the fabrication system available is to hydrogenate the fiber. To do so, the fiber is exposed to a hydrogen atmosphere at 20 bars of pressure for two weeks. Once this period of time is over, the fiber is photosensitive.

The main problem with the fabrication of FBGs within poled fibers is the core visibility. The existence of both electrodes can hide the core from the UV beam used to inscribe the FBG. Fortunately, as it has been stated in Chapter 2, the fabrication setup of the laboratory has a core tracking method.

The first step to fabricate the FBG is to fix the fiber in the fabrication setup. This must be done with extremely care due to the diminished tensile strength of the poled fiber (metal insertion and polishing of the fiber to connect the electrodes to thin wires threaten structural strength). Once the fiber is fixed in the fabrication platform, it must be ensured that the core of the fiber is visible from the UV beam perspective. To ensure that this is the actual situation, the phase mask is removed from the system and the shutter is open. This way the UV beam coming from the laser hits the fiber. If the core is visible, the tracking system will reach a steady state. Otherwise it will move the beam down up to the limit position, proving this way that one of the electrodes is blocking the beam. If this is the actual situation, the fiber must be rotated in order to make the core visible. This is shown in the next figure:

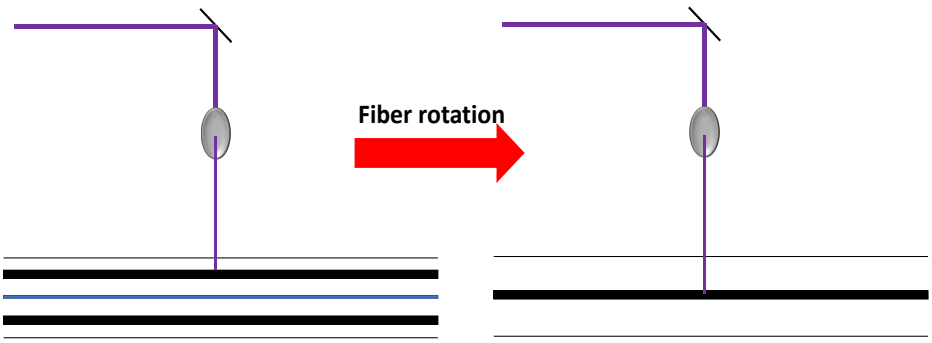

Fig. 6.8. Procedure to make the core of the fiber visible from the UV laser beam perspective

Once the visibility of the core is ensured, the phase mask is added to the system one more time and the fabrication procedure can start. The first thing to do is to move the platform a bit, due to the fact that the UV beam has already hit the fiber and therefore not only the average refractive index has changed in that particular spot but the poling effect has been attenuated also (green light can

remove poling when no HV is being applied to the fiber, so UV light, which is an even more powerful radiation, does it too).

This poling removal effect [25] also happens during FBG fabrication. The phase mask technique used to inscribe the gratings is based in the interferometric pattern created by the grating of the phase mask (see Fig. 6.9). This interferometric region comes from the interference of the created ±1 orders. The problem is that a 0 order is also created, and this beam erases the poling from the fiber while the FBG is being inscribed. Another effect that can contribute to poling erasing is the movement errors of the translation platform that moves the mirror and the phase mask to the next position for the next exposure to UV light. The FBG at the end is a collection of superimposed exposures to the Gaussian UV beam.

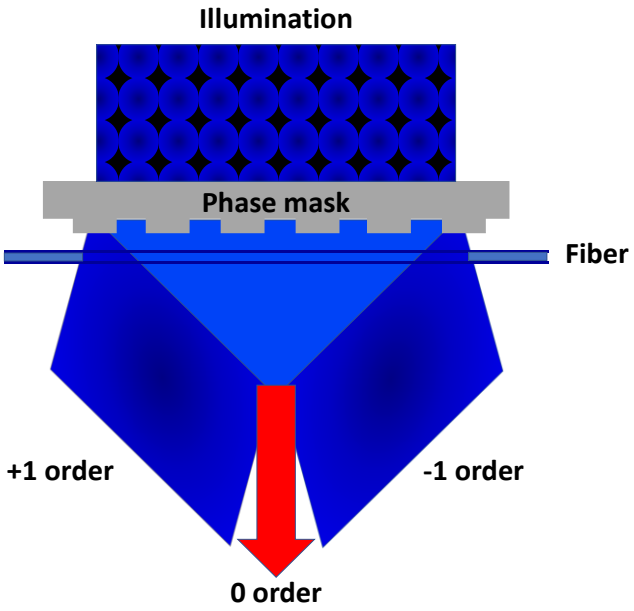

Fig. 6.9. Phase mask inscription technique

Any mismatch between exposures (superposition between consecutive exposures is not perfect), is going to remove the poling effect from that particular point. In order to compare both phenomena, the decision that was made was to fabricate a point FBG and a 1 cm FBG in order to compare their performances. There was a second reason to fabricate a point FBG also. This was the possible rotation of the fiber. In the starting position of the FBG inscription the core is visible for the UV beam, but as the platform moves this visibility can be lowered by the electrodes if the fiber shows some rotation. This rotation effect is not important when an SMF is used but as the fiber here has two electrodes parallel to the fiber core if the position of this electrodes change

along the FBG length, the UV beam can be blocked partially in some point by the electrodes and the symmetry of the FBG can be compromised.

To fabricate a point FBG, the shutter of the system is open while the platform is fixed so the FBG length is the width of the beam. While the beam is open the FBG growth is monitored in order to stop the inscription before saturation is reached. The shutter is also closed every second while the FBG is inscribed in order not to heat the fiber, what can cause some blurring in the interferometric pattern that is being inscribed, making the FBG weaker and erasing more poling from the fiber. For the standard FBG, the procedure is the regular one.

At the end of the inscription process, an interferometric pattern has been inscribed in the fiber creating both FBGs. But as it has been stated before, UV light erases poling. So, in the high power fringes of the interferometric pattern the poling effect has being erased (not completely since the UV source is not comparable to the green light source that was used to pole the fiber in terms of power) while this is not the case for the low power fringes.

When an electric field is applied to a poled fiber, the through-poling increased electro-optic effect changes slightly the refractive index of the fiber. If a grating has been inscribed in the fiber, this electric field would change the grating structure. But this change is bigger in the areas not affected by UV light during inscription compared to the areas in which the refractive index has been enlarged through UV exposure due to the fact that UV erases poling (see Fig. 6.10). This change in the structure of the FBG is going to change also the optical spectrum of the FBG and this can be utilized to use this component as a sensor device.

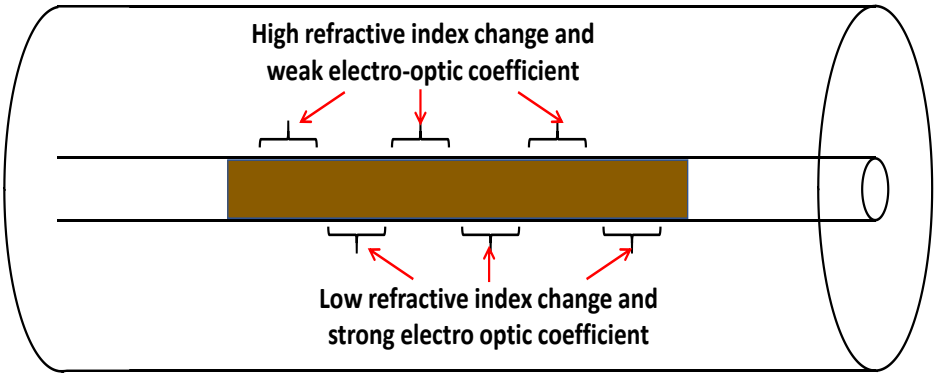

Fig. 6.10. Situation created in the core of the fiber after poling and FBG inscription

6.4 Principle of operation and experimental measurements

The setup used to perform the experimental measurements is showed in Fig. 6.11. Two types of measurements were carried out. In the first one, the effect of

DC voltage in the FBGs inscribed in the poled fiber was studied using a broadband source and an Optical Spectrum Analyzer (OSA). In the second case, the voltage supply was in the pulsed mode, and a tunable laser and an Optical Signal Analyzer (OSA*) were used to perform the measurements.

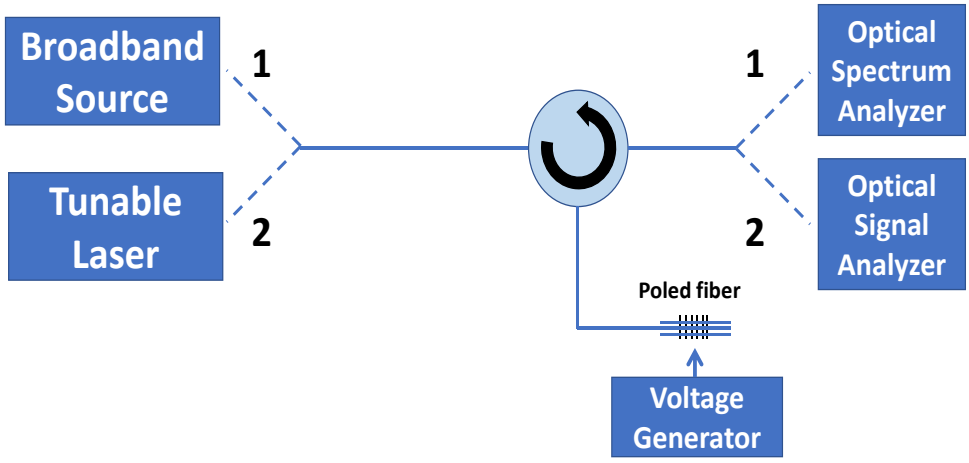

Fig. 6.11. Schematic view of the experimental measurements setup

As it has been explained in the previous section of this chapter, the application of an electric field to a poled fiber changes the refractive index in the poled area thanks to an increased electro-optic effect. One could think that this refractive index change is going to be constant along the entire FBG length, but this is not the case. UV light erases poling from the fiber so some parts of the FBG are strongly poled while the rest of the FBG is weakly poled (in theory). If the FBG suffers a constant refractive index change in its entire length the direct effect would be a displacement in wavelength of the spectrum. But if the change is not constant along the FBG, what is being changed is the Δn of the modulation of the refractive index produced when the FBG is created.

For the weak FBG, on the one hand, in the spots in which the UV power was high during inscription, the refractive index is high but the poling effect is small. On the other hand, in the spots where UV light was weak, the refractive index change is small but the poling effect is still high. Taking this into account, when voltage is applied to the fiber, the refractive index of the fiber is going to change slightly but it is going to change more in the spots where UV light was weak. This way the Δn created by UV light is going to be slightly diminished. So the expected effect in the optical spectrum of the weak FBG is a slight broadening and weakening of the FBG. For the standard FBG, the expected effect is a Bragg wavelength drift, since there is not so much difference between the fringes since the exposure time was smaller compared to the point FBG.

To study this effect, the light coming from a broadband source was headed into port 1 of a circulator. In port 2 it was the poled fiber with the FBGs inscribed. These FBGs reflected the light which went, once reflected, to port 3 of the circulator, in which an OSA was connected to monitor the FBG reflected spectrum. The poled fiber was connected to a voltage supply in DC mode.

The spectrum of the FBGs was monitored with a 1pm resolution and every time the voltage supplied was changed a new spectrum was recorded. In Fig. 6.12 it can be seen the spectra of the FBGs that were inscribed in the poled fiber (left: point FBG, right: standard FBG).

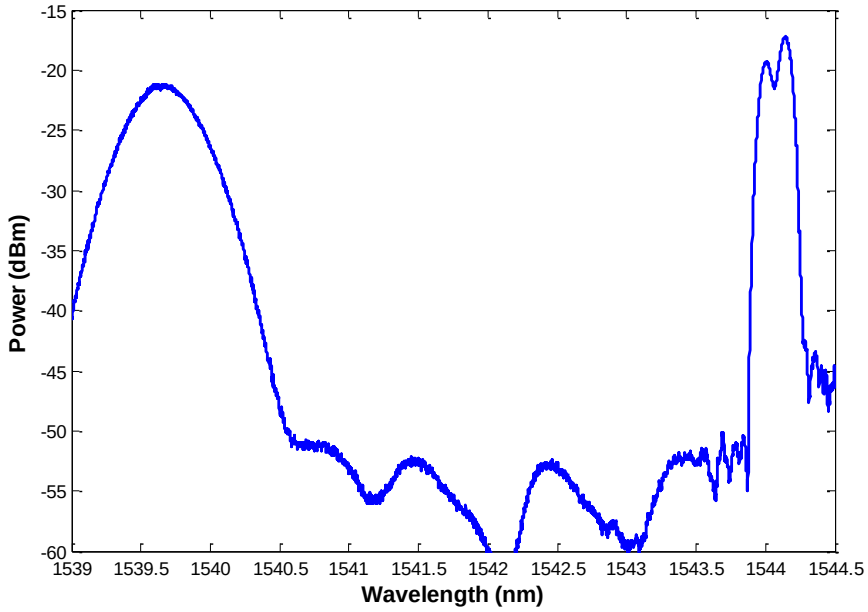

Fig. 6.12. Spectra of the fabricated FBGs

As can be seen the point FBG was much wider than the standard FBG due to its limited length and the standard FBG showed an abnormal shape due to the birefringence action (both polarizations experience different refractive index).

The DC voltage effect in the FBGs is shown in Fig. 6.13. As can be seen in the figure the effect is different for both FBG and the changes are explained here:

- Weak FBG: The main effect seen in the weak FBG spectrum is a broadening of the spectrum and a slight movement. As it has been stated previously, the application of voltage is going to reduce the Δn of the modulation created in the fiber by the UV light exposure. A small reduction in the peak reflectivity is also confirmed but almost negligible.

- Standard FBG: the effect that can be seen in the FBG is a Bragg wavelength movement. This movement grows as the voltage does it.

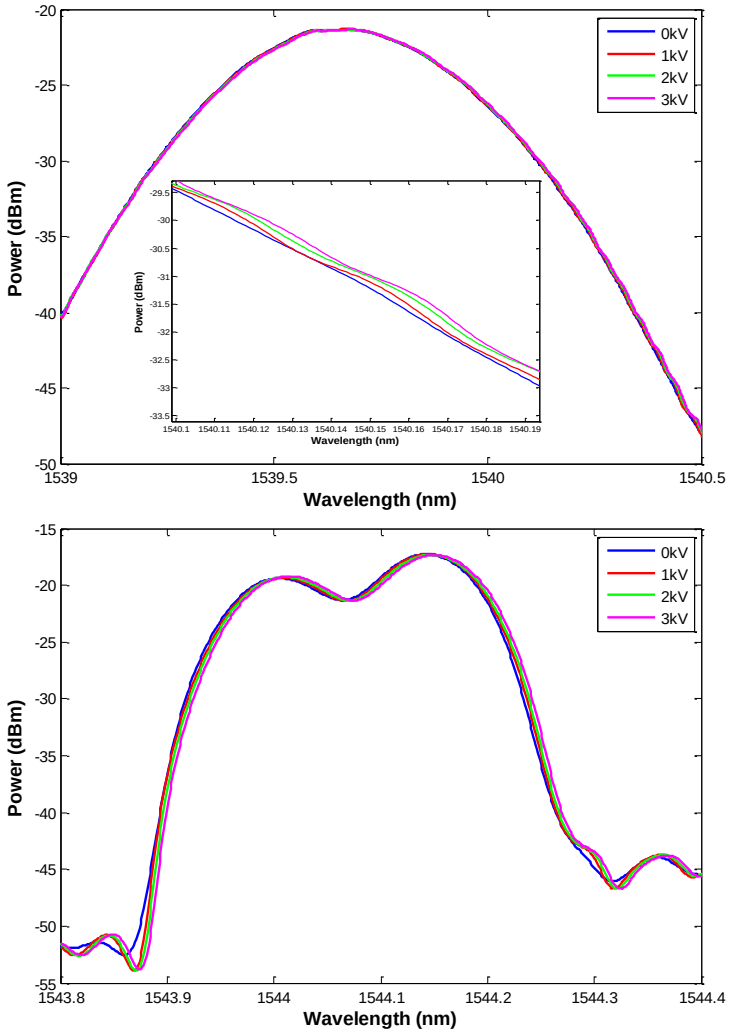

Fig. 6.13. Effect of different DC voltage in the FBGs shape. Upper: Weak FBG and zoom view (inset), lower: standard FBG

So there is a difference in the effect of DC voltage on the point and standard FBG. This difference is created by the different fabrication process used to inscribe these gratings in the poled fiber. For the point FBG, the shutter was opened and the platform was steady. That means that the UV light was hitting always the same spot (temperature changes in the fiber caused by the UV beam are neglected). So taking into account that the total exposure time was around

20 s, the amount of poling removed from the fringes exposed to high UV power is great compared to the standard FBG. This means that the Δn created by the UV light is getting smaller when the voltage is applied (poled areas experience a greater refractive index change than those where the poling effect was partially erased). However, in the standard FBG, the fabrication procedure consists on exposure to the UV light followed by a movement of the platform for a new exposure. This means that the exposure time of every section of the FBG is small compared to the point FBG (0.5 s in this case). This means that the erasure of the poling effect is not so strong in the standard FBG, therefore the difference between the fringes of the FBG is almost negligible in terms of poling and that is why in this case the Δn created by the UV light is being kept more or less constant when the DC voltage is applied and that is why the effect of the DC voltage is in this case a displacement of the FBG spectrum (increment in the average refractive index that affects the entire FBG and not only some parts of it). Finally, the effect of DC voltage is also greater in the standard FBG than in the point FBG probably due to the shorter exposure time (stronger poling effect). The curve that represent the relationship between the voltage applied and the movement of the standard FBG is shown in Fig. 6.14.

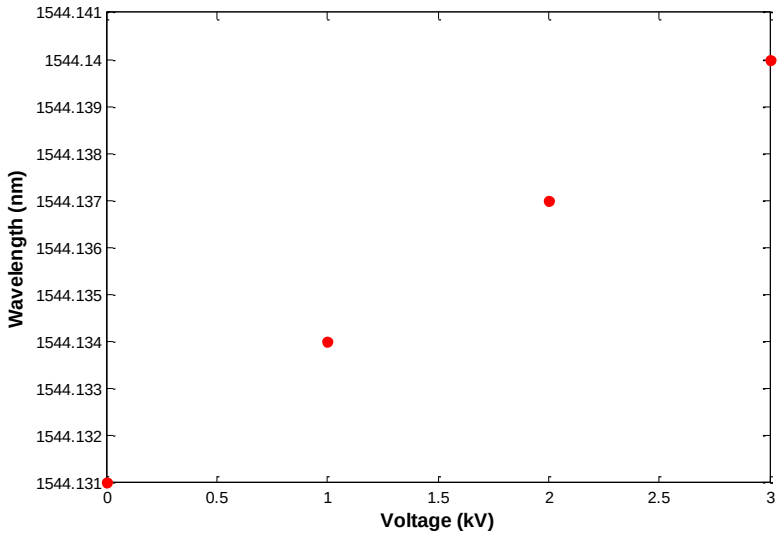

Fig. 6.14. Standard FBG movement related to the DC voltage applied

As can be seen, the FBG movement is linear with the voltage applied. A 10 pm change for 3 kV applied to the fiber is showed. This demonstrates that the poled fiber with FBGs inscribed on it can be used to measure DC voltage.

In order to measure the effect of a pulsed HV source, the optical broadband source is replaced by a tunable laser. This laser can be tuned in order to emit at

any wavelength of the third window. So the measurement procedure starts with the laser emitting inside the bandwidth of an FBG (at the edge of an FBG). After being reflected by the FBG, the signal goes to an optical signal analyzer (OSA*). In this optical signal analyzer, the incoming signal is photodetected and the spectrum of the radiofrequency signal detected is showed in a screen. In the beginning, as the HV generator is not modulated, only a DC electrical signal will be showed in the screen of the OSA* since the reflected laser power shows no changes in time. But if a modulation is applied to the voltage source, the FBG will be affected by this voltage, the Bragg wavelength of the FBG will change, and the optical power reflected by the FBG at the laser particular wavelength will also change following the frequency of the modulation of the HV source. This way, if this reflected signal is photodetected, additionally to the DC component, there will be present the frequency of the train of pulses modulating the HV generator in the screen as well. This principle of operation is shown in Fig. 6.15.

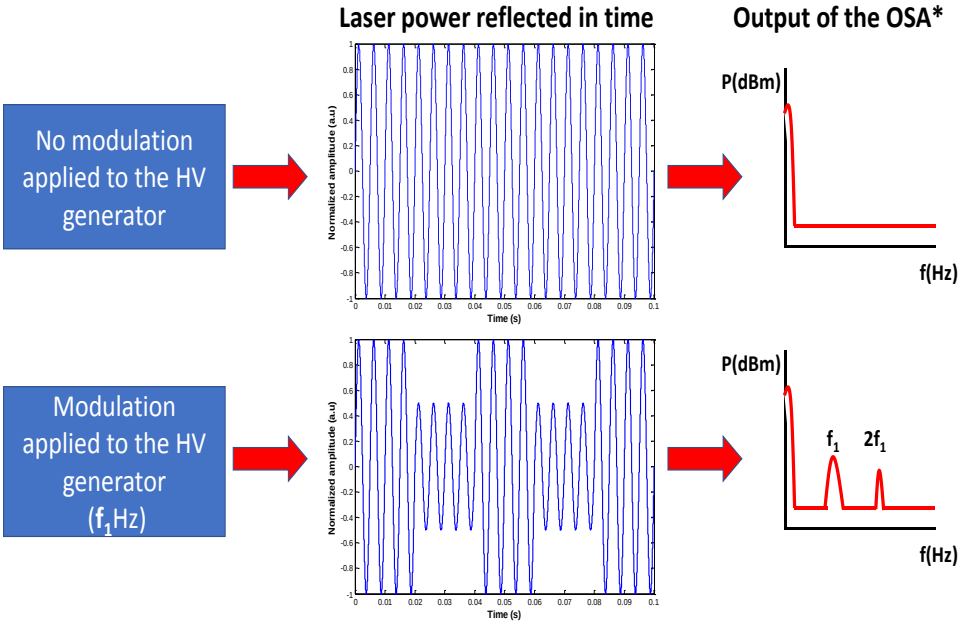

Fig. 6.15. Operational principle of the AC voltage measurement

This principle of operation was tested through experimental measurements. A tunable laser was set to emit at 1,544.2 nm (the right edge of the fabricated standard FBG). A train of square-shaped pulses fed the voltage generator in order to modulate the output of the source to create a train of HV pulses. This HV pulses drove the poled fiber what affected the reflected signal by the FBG in terms of power. This reflected signal was then fed to the OSA*, where the

signal was photodetected and its frequency components were showed in the screen of the apparatus.

A 1 kHz square signal was fed into the HV source to create a train of pulses at that particular frequency. The output of the laser was set to 8 dBm and the reflected signal was fed into the OSA*. The HV magnitude was changed between consecutive measurements and the traces showed at the screen of the OSA* were captured. The results obtained are shown in Fig. 6.16.

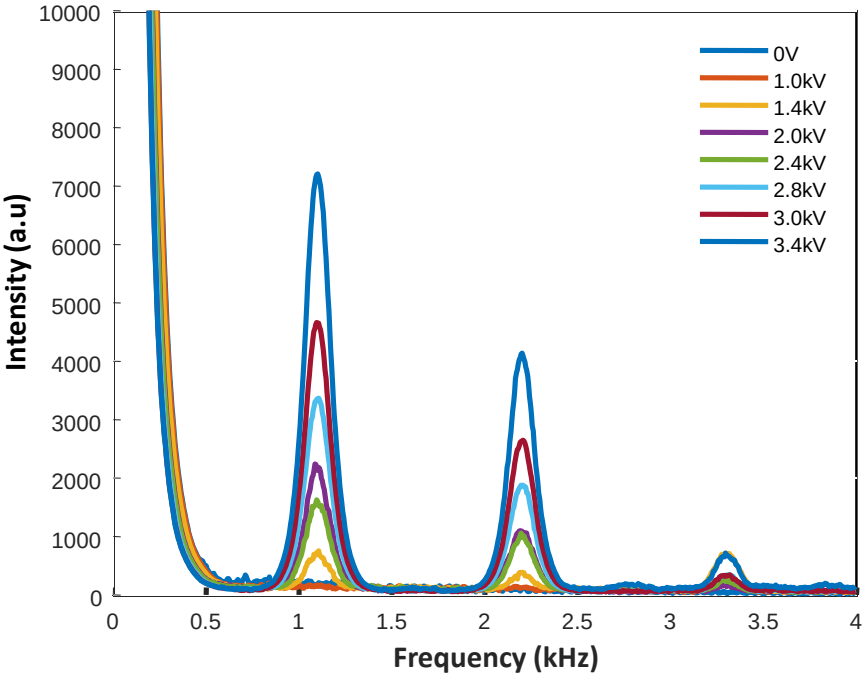

Fig. 6.16. RF signal detected by the OSA* for different voltages

As can be seen, the 1 KHz signal (and the multiples of it) can be clearly seen in the screen of the OSA*. The generated peaks grow when the voltage is increased due to a higher change in the laser power. If the peak values at 1 kHz are extracted the retrieved curve is the one showed in Fig. 6.17 (red points).

As can be seen, the measured values follow a trend similar to a quadratic curve. But there are some peaks and valleys in the distribution. These can be caused by mode competition, is it to say, the power distribution between the fundamental peak and the multiples of it is not always the same. Another factor that could be contributing to this situation is the quality of the signal that is driving the HV generator.

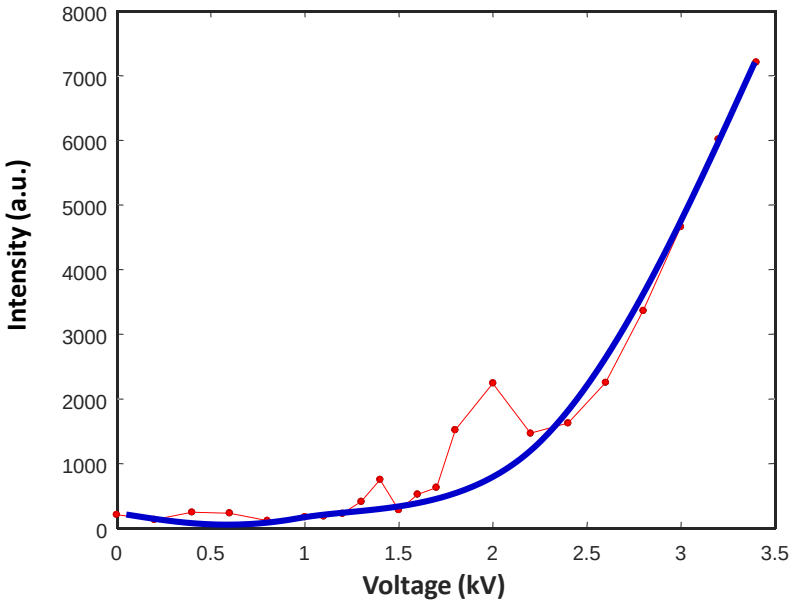

Fig. 6.17. Retrieved values from the OSA* traces (red points) and fitting (blue curve)

It is showed in Fig. 6.18, the signal driving the HV generator (lower trace) and the photodetected electric signals (upper traces) for the two different edges of the FBG before their spectrum is shown in the screen of the OSA*. The driving signal is not a perfect train of square pulses. This can affect the frequency that is being generated since the change in the pole fiber is not constant. Additionally, the signal detected and showed in the screen of the OSA* afterwards is very noisy. This affects the quality of the modulation tone detected and showed in the OSA* and can explain the behavior showed in Fig. 6.17. The reason why there exists an apparently 180º phase change between the traces showed in the upper part of Fig. 6.18 is due to the difference behavior when the laser is on one edge of the FBG or the other. If the laser is in the right edge of the FBG, when the voltage is applied, the FBG moves to the right what means an increment in the power reflected. When the laser is on the left edge the behavior is just the opposite (when the grating moves to the right, the reflected power of the laser is smaller).

Anyway, the frequency of the signal driving the HV generator is clearly detected by the OSA* and the magnitude of the signal follows, although not perfectly, the increments of the voltage level applied to the pole fiber.

A new measurement was carried out keeping the voltage peak level and changing the frequency of the modulation produced. In Fig. 6.19 the results can be observed.

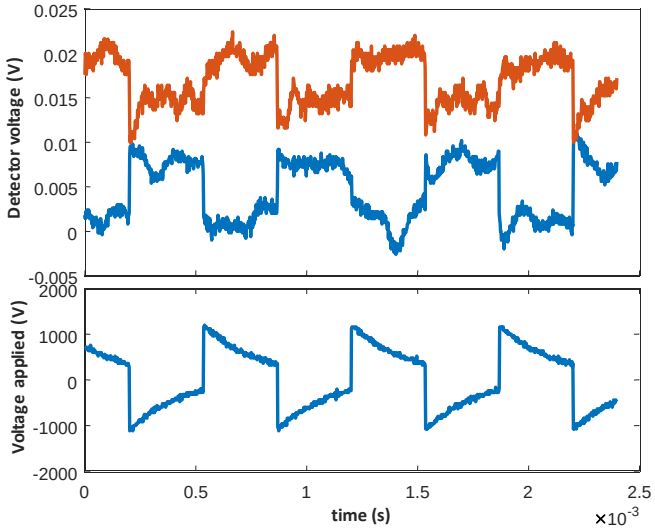

Fig. 6.18. Upper: Reflected laser power in time for the two edges of the FBG. Lower: Modulation signal applied to the poled fiber

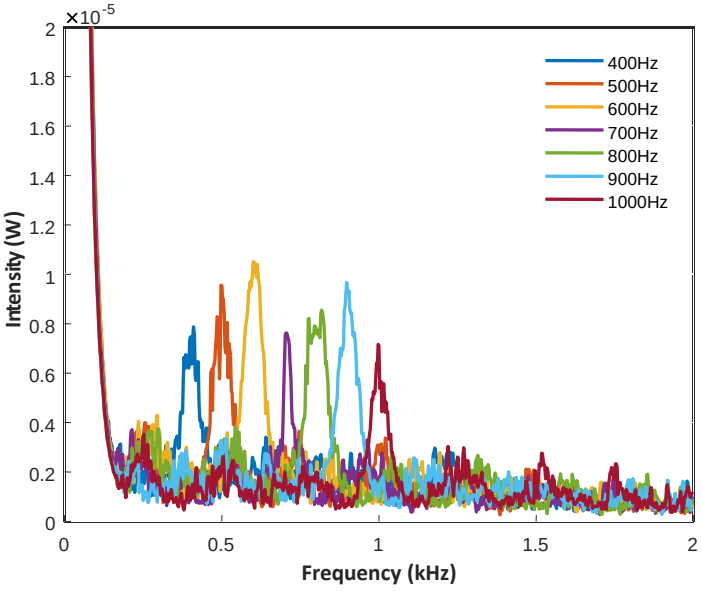

Fig. 6.19. Peaks detected by the OSA* for a HV modulation of 1.3kV and different values of frequency

Fig. 6.19 shows that the OSA* is able to measure the frequency change perfectly although the amplitude value changes for the different traces. This variability showed in the amplitude levels is caused by the two factors discussed previously and could be probably solved taking the average value of a certain

number of measurements although that would mean a decrement in the measurement speed.

6.5 Conclusions

In this chapter optically poled fibers with FBGs play the role of electric field sensors. This kind of device has demonstrated to be able to measure DC and AC voltage applied to it in terms of magnitude and frequency.

To measure DC voltage, a broadband source and an optical spectrum analyzer are used to study the effect of the electric field in the fiber. Two FBGs were fabricated in the poled fiber, a point FBG and a standard FBG. The effect of DC voltage was different in both gratings due to the different fabrication process. On the one hand, for the point FBG, the effect shown in the experimental measurements is a broadening of the spectrum. On the other hand, for the standard FBG, the effect is a movement of the Bragg wavelength of the grating. As the effect is greater in the standard FBG, it is used to monitor the voltage applied to the fiber. A linear relationship between the voltage magnitude and the movement of the Bragg wavelength of the FBG is demonstrated.

To measure the AC voltage, the broadband source and the OSA are replaced by a tunable laser and an optical signal analyzer respectively. The HV supply is driven by a square-shape train of pulses at a particular frequency in order to create HV pulses. The reflected power of the laser is modulated at the frequency of the modulation applied to the pole fiber and the values are retrieved by the OSA*. In the spectrum retrieved by the OSA* it can be clearly seen the frequency of the modulation applied to the HV generator. Additionally, the amplitude of the peaks showed in the screen of the OSA* are dependent on the magnitude of the HV pulses. A quadratic relationship between both parameters has been showed in the experimental measurements. This relationship is not perfect, and it is caused by mode competition and the shape of the signal that is driving the HV generator. If the average of a certain number of measurements is used instead of a unique sweep, the results could be improved but the speed of the interrogation technique would be affected.

References

[1] Otto Strobel, "Optical Fibers," in *Optical and Microwave Technologies for Telecommunication Networks* , , Wiley, 2016, pp.

[2] K. Thyagarajan; Ajoy Ghatak, "Fiber Optic Components," in *Fiber Optic Essentials* , , IEEE, 2007, pp.

[3] L. H. Spiekman, "Active Devices in Passive Optical Networks," in *Journal of Lightwave Technology*, vol. 31, no. 4, pp. 488-497, Feb.15, 2013.

[4] J. K. Sahu *et al*., "Progress in active fibers," *OFC/NFOEC 2007 - 2007 Conference on Optical Fiber Communication and the National Fiber Optic Engineers Conference*, Anaheim, CA, 2007, pp. 1-3.

[5] S. C. Fleming, T. Fujiwara, D. Wong, Y. Zhao and S. B. Poole, "Poled fiber devices-mechanisms and applications," *Optical Fiber Communications, OFC.*, San Jose, CA, USA, 1996, pp. 287-288.

[6] K. Lee, S. Fleming and J. L. Blows, "Poling of single electrode fibre with polyimide conductive coating and investigation of poling mechanism," in *Electronics Letters*, vol. 42, no. 5, pp. 273-274, 2 March 2006.

[7] L. Huang, G. Ren, Y. Gao, B. Zhu and W. Peng, "Design of Thermally Poled Twin-Core Fiber Coupler With Electrical Tunability," in *IEEE Photonics Technology Letters*, vol. 27, no. 8, pp. 919-922, 15 April15, 2015.

[8] X. -. Long and S. R. J. Brueck, "Large-signal phase retardation with a poled electrooptic fiber," in *IEEE Photonics Technology Letters*, vol. 9, no. 6, pp. 767-769, June 1997.

[9] X. -. Long, R. A. Myers and S. R. J. Brueck, "A poled electrooptic fiber," in *IEEE Photonics Technology Letters*, vol. 8, no. 2, pp. 227-229, Feb. 1996.

[10] P. G. Kazansky, P. S. J. Russell and H. Takebe, "Glass fiber poling and applications," in *Journal of Lightwave Technology*, vol. 15, no. 8, pp. 1484-1493, Aug. 1997.

[11] T. Fujiwara, D. Wong and S. Fleming, "Large electrooptic modulation in a thermally-poled germanosilicate fiber," in *IEEE Photonics Technology Letters*, vol. 7, no. 10, pp. 1177-1179, Oct. 1995.

[12] V. Pruneri and P. G. Kazansky, "Electric-field thermally poled optical fibers for quasi-phase-matched second-harmonic generation," in *IEEE Photonics Technology Letters*, vol. 9, no. 2, pp. 185-187, Feb. 1997.

[13] W. Xu, J. Arentoft, D. Wong and S. Fleming, "Evidence of space-charge effects in thermal poling," in *IEEE Photonics Technology Letters*, vol. 11, no. 10, pp. 1265-1267, Oct. 1999.

[14] T. Fujiwara, D. Wong, Y. Zhao, S. Fleming, S. Poole and M. Sceats, "Electro-optic modulation in germanosilicate fibre with UV-excited poling," in *Electronics Letters*, vol. 31, no. 7, pp. 573-575, 30 March 1995.

[15] A. Canagasabey, C. Corbari, A. V. Gladyshev, F. Liegeois, S. Guillement, Y. Hernandez, M. V. Yashkov, A. Kosolapov, E. M. Dia nov, M. Ibsen, and P. G. Kazansky, “High-average-power second-harmonic generation from

periodically poled silica fibers," Opt. Lett., vol. 34, no. 16, pp. 2483–2485, Aug. 2009.

[16] A. V. Gladyshev, C. Corbari, O. I. Medvedkov, S. A. Vasiliev, P. G. Kazansky and E. M. Dianov, "UV-Induced Absorption in All-Fiber Frequency Doublers: Characterization and Photobleaching," in *Journal of Lightwave Technology*, vol. 33, no. 2, pp. 439-442, 15 Jan.15, 2015.

[17] Kun-Long Chen and Wilsun Xu, "Voltage distortion measurement using a contactless sensor," *2016 IEEE Power and Energy Society General Meeting (PESGM)*, Boston, MA, 2016, pp. 1-5.

[18] P. Blazkiewicz, W. Xu, D. Wong, S. Fleming and T. Ryan, "Modification of thermal poling evolution using novel twin-hole fibers," in *Journal of Lightwave Technology*, vol. 19, no. 8, pp. 1149-1154, Aug. 2001.

[19] W. Xu, J. Arentoft, D. Wong and S. Fleming, "Evidence of space-charge effects in thermal poling," in *IEEE Photonics Technology Letters*, vol. 11, no. 10, pp. 1265-1267, Oct. 1999.

[20] W. Margulis and N. Myren, "Progress on fiber poling and devices," *OFC/NFOEC Technical Digest. Optical Fiber Communication Conference, 2005.*, Anaheim, CA, 2005, pp. 3 pp. Vol. 4-.

[21] F. De Lucia, D. Huang, C. Corbari, N. Healy, and P. Sazio, "Optical fiber poling by induction," Opt. Lett. 39, 6513-6516 (2014).

[22] H. An and S. Fleming, "Trapping second-order nonlinearity in erbium-doped germanosilicate ring in thermally poled optical fibre," in *Electronics Letters*, vol. 42, no. 2, pp. 78-80, 19 Jan. 2006.

[23] W. Xu, D. Wong and S. Fleming, "Evolution of linear electro-optic coefficients and third-order nonlinearity during prolonged negative thermal poling of silica fibre," in *Electronics Letters*, vol. 35, no. 11, pp. 922-923, 27 May 1999.

[24] Caroline S. Franco, Gladys A. Quintero, Niklas Myrén, Alexandre Kudlinski, Hassina Zeghlache, Hélio R. Carvalho, Adriana L. C. Triques, Danays M. González, Paula M. P. Gouvêa, Gilbert Martinelli, Yves Quiquempois, Bernhard Lesche, Walter Margulis, and Isabel C. S. Carvalho, "Measurement of depletion region width in poled silica," Appl. Opt. 44, 5793-5796 (2005)

[25] Alexandre R. Camara, João M. B. Pereira, Oleksandr Tarasenko, Walter Margulis, and Isabel C. S. Carvalho, "Optical creation and erasure of the linear electrooptical effect in silica fiber," Opt. Express 23, 18060-18069 (2015).

[26] Mikael Malmström, Oleksandr Tarasenko, and Walter Margulis, "Pulse selection at 1 MHz with electrooptic fiber switch," Opt. Express 20, 9465-9470 (2012)

Chapter 7

Summary, conclusions and open research lines

7.1 Summary and conclusions

Following the general objectives of this Ph.D. new interrogation techniques have been designed and demonstrated through experimental measurements. Additionally, optically poled fibers with FBGs inscribed on them have been used as electric field sensors. This has required the usage of microwave photonics techniques and different equipment in order to optimize the performance of such devices.

In chapter 1, the context of this thesis has been presented. The main technologies as well as techniques to create and interrogate optical sensors have been reviewed along with the Microwave Photonics field. The performance, advantages and drawbacks of these techniques have been exposed and discussed.

In chapter 2, the wavelength to radio-frequency delay mapping technique has been presented and demonstrated. This technique is based on the use of a dispersive media to map the Bragg wavelength of FBGs into radio-frequency delays easily accessible once the impulse response of the system has been calculated. In order to increase the resolution, the so called zero-padding technique is used to increase the number of points of the impulse response. In consequence, the resolution in this interrogation technique is directly related to the dispersion of the system, the number of zeroes added to the raw data prior to IFFT calculation and the bandwidth of the electric measurement. This technique allows to interrogate FBGs arrays that may share or not the same reflection band.

In chapter 3, the previous technique was improved using the KLT routine in order to reduce the computational complexity while improving the resolution of the measurement. The wavelength to radio-frequency technique has a problem, the huge number of points it has to work with in order to produce a suitable resolution. This means that IFFT calculation and handling of the impulse response vector are costly processes. However, the KLT routine lets diminish the number of points over three orders of magnitude and at the same time it even increases the resolution of the measurement. Again, this technique allows to interrogate FBGs arrays that may share or not the same reflection band.

In chapter 4, the coherent interrogation of an array of 500 weak FBGs is introduced and demonstrated. The interrogation of the microwave photonics filter under a coherent regime allows to locate and measure hot spots inside the fiber while measuring the temperature/pressure at the same time. Thanks to the

interrogation technique developed and the characteristics of the sensor used, this sensor acts like a distributed sensor but without the disadvantages of the Brillouin or Rayleigh scattering methods (high power consumption, complex systems, low SNR or slow interrogation speed).

In chapter 5, the interrogation technique based on the conversion of phase modulation to intensity modulation is presented. This method is characterize by an astonishing sensitivity (1 dB/pm). This way, to measure temperatures changes below 0.1 ºC becomes trivial. The interrogation technique shows great simplicity and no post-processing is needed to retrieve the sensing data. It is also insensitive to power changes in the source since these are self-compensated by the interrogation technique.

Finally, in chapter 6, poled fibers with FBGs written on them are used as electric field sensors. A point and a standard FBG are inscribed in a poled fiber and the results extracted from them are different due to the differences of the fabrication process. These differences are based on the erasure of poling by UV light exposure. DC voltage is measured following the changes in the optical spectrum of the FBG and AC voltage is measured (frequency and magnitude) through photodetection of the optical power reflected by the FBG and the subsequent study of the electric spectrum of such signal.

To conclude, MWP applications applied to the field of optical sensing show some benefits compared to traditional techniques. Simplicity, power consumption, higher SNR, increment in resolution and sensitivity or the ability to interrogate arrays of FBG with the same spectral properties are some of the advantages that this application produces.

7.2 Open research lines

These are some research lines that may continue in the future:

- Development of integrated or more dedicated equipment to boost the speed of the interrogation techniques developed (local oscillators, DSP's, digital VNA, etc)
- Study the effect of different types of gratings in the sensitivity of the PM to IM conversion technique (phase shifted FBGs for example are expected to increase sensitivity due to the extremely narrow bandwidth of the passband).
- Study the effect of the characteristics of the FBGs (length, strength, bandwidth or type) written in the poled fiber to increase the performance of the electric field sensors.
- Increase the number of sensors interrogated using the coherent interrogation technique to the tens of thousands scale in order to study the effect of multiple reflection and power depletion.

- Introduction of new transformations (like the KLT routine) and data-processing techniques to boost the performance (speed, sensitivity, resolution or accuracy) of the interrogation techniques developed in this project.

Appendix 1
Author's publications

A.1 Scientific publications in journals

A. L. Ricchiuti, J. Hervás, D. Barrera, S. Sales and J. Capmany, "Microwave Photonics Filtering Technique for Interrogating a Very-Weak Fiber Bragg Grating Cascade Sensor," in IEEE Photonics Journal, vol. 6, no. 6, pp. 1-10, Dec. 2014.

J. Hervás, C. R. Fernández-Pousa, D. Barrera, D. Pastor, S. Sales, and J. Capmany, "An Interrogation Technique of FBG Cascade Sensors Using Wavelength to Radio-Frequency Delay Mapping," J. Lightwave Technol., vol 33, pp 2222-2227, 2015.

A. L. Ricchiuti, J. Hervás and S. Sales, [INVITED] "Cascade FBGs distributed sensors interrogation using microwave photonics filtering techniques," Optics & Laser Technol., vol. 77, pp 144-150, 2016.

J. Hervás, I. Suárez, J. Pérez, P.J. Rodríguez Cantó, R. Abargues, J. P. Martínez-Pastor, S. Sales and J. Capmany, "MWP phase shifters integrated in PbS-SU8 waveguides," Opt. Express, vol. 23, pp 14351-14359, 2015.

J. Clement, G. Torregrosa, J. Hervás, D. Barrera, S. Sales and C. R. Fernández-Pousa, "Interrogation of a Sensor Array of Identical Weak FBGs Using Dispersive Incoherent OFDR," in IEEE Photonics Technology Letters, vol. 28, no. 10, pp. 1154-1156, 2016.

J. Perez, I. Suárez, J. Hervás, A. L. Ricchiuti, J. P. Martínez-Pastor and S. Sales, "Continuous Broadband MWP True-Time Delay With PbS-PMMA and PbS-SU8 Waveguides," in IEEE Photonics Technology Letters, vol. 28, no. 15, pp. 1657-1660, 2016.

M. Llera, T. Aellen, J. Hervas, Y. Salvadé, P. Senn, S. Le Floch, and H. Keppner, "Liquid-air based Fabry-Pérot cavity on fiber tip sensor," Opt. Express, vol. 24, pp 8054-8065, 2016.

J. Hervás, D. Tosi, H. García-Miquel, D. Barrera, C. R. Fernández-Pousa and S. Sales, "KLT-Based Interrogation Technique for FBG Multiplexed Sensor Tracking," in Journal of Lightwave Technology, vol. 35, no. 16, pp. 3387-3392, 15 Aug.15, 2017.

J. Hervás et al., "Microwave Photonics for Optical Sensors," in IEEE Journal of Selected Topics in Quantum Electronics, vol. 23, no. 2, pp. 327-339, March-April 2017, Art no. 5602013.

I. Gasulla, D. Barrera, J. Hervás and S. Sales, "Spatial Division Multiplexed Microwave Signal processing by selective grating inscription in homogeneous multicore fibers," in Nature Scientific Reports, vol. PP, no. 99, pp. 1-1, 2016.

J. Clement Bellido et al., "Fast Incoherent OFDR Interrogation of FBG Arrays Using Sparse Radio Frequency Responses," in Journal of Lightwave Technology, vol. 36, no. 19, pp. 4393-4400, Oct.1, 2018.

J. Hervás, D. Barrera, J. Madrigal and S. Sales, "Microwave Photonics Filtering Interrogation Technique Under Coherent Regime For Hot Spot Detection on a Weak FBGs Array," in Journal of Lightwave Technology, vol. 36, no. 4, pp. 1039-1045, 15 Feb.15, 2018.

Sergi García, David Barrera, Javier Hervás, Salvador Sales and Ivana Gasulla, "Microwave Signal Processing over Multicore Fiber," in Photonics, vol. 4, no. 4, pp. 1-14, 2017.

A.2 Scientific publications in congresses

J. Hervás, A. Ricchiuti, D. Barrera, S. Sales, L. Thévenaz, and J. Capmany, "Weak fiber Bragg grating cascade sensor interrogation using microwave photonic filtering techniques," in Advanced Photonics, OSA Technical Digest (online) (Optical Society of America, 2014), paper SeW1C.2

J. Hervás, D. Barrera, S. Sales and J. Capmany, "Very high Q-factor microwave photonic FIR filter based on a ultralong FBG cascade," Microwave Photonics (MWP) and the 2014 9th Asia-Pacific Microwave Photonics Conference (APMP) 2014 International Topical Meeting on, Sendai, 2014, pp. 395-398.

J. Hervás et al., "MWP true time delay implemented in PbS-SU8 waveguides," 2015 17th International Conference on Transparent Optical Networks (ICTON), Budapest, 2015, pp. 1-4.

S. Sales, A. Ricchiuti, J. Hervás, D. Barrera and J. Capmany, "Sensor distribuido basado en FBGs débiles en cascada utilizando técnicas de Fotónica de Microondas," in XXX Simposium Nacional de la Unión Científica Internacional de Radio (URSI 2015), Pamplona, 2015, pp. 1-3.

J. Clement, J. Hervás, C. R. Fernández-Pousa, D. Barrera, D. Pastor, S. Sales and J. Capmany, "Interrogation of a cascaded FBG sensor using a wavelength-to-delay mapping technique," Proc. SPIE 9634, 24th International Conference on Optical Fibre Sensors, 96344S (September 28, 2015).

D. Barrera, J. Hervás, I. Gasulla and S. Sales, "Enhanced accuracy sensors using multicore optical fibres based on RFBGs for temperatures up to 1000°C," Proc. SPIE 9916, Sixth European Workshop on Optical Fibre Sensors, 99161J (May 30, 2016).

J. Clement, G. Torregrosa, J. Hervás and C. R. Fernández-Pousa, "Absolute Bragg wavelength and dispersion determination in dispersive incoherent OFDR interrogators" Proc. SPIE 9916, Sixth European Workshop on Optical Fibre Sensors, 99161K (May 30, 2016).

J. Hervás, D. Barrera, Carlos R. Fernández-Pousa and S. Sales, "FBGs cascade interrogation technique based on wavelength-to-delay mapping and KLT analysis," Proc. SPIE 9916, Sixth European Workshop on Optical Fibre Sensors, 991628 (May 30, 2016).

I. Gasulla, D. Barrera, J. Hervás, S. García and S. Sales, "Multi-cavity Microwave Photonics devices built upon multicore fibres," 2016 18th International Conference on Transparent Optical Networks (ICTON), Trento, 2016, pp. 1-4.

J. Hervás, D. Barrera, J. Madrigal and S. Sales, "Phase modulation to intensity modulation conversion for sensitive FBG sensor interrogation," in 25th International Conference on Optical Fibre Sensors, Jeju (Corea), 2017, Paper No. 10323-296.

J. Hervás, D. Barrera, J. Madrigal and S. Sales, "Microwave Photonics filtering interrogation technique under coherent regime for hot spot detection on cascaded FBG fiber," in 25th International Conference on Optical Fibre Sensors, Jeju (Corea), 2017, Paper No. 10323-293.

Javier Madrigal, David Barrera, Javier Hervás, Hailan Chen and S.Sales,"Directional curvature sensor based on long period gratings in multicore optical fiber," in 25th International Conference on Optical Fibre Sensors, Jeju (Corea), 2017, Paper No. 10323-197.

J. Clement, J. Madrigal, J. Hervás, and C. R. Fernández-Pousa, "Fast Interrogation of Equally-Spaced Arrays of Fiber Bragg Gratings Using Sparse Incoherent OFDR," in Advanced Photonics 2018 (BGPP, IPR, NP, NOMA, Sensors, Networks, SPPCom, SOF), OSA Technical Digest (online) (Optical Society of America, 2018), paper JTu2A.60.

I. Gasulla, S. García, D. Barrera, J. Hervás, and S. Sales, "Fiber-distributed Signal Processing: Where the Space Dimension Comes into Play," in Advanced Photonics 2017 (IPR, NOMA, Sensors, Networks, SPPCom, PS), OSA Technical Digest (online) (Optical Society of America, 2018), paper PW1D.1.

J. Hervás, J. Madrigal, D. Barrera and S. Sales, "Multiplexing FBG sensors combining microwave photonics and phase modulation," 2017 19th International Conference on Transparent Optical Networks (ICTON), Girona, 2017, pp. 1-4.

I. Gasulla, S. García, D. Barrera, J. Hervás and S. Sales, "Space-division Multiplexing for fiber-wireless communications," 2017 19th International Conference on Transparent Optical Networks (ICTON), Girona, 2017, pp. 1-4.

A.3 Participation in research projects

- Microwave photonics for emergent applications

- Financing entity: Ministry of Economy and Business
- Duration from: 01/01/2015 to: 01/07/2018
- Grant value: 202675 €

- Applications of nanophotonic technology to the telecommunication and sensing fields

- Financing entity: Ministry of Economy and Business
- Duration from: 07/10/2013 to: 31/12/2014
- Grant value: 179685 €